②

Naval Research Laboratory

Washington, DC 20375-5000

NRL Memorandum Report 6410

Low Reynolds Number Calculation of Turbulent Channel Flow: A General Discussion

R. A. HANDLER, E. W. HENDRICKS AND R. I. LEIGHTON

Laboratory for Computational Physics and Fluid Dynamics

February 23, 1989

Approved for public release; distribution unlimited.

SECURITY CLASSIFICATION OF THIS PAGE

REPORT DOCUMENTATION PAGE	*Form Approved* *OMB No 0704-0188*

1a REPORT SECURITY CLASSIFICATION UNCLASSIFIED	1b RESTRICTIVE MARKINGS
2a SECURITY CLASSIFICATION AUTHORITY	3 DISTRIBUTION/AVAILABILITY OF REPORT Approved for public release; distribution unlimited.
2b DECLASSIFICATION/DOWNGRADING SCHEDULE	
4 PERFORMING ORGANIZATION REPORT NUMBER(S) NRL Memorandum Report 6410	5 MONITORING ORGANIZATION REPORT NUMBER(S)

6a NAME OF PERFORMING ORGANIZATION Naval Research Laboratory	6b OFFICE SYMBOL *(If applicable)* Code 4420	7a NAME OF MONITORING ORGANIZATION
6c ADDRESS *(City, State, and ZIP Code)* Washington, DC 20375-5000		7b ADDRESS *(City, State, and ZIP Code)*
8a NAME OF FUNDING/SPONSORING ORGANIZATION Office of Naval Research	8b OFFICE SYMBOL *(If applicable)*	9 PROCUREMENT INSTRUMENT IDENTIFICATION NUMBER

8c ADDRESS *(City, State, and ZIP Code)*	10 SOURCE OF FUNDING NUMBERS			
	PROGRAM ELEMENT NO	PROJECT NO	TASK NO	WORK UNIT ACCESSION NO
Arlington, VA 22217	61153N		RR23-01-41	DN158-015

11 TITLE *(Include Security Classification)*
Low Reynolds Number Calculation of Turbulent Channel Flow: A General Discussion

12 PERSONAL AUTHOR(S)
Handler, R.A., Hendricks, E.W. and Leighton, R.I.

13a TYPE OF REPORT Interim	13b TIME COVERED FROM 10/88 TO 11/88	14 DATE OF REPORT *(Year, Month, Day)* 1989 February 23	15 PAGE COUNT 107

16 SUPPLEMENTARY NOTATION

17 COSATI CODES			18 SUBJECT TERMS *(Continue on reverse if necessary and identify by block number)*
FIELD	GROUP	SUB-GROUP	Turbulence aliasing, Conditional sampling, Spectral methods

19 ABSTRACT *(Continue on reverse if necessary and identify by block number)*

The statistical properties of turbulent flow in a channel at a wall Reynolds number of 125 using a moderate resolution direct numerical simulation is investigated. We have found that the use of a Green function method results in turbulent statistics which are significantly closer to experimental results than those produced by the Orszag-Kells (1980) splitting method. We have found some differences between our calculations and those of Kim, Moin and Moser (1987) (KMM). Our calculation gives somewhat lower turbulent intensities and longer streamwise correlation lengths. In general, however, the one and two point statistics are in good agreement with the KMM results. Conditional sampling calculations on the simulated data indicate a definite relationship between VITA and Q_2^{T} events. We have also found that aliasing errors cause strong damping effects on the final steady state turbulent velocity field.

20 DISTRIBUTION/AVAILABILITY OF ABSTRACT ☒ UNCLASSIFIED/UNLIMITED ☐ SAME AS RPT ☐ DTIC USERS	21 ABSTRACT SECURITY CLASSIFICATION UNCLASSIFIED	
22a NAME OF RESPONSIBLE INDIVIDUAL R.A. Handler	22b TELEPHONE *(Include Area Code)* (202) 767-2457	22c OFFICE SYMBOL Code 4420

DD Form 1473, JUN 86 *Previous editions are obsolete* SECURITY CLASSIFICATION OF THIS PAGE

S/N 0102-LF-014-6603

CONTENTS

LOW REYNOLDS NUMBER CALCULATION OF TURBULENT CHANNEL FLOW: A GENERAL DISCUSSION

1. Introduction

Direct numerical simulations (DNS) of turbulent shear flows have recently provided researchers with a new tool that has been used to study the dynamics of turbulence in great detail. In some cases these calculations have provided information that would be difficult or impossible to obtain from experiments and in other cases they have provided new results that were latter confirmed by experiments. At the Naval Research Laboratory, we have recognized that DNS may provide new insights into problems that are of particular interest to the Navy. Problems to which DNS may be applied in the future include investigations of the sources of turbulent flow noise, the physics of polymer-induced drag reduction, and turbulence-free surface interactions. However, in order to embark on a detailed study of any of these complex problems, it is first necessary to establish confidence in our ability to perform meaningful simulations of turbulence in relatively simple cases.

The channel geometry has been chosen by many investigators as a starting point for DNS wall-bounded shear flow calculations because of both its geometrical simplicity and the ease with which it can be handled numerically. However, in spite of its simplicity, intense investigations of the high resolution calculations of Kim, Moin and Moser(1987) (KMM) , for example, have yet to unequivocably unravel the spatial and temporal evolution of the coherent vortical structures which experimental evidence suggests have their origin near the wall. Therefore, the complex physics of even this simple wall-bounded shear flow, it seems, warrants continued intensive investigation in the hope that such studies may reveal more details of fundemental wall turbulence phenomena of which, perhaps the most important is the nature of the Reynolds stress producing events. We have therefore undertaken, in the last few years, an effort in DNS which parallels, in some respects, the efforts of other groups for the purpose of eventually applying these methods to attack the more complex problems mentioned above. In this report we review the progress that has recently been made at NRL in moderate

---

Manuscript approved December 8, 1988.

resolution, low Reynolds number DNS channel flow calculations. In the future we will report on progress that has been made in applying DNS to more complicated geometries and on the results of higher resolution calculations.

In Section 2 we review the numerical methods that have been used to perform DNS calculations of turbulence. In particular, we discuss the difficulties associated with operator splitting methods and the methods that have been devised, such as Green function methods, for overcoming operator splitting errors. We also propose a modification of the original Green function method devised by Marcus(1984) which we will analyze and test in future investigations. We also discuss methods that have been devised to solve the equations of motion without resort to splitting. We conclude Section 2 with a review of the computer codes that we have used and note the algorithms upon which each is based. We have created numerous datasets which cover differing length and time scales which can be used for distinctly different purposes. The attributes of each dataset is listed at the end of Section 2.

In Section 3 we discuss one and two point statistics from several datasets and also present some preliminary conditional sampling results. We find that in spite of the low resolution of our calculations, our results compare well in most respects to the higher resolution calculations of KMM and also with experiments. We note, however, that our computations give somewhat lower intensities and somewhat longer streamwise length scales than the KMM results. We speculate on several possible reasons for these differences.

We also include, in Appendix A, a discussion of the effects of aliasing errors on the long-time behavior of the calculations. We present evidence that the numerical solutions to the Navier-Stokes equations may be severely and adversely affected by aliasing errors. The evidence presented indicates that if these errors are not removed, the solution reaches a chaotic steady state which is remarkably similar to a weak transitional turbulent flow. That is, we have found that aliasing errors have a damping effect on the turbulence which has yet to be understood.

2. A Review of Numerical Methods

Here we review the principal numerical methods that have been employed in the direct numerical simulation of turbulence by numerous investigators over the past decade. We place special emphasis on a review of the methods that have been used in the simulation of wall bounded turbulence. Orszag and Patterson (1973) performed the first simulation of homogenous isotropic turbulence which required 32^3 grid points. A spectral Galerkin approach was employed in which trigonometeric functions were used. The next major direct simulation was the turbulent channel flow calculation of Orszag and Kells(1980) and Orszag and Patera(1983). In these simulations one homogenous coordinate using trigonometric functions was replaced by Chebyshev polynomials. In the first paper. the problem of transition to turbulence in a channel geometry was studied, and in the second, the study was extended to turbulent flow. At the same time there was work being done at NASA Ames (Kim and Moin(1982)) and other institutions on large eddy simulations (LES). LES involves many of the same numerical techniques, but includes a term in the Navier-Stokes equations which models the unresolved turbulent length scales.

The next major step in direct simulations was taken by Marcus (1984) and Schumann (1985). This improvement involves the use of Green functions or so-called influence matrix methods to improve the implementation of the boundary conditions. This method improves the convergence properties of the earlier methods and will be discussed in detail shortly. Marcus applied this method to the Taylor-Couette problem and satisfactorily predicted wave speeds. Schumann applied his version of this method to turbulent channel flow.

There are difficulties in the above methods related to satisfying the incompressibility condition which cannot easily be overcome. An alternative is to rewrite the Navier-Stokes equations as a fourth-order equation for the normal velocity and a second-order equation for the normal vorticity. In this form. the equations are more difficult to solve, but incompressibilty is satisfied implicitly.

2.1 Governing Equations and the Channel Flow Geometry

We are particularly interested in studying turbulent flow between two rigid parallel walls. This choice represents a compromise between scientific interest and numerical effort. The streamwise coordinate is x or x_1, the wall normal coordinate is y or x_2 and the spanwise coordinate is z or x_3. The computational domain used throughout this work, in terms of channel half-widths, is 2 in the wall normal direction and 5 in both the streamwise and spanwise directions. All calculations are performed with Chebyshev polynomials in the wall normal direction and Fourier series in the streamwise and spanwise directions.

The governing equations for this problem are the Navier-Stokes equations in the so-called rotational form:

$$\frac{\partial \mathbf{u}}{\partial t} = \mathbf{u} \times \boldsymbol{\omega} - \boldsymbol{\nabla}(p + \frac{\mathbf{u} \cdot \mathbf{u}}{2}) + \frac{1}{Re}\nabla^2 \mathbf{u} + \mathbf{f}, \tag{2.1}$$

and the continuity equation,

$$\boldsymbol{\nabla} \cdot \mathbf{u} = 0. \tag{2.2}$$

In these equations, $p + \frac{\mathbf{u} \cdot \mathbf{u}}{2}$ is the dynamic pressure head, Re is the Reynolds number based on channel half-width and friction velocity, and $\mathbf{f}$ is a body force.

It is possible to eliminate the pressure from the above equations. This results in the fourth order equation:

$$\frac{\partial}{\partial t}\nabla^2 u_2 = N_u + \frac{1}{Re}\nabla^4 u_2, \tag{2.3}$$

where

$$N_u = (\frac{\partial^2}{\partial x_1^2} + \frac{\partial^2}{\partial x_3^2})(\mathbf{u} \times \boldsymbol{\omega})_2 - \frac{\partial}{\partial x_2}\{\frac{\partial}{\partial x_1}(\mathbf{u} \times \boldsymbol{\omega})_3 + \frac{\partial}{\partial x_3}(\mathbf{u} \times \boldsymbol{\omega})_1\}$$

for the normal velocity. In addition there is a second order equation for the normal vorticity:

$$\frac{\partial}{\partial t}\omega_2 = N_{\omega_2} + \frac{1}{Re}\nabla^2\omega_2, \tag{2.4}$$

with

$$N_{\omega_2} = \frac{\partial}{\partial x_3}(\mathbf{u}\times\ \boldsymbol{\omega})_1 - \frac{\partial}{\partial x_1}(\mathbf{u}\times\ \boldsymbol{\omega})_3.$$

In this formulation the flow conserves mass implicitly.

For all the schemes, no-slip boundary conditions are imposed at the walls. From the continuity equation it follows that an additional boundary condition at the walls,

$$\frac{\partial u_2}{\partial x_2} = 0 \text{ on } x_2 = \pm 1,$$

can be derived. This boundary condition is needed when solving the fourth order equation for the normal velocity. In the streamwise and spanwise direction the use of trigonometric functions requires periodic boundary conditions.

There are several ways to non-dimensionalize the Navier-Stokes equations. The two methods used currently are inner scaling and outer scaling whose definitions are given in Table 2.1. When describing turbulent physics close to a wall the only parameters available that can be used to form length and time scales are the viscosity and the wall shear stress. For inner variable scaling we define the friction velocity, u^*, a length scale, l^*, and a friction or wall Reynolds number, R^*. This scaling is the appropriate one when discussing the flow behavior in the viscous sublayer, the buffer layer and to some extent the logarithmic layer.

When describing the physics far from the wall, outer scaling is used. In turbulent channel flow the outer scales are usually taken to be the mean centerline velocity, U_{cl}, and the channel half-width, L_2. Outer scaling is appropriate when discussing the large scale properties of the flow. In the current state of direct simulation, the core region of the flow is small and this scaling is not as effective as inner scaling. In turbulent transition studies outer scaling, however, is more appropriate.

Table 2.1
Non-dimensionalizations

Variable	Inner Scaling	Outer Scaling
Velocity	$u^* = \sqrt{\nu \frac{\partial u}{\partial x_2}\|_{wall}}$	U_{cl}
Length	$l^* = \sqrt{\frac{\nu}{\frac{\partial u}{\partial x_2}\|_{wall}}}$	L_2
Viscosity	ν	ν
Reynolds Number	$R^* = \frac{u^* L_2}{\nu}$	$Re = \frac{U_{cl} L_2}{\nu}$

When inner scaling is used, the driving force can be related to the mean wall shear stress (and the friction velocity) in the sense that the wall shear stress will converge asymptotically to or rather oscillate about a mean value. The wall shear stress and the friction velocity can be related to the driving force in the following manner:

$$u^{*2} = \nu \frac{\partial u}{\partial x_2}\Big|_w = \frac{dP_0}{dx_2}$$

where P_0 is the static pressure. A large scale velocity is not specified since it is not needed. When outer scaling is used this relationship must hold, but there is the additional need to specify a large scale velocity. Since there is no unique relationship between the mean turbulent centerline velocity and the wall shear stress, the most natural velocity to choose is the initial mean centerline velocity. Since our main interest is fully developed turbulence and not turbulent transition, all further discussions will be in the context of inner scaling.

2.2 Time Stepping Methods

The incompressible Navier-Stokes equations form a non-linear coupled set of partial differential equations. There are two major difficulties with these equations when trying to select a time-stepping scheme: the non-linearity of the convective term and the enforcement of the incompressibility condition. These two problems are handled in very different ways. The extreme complexity of the non-linear term makes treating it implicitly very unattractive so that it is generally handled with an explicit or so-called semi-implicit numerical method.

The second problem, enforcing incompressibility, is equivalent to solving the time dependent Stokes problem. The Stokes problem is the Navier-Stokes problem with the incompressibilty equation but with no convective term. The statement of this problem is given as follows:

$$\frac{\partial \mathbf{u}}{\partial t} = -\,\nabla p + \frac{1}{Re}\nabla^2 \mathbf{u}, \tag{2.5}$$

$$\nabla \cdot \mathbf{u} = 0 \tag{2.6}$$

and

$$\mathbf{u} = 0 \text{ on } x_2 = \pm 1. \tag{2.7}$$

There are two methods for dealing with this problem: the split schemes and the unsplit schemes. In the split schemes the coupled linear Stokes equations are separated into a pressure step and a viscous step. The incompressibility condition is enforced during the pressure step. In the unsplit schemes a fourth order equation for the vertical velocity is formed. It satisfies the incompressibility condition implicitly. Note that even the unsplit scheme requires the splitting off of the non-linear terms. The 'split' or 'unsplit' character of a scheme in the context of this paper refers only to the algorithm used to solve the Stokes problem. A variety of split schemes are used in the computer codes for turbulence simulation now operational at NRL and a code using the unsplit scheme is now under development.

2.2.1 Time Split Methods

The motivation for using the split scheme is numerical simplicity and efficiency. It involves reducing a complicated set of coupled equations into a simpler set. Unfortunately, the simplification occurs at the expense of an improper implementation of the boundary conditions. In the Stokes problem described above, the pressure field exists to satisfy the incompressibility condition. Each of the time-dependent equations is a second order equation with two boundary conditions: the zero velocity condition at $x_2 = \pm 1$. They form a coupled, but closed set of equations. We do not wish to solve this coupled set of equations.

The Stokes problem can be simplified by splitting it in two parts as follows:

The incompressibility step is,

$$\frac{\partial \mathbf{u}}{\partial t} = - \boldsymbol{\nabla} p. \tag{2.8}$$

$$\boldsymbol{\nabla} \cdot \mathbf{u} = 0. \tag{2.9}$$

and the viscous step is

$$\frac{\partial \mathbf{u}}{\partial t} = \frac{1}{Re} \nabla^2 \mathbf{u}. \tag{2.10}$$

$$\mathbf{u} = 0 \text{ on } x_2 = \pm 1. \tag{2.11}$$

The splitting scheme introduces distinct time stepping errors (Orszag, Israeli and Deville 1987) which dominate those of the viscid or inviscid problems. Therefore there is no advantage in specifying a high order time stepping scheme. In addition, the steep spatial gradients near the walls require a fine mesh and these terms must by handled implicitly in order to avoid a strong time step constraint. Typically, an Adams-Bashforth scheme is used for the nonlinear terms and an implicit Euler method for the linear terms. A Crank-Nicholson scheme may also be used.

We note that boundary conditions have not yet been specified for the incompressibility step. The only proper boundary condition is the no-slip condition imposed after the pressure step (Marcus, 1984). However, a boundary condition must be specified at the intermediate step. In this step there are four equations for four unknowns and they can be solved for a single variable which is either pressure or normal velocity. Solving for the pressure field results in a Neumann problem while solving for the normal velocity leads to a Dirichlet problem. There is no difficulty in specifying the boundary conditions for the linear viscous step.

A. Dirichlet Methods

The original Orszag-Kells(1980) algorithm for simulating turbulence between flat plates uses a normal velocity formulation to satisfy the incompressibility condition. The semi-implicit Adams-Bashforth Crank-Nicholson scheme, which will be described later, is used to treat the non-linear term. A backward Euler scheme is used in the pressure and viscous steps. Due to a strong memory constraint, an explicit Adams-Bashforth scheme is used in all the algorithms discussed in this work, although the treatment of the non-linear term is still under study. When the non-linear terms are included, the three steps in the algorithm can be written as follows:

(a)the non-linear step:

$$\frac{\hat{\mathbf{u}} - \mathbf{u}^n}{\Delta t} = \frac{3}{2}\mathbf{F}^n - \frac{1}{2}\mathbf{F}^{n-1} \tag{2.12}$$

where

$$\mathbf{F} = \mathbf{u} \times \omega + \mathbf{f}$$

(b) the pressure step:

$$\nabla^2 \hat{\hat{u}}_2 = \left(\frac{\partial^2}{\partial x_1^2} + \frac{\partial^2}{\partial x_3^2}\right)\hat{u}_2 - \frac{\partial}{\partial x_2}\left(\frac{\partial}{\partial x_1}\hat{u}_1 + \frac{\partial}{\partial x_3}\hat{u}_3\right) \tag{2.13}$$

$$\hat{\hat{u}}_2 = 0 \text{ on } x_2 = \pm 1.$$

and (c)the viscous step:

$$\frac{\mathbf{u}^{n+1} - \hat{\hat{\mathbf{u}}}}{\Delta t} = \frac{1}{Re}\nabla^2 \mathbf{u}^{n+1} \tag{2.14}$$

$$\mathbf{u}^{n+1} = 0 \text{ on } x_2 = \pm 1.$$

Note that only during the intermediate pressure/continuity step is the continuity equation satisfied, while only at the end of the viscous step are the boundary conditions properly satisfied. This inconsistency can be seen by examining the normal momentum equation of the continuity step:

$$\hat{\hat{u}}_2 = \hat{u}_2 - \Delta t \frac{\partial}{\partial x_2}\hat{\Pi}^{n+1}, \tag{2.15}$$

where $\Pi = p + \frac{\mathbf{u}\cdot\mathbf{u}}{2}$, which implies that at the walls

$$\frac{\partial}{\partial x_2}\hat{\Pi}^{n+1} = \frac{\hat{u}_2}{\Delta t} \text{ on } x_2 = \pm 1. \tag{2.16}$$

This is not consistent with the Navier-Stokes equations for the normal momentum evaluated at the walls and has the effect of introducing spurious pressure forces at the walls.

B. Neumann Methods

A boundary condition for the pressure field can be developed based on the assumption that at high Reynolds numbers, the inviscid boundary conditions are good approximations. From the Navier-Stokes equation in the wall-normal direction the following boundary condition can be developed:

$$\frac{\partial}{\partial x_2}\Pi = \frac{1}{Re}\frac{\partial^2}{\partial x_2^2}u_2 \text{ on } x_2 = \pm 1, \tag{2.17}$$

which in the inviscid limit becomes

$$\frac{\partial}{\partial x_2}\Pi = 0 \text{ on } x_2 = \pm 1. \tag{2.18}$$

The complete algorithm is given by:

(a) the non-linear step:

$$\frac{\hat{\mathbf{u}} - \mathbf{u}^n}{\Delta t} = \frac{3}{2}\mathbf{F}^n - \frac{1}{2}\mathbf{F}^{n-1}, \tag{2.19}$$

(b) the pressure step:

$$\nabla^2 \Pi^{n+1} = \nabla \cdot \frac{\hat{\mathbf{u}}}{\Delta t} \tag{2.20}$$

$$\frac{\partial \Pi^{n+1}}{\partial x_2} = 0 \text{ on } x_2 = \pm 1,$$

and (c) the viscous step:

$$\frac{\mathbf{u}^{n+1} - \hat{\hat{\mathbf{u}}}}{\Delta t} = \frac{1}{Re}\nabla^2 \mathbf{u}^{n+1} \tag{2.21}$$

$$\mathbf{u}^{n+1} = 0 \text{ on } x_2 = \pm 1.$$

From (2.20), the pressure boundary condition implies

$$\hat{\hat{u}}_2 = \hat{u}_2 \text{ on } x_2 = \pm 1. \tag{2.22}$$

We find, therefore, that there is a fictitious flow through the boundary during the incompressibility step. One way to avoid this difficulty is by using a Green function approach.

C. Green Function Methods

The difficulty with the Orszag-Kells algorithm is the lack of proper boundary conditions at the intermediate pressure step. In an attempt to minimize the errors induced by these difficulties, Marcus (1984) developed a Green function method to add a correction to the calculated pressure field. He solved the incompressibility step for the pressure and made the observation that the pressure step is a linear non-homogeneous problem with non-homogeneous boundary conditions. The solution can then by divided into three parts: one which satisfies the inhomogeneous equation with homogeneous boundary conditions and two other solutions which satisfy the homogeneous equation with non-homogeneous boundary conditions. Let

$$\Pi^{n+1} = \bar{\Pi}^{n+1} + \Pi_c^{n+1} \tag{2.23}$$

where $\bar{\Pi}^{n+1}$ is the solution to

$$\Delta t \nabla^2 \bar{\Pi}^{n+1} = \nabla \cdot \hat{u}, \tag{2.24}$$

subject to

$$\bar{\Pi}^{n+1} = 0 \text{ on } x_2 = \pm 1, \tag{2.25}$$

and

$$\nabla^2 \Pi_c = 0 \tag{2.26}$$

subject to inhomogenous boundary conditions at the upper and lower boundaries. The boundary conditions for the pressure correction can be found by substituting (2.23) into (2.20) and evaluating them at the walls subject to

$$u_2^{n+1} = 0 \text{ on } x_2 = \pm 1. \tag{2.27}$$

This leads to the following condition:

$$\Delta t \frac{\partial}{\partial x_2} \Pi^{n+1} = \hat{u}_2 + \frac{\Delta t}{Re} \nabla^2 u_2^{n+1}, \text{ on } x_2 = \pm 1. \tag{2.28}$$

or

$$\Delta t \frac{\partial}{\partial x_2} \Pi_c^{n+1} = \hat{u}_2 + \frac{\Delta t}{Re} \nabla^2 u_2^{n+1} - \Delta t \frac{\partial}{\partial x_2} \bar{\Pi}^{n+1}, \text{ on } x_2 = \pm 1. \tag{2.29}$$

Note that u_2^{n+1} is not known during the incompressibility step. However, Marcus asserts that this boundary condition is true if and only if:

$$\nabla \cdot \mathbf{u}^{n+1} = 0, x_2 = \pm 1. \tag{2.30}$$

To satisfy these boundary conditions, the Laplace equation for the pressure corrections is solved for arbitrary Dirichlet boundary conditions. The solution can be written as (following Marcus' notation):

$$\Pi_c^{n+1}(x_2, k_{x_1}, k_{x_3}) = a_1^{n+1}(k_{x_1}, k_{x_3})\chi_1(x_2, k_{x_1}, k_{x_3}) + a_2^{n+1}(k_{x_1}, k_{x_3})\chi_2(x_2, k_{x_1}, k_{x_3}) \tag{2.31}$$

where χ_1 and χ_2 are solutions to the Laplace equation with the following boundary conditions:

$$\chi_1 = \begin{cases} 1, & x_2 = 1; \\ 0, & x_2 = -1, \end{cases} \tag{2.32}$$

and

$$\chi_2 = \begin{cases} 0, & x_2 = 1; \\ 1, & x_2 = -1. \end{cases}$$

Note that they are independent of the fluid flow and need to be calculated only once. Then let

$$\hat{\hat{u}} = \bar{\hat{\hat{u}}} + \hat{\hat{u}}_c, \tag{2.33}$$

where

$$\bar{\hat{\hat{u}}} = \hat{u} - \Delta t \ \nabla\bar{\Pi}^{n+1}, \tag{2.34}$$

and

$$\hat{\hat{u}}_c = -\Delta t \ \nabla\Pi_c^{n+1}. \tag{2.35}$$

The final viscous step is

$$u_2^{n+1} = [1 - \frac{\Delta t}{Re}\nabla^2]^{-1}\bar{\hat{\hat{u}}}_2 + [1 - \frac{\Delta t}{Re}\nabla^2]^{-1}\hat{\hat{u}}_c, \tag{2.36}$$

where

$$u_1^{n+1} = [1 - \frac{\Delta t}{Re}\nabla^2]^{-1}\hat{\hat{u}}_1,$$

and

$$u_3^{n+1} = [1 - \frac{\Delta t}{Re}\nabla^2]^{-1}\hat{\hat{u}}_3.$$

The operator $1 - \frac{\Delta t}{Re}\nabla^2$ is inverted using the proper Dirichlet boundary conditions. The remaining undetermined coefficients a_1^{n+1} and a_2^{n+1} are found by applying the boundary condition given by (2.27).

D. A Proposed Alternate Green Function Method

The Green function formulation developed by Marcus is only a correction to the splitting algorithm and still suffers from one of the main difficulties associated with splitting schemes. Since the Navier-Stokes equations consist of three second order operators (three momentum equations) they form a sixth-order system and therefore require six boundary conditions for their solution. In the time splitting algorithms there are usually four second-order operators with a total of eight boundary conditions which must be solved. The Marcus correction improves the splitting algorithm, but does not correct this problem.

The following algorithm is an attempt to solve this problem. The proposed algorithm requires six boundary conditions and only three Poisson equation inversions. It has not been implemented to the best of our knowledge nor has the algorithm been analyzed for stability or accuracy. The algorithm is similar to that of Marcus in its use of Green functions. It is included here since it may be the basis of transition calculations using non-Newtonian constitutive equations. In the next section an algorithm will be presented which is better than the split algorithms but it should be recognized that for complex non-linear constitutive equations in non-Newtonian flows a split scheme may be more manageable.

The objective is to solve for the normal velocity in the continuity and viscous steps using both zero flow and zero flux boundary conditions applied after the viscous step. This can be accomplished through the use of Green functions which couple these two steps through the boundary conditions. The Green functions must be evaluated and the accompanying coefficients must be determined to satisfy the boundary conditions. The updated streamwise and spanwise velocities can then be computed at the continuity step. No boundary conditions will be imposed at this step. The remaining two equations in the viscous step for the spanwise and streamwise velocity can be combined to form an equation for the normal vorticity. Solving for the normal vorticity requires only one Poisson inversion and two boundary conditions. The boundary conditions can be derived from the remaining no-slip boundary conditions. The application of two sets of boundary conditions in the normal velocity problem is not improper since two sets of second order problems are being solved. The result is the same order as the original problem and there is no need to invent boundary conditions for the pressure field. By solving the problem in this fashion, a boundary condition for the pressure field is never specified. The use of a no flux boundary condition is consistent with enforcing continuity at the wall. The accuracy and stability of this scheme has not yet been determined. The Green function code currently being used will be modified to test this algorithm.

2.2.2 Time Unsplit Methods

The unsplit schemes are preferable in that they satisfy continuity implicitly and the normal velocity and normal vorticity are uncoupled if the non-linear terms are neglected. The fourth- order problem is solved using several auxiliary problems and the second-order problem for vorticity is solved directly. This formulation was first discussed by Orszag and Patera (1983) and later implemented in a simpler form in the large-scale direct simulations by Kim, Moin and Moser (1987). It is the latter formulation that will be used.

Using the Crank-Nicholson scheme for the linear terms and the Adams-Bashforth scheme for the non-linear terms, (2.3) and (2.4) can be rewritten as

$$(1 - \frac{\Delta t}{2Re}\nabla^2)\nabla^2 u_2^{n+1} = (1 + \frac{\Delta t}{2Re}\nabla^2)\nabla^2 u_2^n + \frac{\Delta t}{2}(3N_{u_2}^n - N_{u_2}^{n-1}), \qquad (2.37)$$

and

$$(1 - \frac{\Delta t}{2Re}\nabla^2)\omega_2^{n+1} = (1 + \frac{\Delta t}{2Re}\nabla^2)\omega_2^n + \frac{\Delta t}{2}(3N_{\omega_2}^n - N_{\omega_2}^{n-1}), \qquad (2.38)$$

where the known terms have been moved to the the right hand side. These equations are subject to the boundary conditions:

$$u_2 = \frac{\partial u_2}{\partial x_2} = \omega_2 = 0 \text{ on } x_2 = \pm 1. \tag{2.39}$$

The vorticity problem is an inhomogeneous Poisson problem with homogeneous boundary conditions. It can be solved relatively easily. A Chebyshev-Tau method will be used. The vertical velocity problem can be solved if it is broken into a homogeneous problem and two inhomogenous problems:

$$u^{n+1} = u_p^{n+1} + \alpha^+ u_+^{n+1} + \alpha^- u_-^{n+1}, \tag{2.40}$$

which satisfy the conditions

$$u_p = u_+ = u_- = 0 \text{ on } x_2 = \pm 1, \tag{2.41}$$

and

$$\frac{\partial}{\partial x_2}(u_p + \alpha^+ u_+ + \alpha^- u_-) = 0 \text{ on } x_2 = \pm 1. \tag{2.42}$$

To solve these problems, introduce the auxiliary variable ζ such that

$$\zeta^{n+1} = \nabla^2 {u_2}^{n+1}. \tag{2.43}$$

Then the particular problem is

$$(1 - \frac{\Delta t}{2Re}\nabla^2)\zeta_p^{n+1} = (1 + \frac{\Delta t}{2Re}\nabla^2)\zeta^n + \frac{\Delta t}{2}(3N_u^n - N_u^{n-1}), \tag{2.44}$$

and

$$\nabla^2 u_p^{n+1} = \zeta_p^{n+1}, \tag{2.45}$$

subject to

$$u_p^{n+1} = 0 \text{ on } x_2 = \pm 1, \tag{2.46}$$

and

$$\zeta_p^{n+1} = 0 \text{ on } x_2 = \pm 1. \tag{2.47}$$

Then the particular problem for satisfying the upper boundary condition is

$$(1 - \frac{\Delta t}{2Re}\nabla^2)\zeta_+^{n+1} = 0, \tag{2.48}$$

and

$$\nabla^2 u_+^{n+1} = \zeta_+^{n+1}, \tag{2.49}$$

subject to

$$u_+^{n+1} = 0 \text{ on } x_2 = \pm 1, \tag{2.50}$$

with

$$\zeta_+^{n+1} = \begin{cases} 1, & \text{if } x_2 = 1; \\ 0, & \text{if } x_2 = -1. \end{cases} \tag{2.51}$$

Then the particular problem for satisfying the lower boundary condition is

$$(1 - \frac{\Delta t}{2Re}\nabla^2)\zeta_-^{n+1} = 0, \tag{2.52}$$

and

$$\nabla^2 u_-^{n+1} = \zeta_-^{n+1}, \tag{2.53}$$

subject to

$$u_-^{n+1} = 0 \text{ on } x_2 = \pm 1, \tag{2.54}$$

$$\zeta_-^{n+1} = \begin{cases} 0, & \text{if } x_2 = 1; \\ 1, & \text{if } x_2 = -1. \end{cases} \tag{2.55}$$

Given the solutions to the auxillary problems, (2.42) can be used to find the unknown coefficients α^+ and α^-.

2.3 The Non-Linear Term

Treatment of the non-linear term in the Navier-Stokes equation has two difficulties. The first is the evaluation of its spatial character. Originally, Orszag and Kells(1980) suggested the use of the so-called rotational form of the Navier-Stokes equations in which the non-linear term is written as $\mathbf{u} \times \boldsymbol{\omega}$. The objective was to recast the non-linear term in a quasi-conservative form as suggested by Fornberg(1973). If the calculation is not dealiased this form may not be quasi-conservative. As discussed in Appendix A, the use of this term with and without the aliasing terms leads to significantly different results. Horiuti (1987) and Zang(1988) have studied this problem numerically and both suggest that if the calculation is not de-aliased then there are better forms for the non-linear term than the rotational form. All the simulations currently being preformed at NRL are de-alaised.

As discussed earlier, there are two different time stepping schemes used for the non-linear term. If the non-linear portion of the time split Navier-Stokes equations is written as

$$\frac{\partial \mathbf{u}}{\partial t} = \mathbf{u} \times \boldsymbol{\omega}, \tag{2.56}$$

then straight forward application of the Adams-Bashforth scheme is

$$\frac{\hat{\mathbf{u}} - \mathbf{u}^n}{\Delta t} = \frac{3}{2}\mathbf{F}^n - \frac{1}{2}\mathbf{F}^{n-1}, \tag{2.57}$$

where $\mathbf{F}$ is the non-linear term. In order to reduce the convective instability of this step Orszag and Kells (1980) suggested rewriting the non-linear step by adding $U(x_2)\frac{\partial \mathbf{u}}{\partial x_1}$ to both sides of (2.56). The left hand side is treated using the Crank-Nicolson implicit scheme and the right hand side by the Adams-Bashforth scheme. The resulting time stepping equations are:

$$\frac{\hat{\mathbf{u}} - \mathbf{u}^n}{\Delta t} = \frac{3}{2}\mathbf{F}^n - \frac{1}{2}\mathbf{F}^{n-1} - \frac{1}{2}U(x_2)(\frac{\partial \hat{\mathbf{u}}^{n+1}}{\partial x_1} - 2\frac{\partial \hat{\mathbf{u}}^n}{\partial x_1} + \frac{\partial \hat{\mathbf{u}}^{n-1}}{\partial x_1}). \tag{2.58}$$

Note that the semi-implicit scheme requires an additional six variables. If the intermediate results $\hat{\mathbf{u}}^n$ and $\hat{\mathbf{u}}^{n-1}$ are not used the order of accuracy is reduced to $O(\Delta t)$. Due to the large memory requirement, this scheme is not usually used.

2.4 Spectral Methods

Here we give only a brief summary of spectral methods necessary to describe the different computer codes currently at NRL. The reader is referred to several complete reviews of spectral methods (Gottlieb and Orszag, 1978, Gottlieb, et al., 1984 and Canuto, et al. 1988) for more detailed descriptions.

The Navier-Stokes equations are discretized in the planes parallel to the walls using a Fourier pseudo-spectral scheme. In the direction normal to the channel walls Chebyshev polynomials are used. Neumann or Dirichlet boundary conditions can be imposed at the wall. In the flow direction and in the spanwise direction periodic boundary conditions are used and this facilitates the use of a trigonometric Fourier series in these directions. The velocity field is represented as

$$\mathbf{u}(\mathbf{x},t) = \sum_{m=-M}^{M-1} \sum_{n=-N}^{N-1} \sum_{p=1}^{P} \tilde{\mathbf{u}}(m,n,p,t) \exp(i(\alpha m + \beta n)) T_p(x_2), \qquad (2.59)$$

where $\alpha = \frac{2\pi}{L_{x_1}}$, $\beta = \frac{2\pi}{L_{x_3}}$, and $i = \sqrt{-1}$.

The algorithms described above require at least four Poisson solutions. For example in the Dirichlet/normal velocity formulation a Poisson equation is inverted for the normal velocity in the pressure step and three Poisson equations are inverted during the viscous step to update the three velocities. In the operational computer codes at NRL two different methods are used in inverting the Poisson equation. They are the collocation and the tau methods. In the collocation method an interpolating polynomial is used to convert continuous equations in space to discrete equations. It can be shown that this is formally equivalent to taking a discrete cosine transform of the data at the collocation points. If $\mathbf{C}$ is the matrix representation for the discrete Fourier transform, $\mathbf{C}^{-1}$ its inverse and $\mathbf{D}$ the discrete derivative operator in matrix form (Gottleib, et al. 1984), then the matrix operator, $\mathbf{M}$, which takes a real space function into the derivative of the real space function is:

$$\mathbf{M} = \mathbf{C}^{-1}\mathbf{D}\mathbf{C}$$

, and the second derivative operator is simply

$$\mathbf{M}\mathbf{M}.$$

The boundary conditions can be built into this matrix and the solution to the Poisson equation is the solution to:

$$\mathbf{M}^2\mathbf{u} = \mathbf{s},$$

where $\mathbf{u}$ is the solution and $\mathbf{s}$ is some source term. Since $\mathbf{MM}$ is a full matrix, normal numerical methods are not effective. Haidvogel and Zang (1978) describe a method of decomposing the full matrix into eigenvalues and eigenvectors. Then the inversion becomes a simple matter of matrix multiplication. After the decomposition, this method is fast and retains the infinite order accuracy of spectral methods.

In the Tau method, the solution to a problem with its boundary conditions is represented with $n+k$ expansion functions. The coefficients are found using n equations derived from the governing equations and k equations derived from the k boundary conditions. The solution is represented in Fourier-Chebyshev coefficients. In the case of the x_2 direction, the Poisson equation can be rewritten as a quasi-tridiagonal system that can be efficiently solved with a modified Gaussian elimination algorithm. The boundary conditions are explicitly built into the matrix operator.

2.5 Computer Codes and Data Sets

There are four operational computer codes for the direct simulation of turbulence in a channel currently in use at NRL. The first two listed in Table 2.2 were written by Orszag and his students using the Orszag-Kells algorithm (Dirichlet boundary conditions in the pressure step). In the first program, a very clever method is used to manage the memory and input-output (i/o). Only a quarter of the computational domain is in computer memory at any time, and to prevent wasted i/o time this time had to be minimized and carefully overlaid by concurrent cpu time. In the second and remaining computer codes, the data is always resident in the computer memory. The last two operational computer codes were developed by John McLaughlin (Clarkson University), and extensively updated by and obtained from Steven Lyons and Thomas

Hanratty (University of Illinois). The fourth computer code uses the Green function algorithm developed by Marcus.

Table 2.2

Computer Codes For Turbulent Channel Flow

Number	Split/Unsplit	Boundary Conditions	Memory	Status	Author
1	Split	Dirichlet	Out of Core	Operational	†
2	Split	Dirichlet	In Core	Operational	‡
3	Split	Neumann	In Core	Operational	○
4	Split	Neumann with Green's Functions	In Core	Operational	○
5	Split	Neumann with Green's Functions	In Core	Under Development	◇
6	Fourth Order	Dirichlet and Neumann	In Core	Under Development	●

† Orszag, Kells and Patera

‡ Orszag, Bullister and Pelz

○ McLaughlin

◇ Leighton and Handler

● Handler, Leighton, Swean and Wang

There are two channel codes under development at NRL. The first is an adaptation of code 4 using the alternate Green Function algorithm described in Section 2.2.1.d. The second and more important one is based on the fourth order algorithm. Much of the work for both has been completed, and both should be in the testing phase by the end of calender year 1988.

Currently, there are four distinct datasets which exist or will exist in the near future. Each of these datasets may have more than one entry which will depend on the resolution in time. There are an additional two datasets, A and DAG. The former was a high resolution simulation which still contained aliasing errors. See Handler, Leighton and Carroll(1987) for a discussion of this dataset. Program 4 was run for a short time ($100t*$), in order to develop data for determining mean statistics. The short run time will have an effect on the mean statistics, but is long enough to get a fair idea of the flow properties. The remaining datasets are to be written to tape using the PDSDUMP routine on the Cray and can be brought up when needed.

In the datasets Chan2 and Chan3, the difference in time scales between entries was chosen to be about a factor of ten. The Chani.1, i=1-3 dataset are used for documenting the long time averages, evaluation the proper orthogonal decomposition, and similar processes where statistically independent realizations are needed. The Chani.2 datasets are for use in conditional sampling, flow visualization and for following the general evolution of the flow. Dataset Chan4.1 and Chani.3 , i=2,3 are for following the details of temporal evolution.

Table 2.3

Data Sets For Turbulent Channel Flow

Name	Domain † (y,z,x)	Resolution (Ny,Nz,Nx)	R*	Δt ○	Program	Status	Notes
A ÷	2.5.5	65.128.64	165	--	1	deleted	Highly Aliased
Chan1.1‡	2.5,5	33,64.16	125	100	3	exists	28 realizations
Chan1.2	2.5,5	33,64.16	125	1	3	exists	2800 realizations ◇
DAG	2.5,5	33,64.16	125	1	4	exists	Diagnostics only
Chan2.1	2.5,10	33,64,32	125	50	4	exists	50 realizations
Chan2.2	2,5,10	33,64,32	125	2	4	exists	500 realizations
Chan2.3	2.5,10	33,64,32	125	0.2	4	exists	128 realizations
Chan3.1	2.5,10	65,64,64	150	50	4	planned	50 realizations
Chan3.2	2.5,10	65,64,64	150	2	4	planned	500 realizations
Chan3.3	2.5,10	65,64,64	150	0.2	4	planned	128 realizations
Chan4.1	2.5,5	65,64,32	125	0.1	4	exists	200 realizations

† Based on channel half width, $x_2 \times x_1 \times x_3$.

◇ Planar Data Only.

○ Time between realizations, all datasets three dimensional except Chan1.2.

‡ Also called DA in text.

÷ See Handler, Leighton and Carroll (1987)

3. Results

3.1 One-point statistics

In this section we will compare the one-point statistics computed from the the dealiased (DA) and the dealiased-Green function (DAG) datasets, whose characteristics have been disscussed in Section 2.5, with experimental data and with the KMM results. For any given component of velocity (or vorticity), which we will designate as u for convenience, we compute the mean value, $\overline{u}$, the mean-square value, $\overline{u^2}$, the skewness, $\overline{u^3}$, and the flatness, $\overline{u^4}$, as follows:

$$\overline{u}(x_2) = 1/N \sum_{j=1}^{N} < u^j >, \tag{3.1}$$

$$\overline{u^2}(x_2) = 1/N \sum_{j=1}^{N} < (u^j - < u^j >)^2 >, \tag{3.2}$$

$$\overline{u^3}(x_2) = 1/N \sum_{j=1}^{N} < (u^j - < u^j >)^3 >, \tag{3.3}$$

and

$$\overline{u^4}(x_2) = 1/N \sum_{j=1}^{N} < (u^j - < u^j >)^4 >, \tag{3.4}$$

where $<>$ signifies averaging over a horizontal plane and the index j identifies each of the N realizations of the flow. Unless otherwise noted, we use the friction velocity, u^*, and the viscous length, l^*, as defined in Section 2.1 to make all variables in this and subsequent sections nondimensional. We use the convention that any variable with a raised asterisk has been made nondimensional using viscous units.

A typical turbulent velocity profile should exhibit four distinct regions which are named, in order of increasing distance from the wall: the sublayer, buffer layer , logarithmic region , and the core. It can be shown from theoretical considerations, (see for example Tennekes and Lumley, 1975) that the sublayer velocity profile must be of the form $\overline{u_1}^* = x_2{}^*$ and that a logarithmic region must exist for which $\overline{u_1}^* = Aln(x_2{}^*) + B$. Hussain and Reynolds (1975) assert that in fully developed channel flow $A = 2.44$ and $B = 5.0$ although there is some scatter in the experimental estimates given for these constants. The mean velocity profile obtained from the DA dataset is presented in Figure 1 along with the profiles from Hussain and Reynolds and KMM. We find that the DA dataset gives good agreement with the experimental result and the higher resolution calculations. The logarithmic layer in the current calculation is not as thick (in viscous units) as in the KMM result. This is a direct consequence of the wall Reynolds number difference (125 for DA and DAG and 180 for KMM) since the wall to the centerline distance in viscous units is equal to the wall Reynolds number itself. It does not appear, however, that the logarithmic layer from the DA dataset is as clearly distinct from the buffer layer as in the experiments or the KMM calculations.

The intensity profiles for the DA dataset are shown in Figure 2. The peak in the intensity of the streamwise component of velocity occurs at a distance of 14.76 for the DA data which is in excellent agreement with KMM and the experiments of Kreplin and Eckelmann(1979) but the peak intensity level is somewhat lower than either KMM or experiment. The DA and the KMM spanwise and wall-normal velocity intensities are both considerably lower than the experimental results. (KMM reference the work of Perry, Lim and Henbest(1985) who maintain that cross-contamination in hot wire measurements may be the cause of the higher wall-normal and spanwise velocity intensities measured by many investigators.) Farther from the wall the DA results show slightly lower intensities than the KMM results. We also note that there is an unusually high value of the wall normal velocity intensity at a distance of 2.4. This is an artifact of the application of a Neumann boundary condition on the pressure in the Orszag-Kells algorithm which has been discussed in Section 2.2.1.b.

The mean velocity profile and turbulence computed from the DAG dataset, which was generated using the Green function method discussed in Section 2.2.1.c, are presented in Figures 3 and 4. The DAG mean velocity profile exhibits a more clearly defined logarithmic layer than the DA profile and there are significant improvements in behavior of the intensities. First, the streamwise velocity intensity has increased and is now very close to both KMM and experiment. Secondly, the artifact produced near the wall in the wall-normal velocity component has now vanished due to the Green function correction which insures enforcement of continuity at the wall. This implies that wall normal derivative of u_2 must vanish at the wall. There is also a marginal increase in the wall-normal velocity intensity and a somewhat larger decrease in the spanwise velocity intensity.

In figure 5 we compare the Reynolds stress computed from the DA data with the KMM data and the experimental data of Eckelmann(1974) who made measurements at R^* values of 142 and 208. The DA results (recall that these calculations were performed at $R^* = 125$) are in reasonable agreement with the Eckelmann ($R^* = 142$) results but are considerably lower than the KMM results ($R^* = 180$) and the higher Reynolds number experimental values. In Figure 6 the DAG results show somewhat better agreement with the lower Reynolds number experimental results. This comparison suggests that for the relatively weak turbulence represented in the DA and the KMM data that some of the discrepancy between these calculations may be due to Reynolds number differences.

From this point on (Figues 7-16) we will make comparisons only to the DAG datasets. In figure 7 the correlation coefficient (Reynolds stress normalized by the relevant root mean square amplitudes) shows the same sharp peak near the wall as in the KMM data although its value is somewhat higher. This is clearly a reflection of the lower turblence intensities in our calculation. We note however that the peak near the wall is absent in the experiments of Sabot and Comte-Belot (1976).

The skewness for each velocity component is plotted in Figures 8,9 and 10. The data generally agree with the KMM results and experimental data of Barlow and Johnston (1985) and Kreplin and Eckelmann (1979). The notable exception is the normal component of velocity where KMM and DAG agree but differ significantly with the experimental data. The flatness for each velocity component is plotted in Figures 11, 12 and 13. The agreement between the DAG and the experimental data is again quite good.

The root mean square vorticity for DAG is plotted Figure 14 and shows excellent agreement with the KMM data and the experiments of Kastrinakis and Eckelmann (1983). The DAG spanwise vorticity shows precisely the same minimum near the wall at about $x_2^* = 5$ as in the KMM result. KMM postulate the existence of wall layer vortical structures to explain this unexpected result. The flatness and skewness for the fluctuating component of vorticity are plotted in Figures 15 and 16 for which there are no comparisons available.

Generally it can be concluded from these comparisons that the mean statistics of the DAG dataset compare well with the highly resolved data of KMM. Our calculations confirm the minimum in the spanwise vorticity as seen in the KMM work. These calculations also confirm, in agreement with KMM, spanwise and wall-normal turbulence intensities that are lower than experimental values.

It is clear that the use of the Green function method improves the one-point statistics computed with the unmodified Orszag-Kells method (i.e. the DA dataset). However, an important issue has been raised by the results presented above. This issue stems from the observation that simulations like those discussed here produce one-point statistics which are remarkably close to those produced by the fully resolved simulations of KMM. It certainly cannot be claimed that if one achieves good one-point statistics that fundemental turbulent dynamics are also being captured. Indeed, conditional sampling performed on the current data (Section 3.3) indicates a bursting rate that is lower than experiment. On the other hand, it is difficult not to conclude that the underlying large scale (or coherent structures), which are being adequately resolved at the resolutions presented here, must be dominating the global behavior of the flow so that the modest resolutions employed here are adequate to achieve good overall results. Certainly this is not a strong argument to justify the use of marginal resolution but it does suggest that expansion functions determined from, for example, a Karhunen-Loeve expansion (Lumley,1970) may be adequate to capture the essential dynamics.

3.2 Two point statistics

Using the DA data set, we have computed the complete two point correlation function for the flow in the following manner. For any given realization of the flow, $\mathbf{u}(\mathbf{x}, t)$, we compute its Fourier coefficients, by:

$$\mathbf{\Phi}(n, m, x_2) = \sum_{l=0}^{N_1-1} \sum_{k=0}^{N_3-1} \mathbf{u}(l, k, x_2) e^{\frac{2\pi n l i}{N_1}} e^{\frac{2\pi m k i}{N_3}}$$

where

$$i = \sqrt{-1},$$

$$n = 0, \ldots. \frac{N_1}{2} + 1,$$

and

$$m = \frac{-N_3}{2}, \ldots. \frac{N_3}{2} - 1. \tag{3.5}$$

In these expressions we have implicitly defined collocation points $(x_1)_l$ and $(x_3)_k$, and wavenumbers $(k_1)_n$ and $(k_3)_m$ as follows:

$$\begin{aligned} (x_1)_l &= l \times L_1/N_1, \\ (x_3)_k &= k \times L_3/N_3, \\ (k_1)_n &= n \times \frac{2\pi}{L_1}, \\ (k_3)_m &= m \times \frac{2\pi}{L_3}, \end{aligned} \tag{3.6}$$

in which L_1 and L_3 are the domain lengths in the streamwise and spanwise directions respectively. In (3.5) time serves merely as a parameter which may be used to identify any given flow realization and is therefore suppressed. We now follow Sirovich(1987) who suggests that the geometric symmetries of a flow should be exploited to increase the effective number of realizations that are used in the averaging process. For the case of channel flow, the equations of motion are invariant with respect to wall normal reflection, spanwise reflection, and rotation about the streamwise axis. These symmetries yield additional spectral representations of the flow which can be written:

$$\begin{aligned}\boldsymbol{\Phi}^1 &= \{\Phi_1{}^0(n,m,-x_2), -\Phi_2{}^0(n,m,-x_2), \Phi_3{}^0(n,m,-x_2)\}\\ \boldsymbol{\Phi}^2 &= \{\Phi_1{}^0(n,-m,x_2), \Phi_2{}^0(n,-m,x_2), -\Phi_3{}^0(n,-m,x_2)\}\\ \boldsymbol{\Phi}^3 &= \{\Phi_1{}^0(n,-m,-x_2), -\Phi_2{}^0(n,-m,-x_2), -\Phi_3{}^0(n,-m,-x_2)\}.\end{aligned} \tag{3.7}$$

In these expressions, the superscripts 1, 2, and 3 refer to vertical reflection, spanwise reflection, and streamwise rotation symmetries respectively and the zero superscript refers to the unaltered (spectral) representation of the flow. The subscripts continue to represent the coordinate directions as previously defined. The (complex) spectrum $\Psi_{\alpha\beta}$ can now be computed from:

$$\Psi_{\alpha\beta}(n,m,x_2,x_2{}') = \langle \frac{1}{4}\sum_{p=0}^{3} \overline{\Phi_\alpha{}^p}(n,m,x_2)\Phi_\beta{}^p(n,m,x_2{}')\rangle \tag{3.8}$$

where,

$$\alpha,\beta = 1,2,3.$$

The overbar designates complex conjugate, and the brackets represents an average over all 30 realizations in the DA dataset. We note that in addition to the increase in the effective size of the data base by a factor of four, the symmetries have the additional advantage of reducing the size of $\Psi_{\alpha\beta}$ also by a factor of four. A factor of two comes from the spanwise symmetry which insures that $\Psi_{\alpha\beta}$ is unique for $n > 0$ and $m > 0$. A second factor of two comes from the vertical reflection symmetry which gives unique values of the spectrum for $-1 < x_2 < 0$ and $-1 < x_2{}' < 1$. The two point correlation function , $R_{\alpha\beta}$, can now be obtained from:

$$R_{\alpha\beta}(l,k,x_2,x_2{}') = K \sum_{n=0}^{\frac{N_1}{2}-1} \sum_{m=-\frac{N_3}{2}}^{\frac{N_3}{2}-1} \Psi_{\alpha\beta}(n,m,x_2,x_2{}') e^{\frac{2\pi nli}{N_1}} e^{\frac{2\pi mki}{N_3}} \tag{3.9}$$

where

resolution remaining unchanged) and also by running at higher absolute grid resolution. We also note, in Figure 18b, a clear example of the errors induced by the Orszag-Kells algorithm near the wall. The curve labeled a, for $x_2{}^* = 0.602$ appears to be completely unrelated to the other curves in Figure 18b. For this distance from the wall the vertical component of velocity undergoes a much too rapid loss of streamwise correlation. This peculiar behavior must be connected to the boundary condition inconsistency problem described in Section 2. It is interesting to note, however, that this error shows up in the correlation function only for the vertical velocity component and then only very near the wall. This does not imply however, that, other errors are produced which are not localized to the wall region. Indeed, as described in Section 3.1, we found some loss of velocity fluctuation intensity in the buffer region. Finally, we note the interesting behavior in the streamwise correlation curves for the spanwise velocity shown in Figure 18c. The clear separation of the curves below $x_2{}^* = 14.76$ and those above $x_2{}^* = 28.3$ is evident which suggests that the spanwise velocity structure is particularly sensitive to the differences between inner and outer layer physics.

In Figure 19 we present the wall normal dependence of the correlation function by plotting $R_{\alpha\beta}(x_2, x_2{}')$. That is we plot $R_{\alpha\beta}$ given by (3.9) with $l = k = 0$. The correlations for the streamwise velocity (Figure 19a) are positive except for a weak negative correlation for $45.7 < x_2{}^* < 77.2$ which appear at values of $x_2{}'$ across the centerline of the channel. Such weakly negative correlations also appear in isotropic turbulence (see Hinze, 1975). The wall normal velocity correlations shown in Figure 19b are positive everywhere with the exception of the wildly oscillating positive and negative behavior for $x_2{}^* = 0.602$. Again, this behavior is attributed to the operator splitting errors discussed previously. In Figure 19d we present the results for R_{12} and note that this function does not peak when $x_2{}' = x_2$ and indeed there is no theoretical reason for the peak to occur there. We note, for example, that close to the wall, say for $0 < x_2{}'^* < 25$, the peaks occur clearly at values of $x_2{}'^*$ for which $x_2{}'^* > x_2{}^*$.

The spanwise velocity correlation function shown in Figure 19c shows the most interesting behavior. We first note that for the curves $0 < x_2{}^* < 21.07$, the correlation is always positive as we move into the wall. The curve for $x_2{}^* = 28.37$ shows the first negative correlation values near the wall. All curves show negative correlation for some values of x_2', when $x_2' > x_2$. One possible interpretation of these correlations is that near the wall there is a streamwise oriented vortex at $x_2^* \approx 20$. That is, we interpret the curve for $x_2^* = 21.07$ as the center of the wall vortex since its correlation coefficient is almost zero but still slightly positive near the wall. This location of the wall vortex center is consistent with the interpretation of the vorticity intensity profiles. The second minima (i.e., the maximum negative values which exist for each curve for $x_2' > x_2$) moves away from the wall roughly in proportion to x_2. That is, the scale of motion seen by observers farther from the wall is proportional to their distance from the wall. We remark, however, that any attempt to interpret these, or any other long-time correlation functions in terms of some proposed flow structures without the addition of flow visualization information is highly speculative. That is, there could be many possible flow structures which could be used to explain any set of correlation functions. The striking features of the R_{33} function, however, do appear to be in agreement with the currently accepted viewpoint that streamwise vortex structures exist near the wall. We also remark that perhaps the most objective way of reconstructing a given three dimensional flow from the complete three dimensional correlation function is by means of more sophisticated statistical approaches such as the orthogonal decomposition proposed by Lumley(1970).

Finally, in Figure 20 we compare our calculations with the measurements of Comte-Bellot(1965). We note first that these measurements were at a Reynolds number of 30,000, a factor of 12 greater than in our calculations. This accounts for the considerably more rapid decay in the measured correlations. We note in particular that the measurements show small negative correlation values for R_{11} for the middle curve of Figure 20a and the two (negative) minima in R_{33}. These characteristics are both in excellent agreement with our calculations.

3.3 Conditional Sampling Results

3.3.1 Purpose

Conditional sampling of a turbulent channel flow is a heuristic search for events or conditions which appear to have some relevance to the kinematics and dynamics of the flow. The search is usually based on some pre-conceived idea or hypothesis which is used as a condition. When the flow is conditionally sampled, the statistics about the occurences of the events can be determined. Some statistics of interest may be the frequency of occurence of the detected events, the ensemble average of the events, or a histogram of some property associated with the detected event.

Conditional sampling has been used by many investigators to detect turbulent bursts. A turbulent burst is an ill-defined event or sequence of events which is responsible for the generation of a disproportionate amount of the Reynolds stress and turbulent kinetic energy. In a single turbulent burst, there may be several ejections of low speed fluid from the wall region into the core. In addition, associated with the turbulent burst is a shear layer which is usually detected as a sweep ($u_2' > 0, u_1' < 0$).

The ensemble average of the conditionally sampled events is considered to be a represention event of the flow physics for a short period of time (say $10t^*$). The rapid fluctuations seen in turbulent flow limit the significance of the ensemble after a short time.

3.3.2 The One And Two Point Detections

There were two objectives to the one and two point detection tests. The first objective was to determine if similar timing statistics and ensemble averages could be obtained from the numerical data set. Two standard detection schemes, the Variable Interval Time Averaging scheme (VITA) and the Second Quadrant Detection scheme (Q_2) were used. They were applied without taking advantage of the spatial character of the data: that is they were used as an experimentalist would have applied them.

The second objective was to determine the proximity of two events in space and time. For example, a particular test was to determine how close two related Q_2 events are in time.

The VITA detection scheme is based on the observation that large fluctuations in the streamwise velocity occur during a typical burst. These large fluctuations are caused by a shear layer passing by the detector. The VITA technique measures the strength and thickness of the shear layer by using a threshold parameter, k, and an averaging time interval, T_a. When the short time variance, properly normalized, exceeds the threshold, k, a burst is detected. An additional condition of the sign of $\frac{\partial u_1}{\partial t}$ is frequently used. Unless noted in this work only positive slope events ($\frac{\partial u_1}{\partial t} > 0$) are retained.

The Reynolds stress can be sorted into the four quadrants in the $u_1' - u_2'$ plane. (See table 3.2) The second quadrant Reynolds stress algorithm, or the Q_2 detection algorithm is based on the observation that to be important, turbulent bursts must develop Reynolds stresses, and second quadrant Reynolds stresses would be the defining property of turbulent ejections. In this detection scheme, an event is considered significant if the magnitude of second quadrant Reynolds stress rises above a predetermined level. Both of these algorithms, along with others, are described in Luchik and Tiedermann (1987).

Table 3.2

Reynolds Stress Quadrant

Quadrant	u'_1	u'_2	Physical Process
Q_1	> 0	> 0	Interaction
Q_2	< 0	> 0	Ejection
Q_3	> 0	< 0	Interaction
Q_4	> 0	< 0	Sweep

Table 3.3
Intra-Burst Ejection Time Scale

U_level	Q_2 threshold,h	Intra-Burst ejection timescale
0.0	0.5	12.3
0.0	1.25	15.2
0.0	2.0	19.9
-0.5	0.5	11.2
-0.5	1.25	13.0
-0.5	2.0	16.0
-1.0	0.5	9.9
-1.0	1.25	11.0
-1.0	2.0	11.9
-1.5	0,5	9.5
-1.5	1.25	10.4
-1.5	2.0	10.6

The timescale discussed above relates two ejection events passing a single detector. Of related interest is the probability of a second event being detected after an initial detection. For example, how likely is the detection of a Q_2 event at a location x_1 and time T_2 given that a detection has occured at a different location x_1 and time T_1. We may also ask how likely is a VITA event to follow or lead a Q_2 event by some time span. With this approach the relationship between differing detection schemes can be studied.

The simulated flow was conditionally sampling at 32 points in the spanwise direction ($\Delta x_3^* = 20$) at two streamwise locations. Then the following probability variable was developed. It is not a normalized probability, but rather a probability relative to a random occurence. Before defining the probability variable, let us introduce the following notation: $T_1(i,n)$ and $T_2(i,n)$ is the detection time of an event i at spanwise location n and streamwise location $x_1(1)$ and $x_1(2)$, respectively, where $x_1(1)$ is the primary location and $x_1(2)$ is the secondary location. Furthermore, introduce a time shift $T_s = T_2 - T_1$. The parameter we want to define is the probability of detecting an event i at the location $T_2(i,n)$ given a detection j at $T_1(j,n)$. This parameter is therefore a function of the two detection schemes applied, the shift in time, T_s, and the shift in the streamwise direction $X_s = x_1(2) - x_1(1)$. We therefore define the probability, p, as follows:

$$p(X_s, T_s) = \frac{1}{N_1}\{\text{ number of events at } T_2(i,n) \text{ given a detection at } T_1(i,n)\},$$

where N_1 is the total number of events detected at streamwise location $x_1(1)$. For large time separations, the events at the two streamwise locations become uncorrelated, and the probability becomes the frequency of the detection of the T_2 events. Therefore, if the probability above is renormalized by the mean detection period of the T_2 events, the resulting probability is a measure of the likelihood that a detection will occur relative to the random detection.

Some of the main results are as follows:

(1) Positive slope VITA events are less dispersive as they convect. When the primary and secondary detectors use VITA and $X_s^* = 240$, two peaks in the relative probability can be seen. The first peak, centered in time about the convective shift $20t^*$, is a result of those events detected at the primary location. A second peak, centered about a convective shift of $-40t^*$ is a result of those events which will be detected at the primary location.

(2) For $X_s^* = 240$, the Q_2 events show a similar two peaked behavior, but the peaks have spread wider than for the VITA events. This implies that the convection speed for the Q_2 events is more varied than for the VITA events.

Table 3.4

Program Flow Chart for Detection and Indexing of Streaks

Input/Output		Routine		Process
Velocity Fields	⟶	Lss.ftn		Finds All Streaks
		↓		
Sorted Streaks	⟵	Resort.Ftn		Sorts Streaks In Time
		↓		
Sorted and Indexed Streaks	⟵	Timing.Ftn		Develops Statistics Deletes Short Streaks

Typical low speed streaks can be seen in Figures 23 and 24. Figure 23 is a plan view of the plane $y^* = 15$. Figure 24 is a view looking upstream at the point $x_1^* = 0$. Both figures are of the streamwise velocity. The shaded regions indicate where the fluctuating velocity is less than $-u'_1$. The markers indicate where the streaks have been detected and followed. There are ten detected streaks at this point in time. Three in the vicinity of $x_1^* = 400$ and $x_3^* = 300$ are weakly defined.

The spacing of the detected streaks is about 100 to 130 viscous lengths apart, which is consistent with experiments. Depending on the parameters used in the Lss.ftn program, the average streak spacing was between 105 and 115 viscous lengths.

We also find (Fig. 24) that the locations detected occur under or near 'tunnel' shaped shear surfaces. Consider the detections at $x_3^* = 90$ and 190, which were typical of smooth, steady, non-meandering low speed streaks. The locations $x_3^* = 340$ and 530 come after the passage of a streak and are weakly defined since the streaks may have lifted away from the wall. Note that inflection velocity profiles can be seen near $x_3^* = 70$, 350 and 520, all of which are near low speed streaks.

Figure 25 shows the evolution of the normal velocity along a low speed streak in the streamwise direction (the horizontal axis) as a function of time (the vertical axis). The convection speed of the velocity perturbations remains about $10u^*$ even though the streamwise velocity in the streak is about $8 - 9u^*$. A typical pair of Q_2 events is located at $t^* = 50$ and $x_3^* = 200$. At $t^* = 20$ and $x^* = 350$ a perturbation in the normal velocity is developing in front of an existing one. This is the development of a new Q_2 event. The existing and the new perturbation may be related to the pair at 50, 200.

Unfortunately, the scheme which finds the initial streaks is not very robust. If a streak develops a kink or dips below the plane in which the searching is done, it may be evaluated as two streaks and the continuity in time is lost. Experimentally, the effects of low speed streaks can be seen for a few thousand viscous time units, but when using the algorithms developed on the data available, less that 3% of the detected streaks lasted more than $200t^*$. Better results are expected when the algorithm is applied closer to the wall, where the flow is more stable.

4. Conclusions

We have investigated, in some detail, the statistical properties of turbulent flow in a channel using data generated from moderate resolution direct numerical simulations. Both long-time averages and conditional averages were computed. We have concluded that the use of the Green function method results in turbulence statistics which are significantly closer to experiments than those produced with the Orszag-Kells algorithm (Section 3.1). However, the velocity fluctuation intensities are still somewhat lower than those produced by the fully resolved KMM calculation. This is particularly true for the wall-normal and spanwise velocities. However, the vorticity profiles are in excellent agreement with the KMM results. For the two-point statistics presented in Section 3.2 we find that the spanwise correlation lengths are in excellent agreement with the KMM results when Reynolds number differences are taken into account. The streamwise correlation lengths, particularly those of the streamwise velocity component, are somewhat larger than the KMM result. We speculate that Reynolds number differences, box length differences, and resolution may all be contributing to these discrepancies. The wall-normal dependence of the spanwise velocity correlation function, $R_{33}(x_2, x_2')$, shows behavior which is suggestive of near wall steamwise vortical structures. The wall-normal dependence of each correlation function shows excellent qualitative agreement with the measurements of Comte-Bellot.

The three conclusions to the conditional sampling work are: (1) the low speed streak tracing is able to follow in space and time the low speed streaks, but the method needs to be applied closer to the wall; (2) to determine temporal statistics, a dataset with a longer domain is needed, and; (3) the results from the two point conditional sampling scheme indicate that there is a very definite correlation between VITA and Q_2 events and that the model proposed in Leighton (1986) is at least partially correct. Further developments in conditional sampling will require an improved dataset and will be finished in the near future.

We have found that aliasing errors have significant effects on the final steady-state solutions to the Navier-Stokes equations for channel flow (Appendix A). When the calculation has converged to the predicted steady-state value of the wall shear stress and aliasing errors are not eliminated, we find that both the mean velocity and the centerline velocity converge to values which are significantly lower than experimental values. In addition, the velocity fluctuation intensities, particularly that of the streamwise velocity component, are too low in amplitude and peak at distances too far from the wall. We conclude that aliasing errors produce solutions which appear stable but which are very much like the flow of underdeveloped turbulence. Aliasing errors appear to have a damping effect on the turbulence. The strength of these effects may well be due to the low resolution of these calculations, but what appears to us to be most interesting is that when these errors are removed, the solution goes quickly back to that of experimentally observed turbulence.

Acknowledgements

This work was supported by the Fluid Dynamics 6.1 Task Area of the Naval Research Laboratory. The authors also gratefully acknowledge the support and assistance of John McLaughlin (Clarkson University), Steven Lyons and Thomas Hanratty (University of Illinois), and Lawrence Sirovich and Kenneth Ball (Brown University). We also thank Steven Orszag and Raj Panda (Princeton University) for permission to use Figure A3.

Appendix

A. Effects of Aliasing Errors on the Behavior of Channel Flow Turbulence Calculations

1. Introduction

It has been known for some time that aliasing errors can have unwanted effects on spectral calculations. In fact, in low resolution calculations, aliasing errors can lead to catastrophic numerical instabilities. Before discussing the details of the effects of aliasing in turbulent channel flow calculations, however, we first give a brief review of the mathematical origin of aliasing errors. We first begin with a simple example of aliasing effects arising in the representation of a continuous one-dimensional function. We assume that we are given a continuous function which is represented by an infinite (convergent) Fourier series. That is, $u(x)$ is given by:

$$u(x) = \sum_{k=-\infty}^{\infty} \hat{u}_k e^{ikx} \tag{A1}$$

where

$$\hat{u}_k = \frac{1}{2\pi}\int_0^{2\pi} u(x)e^{-ikx}dx.$$

Now, we suppose that we sample the continuous function at the discrete points, $x_j = \frac{2\pi j}{N}, j = 0....N-1$. It follows that:

$$u(x_j) = \sum_{k=-N/2}^{N/2-1} u_k^* e^{ikx_j} \tag{A2}$$

and,

$$u_k^* = \frac{1}{N}\sum_{j=0}^{N-1} u(x_j)e^{-ikx_j}. \tag{A3}$$

That is, we clearly distinguish the continuous Fourier modes from the discrete modes. To find the relationship between these two sets of modes we write:

$$u_p^* = \frac{1}{N}\sum_{j=0}^{N-1}\sum_{k=-\infty}^{\infty} \hat{u}_k e^{ikx^j} e^{-ipx_j}, \tag{A4}$$

or

$$u_p^* = \sum_{k=-\infty}^{\infty} \hat{u}_k \frac{1}{N}\sum_{j=0}^{N-1} e^{i(k-p)x_j},$$

where

$$\frac{1}{N}\sum_{j=0}^{N-1} e^{i(k-p)x_j} = \begin{cases} 1, & \text{if } k-p=mN \quad m=0,\pm 1,\dots; \\ 0 & \text{otherwise.} \end{cases} \tag{A5}$$

Therefore, we find the following relationship between the discrete and continuous modes:

$$u_p^* = \hat{u}_p + \sum_{\substack{m=-\infty \\ m\neq 0}}^{\infty} \hat{u}_{p+mN}. \tag{A6}$$

The second term on the right represents the aliasing errors which contaminate the discrete Fourier representation of $u(x)$. We note that if there is no energy in $u(x)$ beyond mode N then these errors vanish and the discrete coefficients equal the continuous coefficients.

In Navier-Stokes calculations, aliasing errors arise from the non-linear terms in the equations of motion. For example, the term $\mathbf{u} \times \omega$ gives rise to errors when the rotational form of the equations are used. In pseudo-spectral calculations we perform the nonlinear product of velocity and vorticity in physical space as opposed to computing the convolution sums which would arise if a purely Galerkin procedure were used. This procedure of performing the non-linear calculation in physical space has been shown by Orszag(1971b) to be considerably more efficient then the Galerkin approach but then aliasing errors may contaminate the calculation. A simple example will clarify the mathematical origin of aliasing due to nonlinearities. We are given the discrete representation of two functions $u(x)$ and $v(x)$ as follows:

$$u(x_j) = \sum_{k=-N/2}^{N/2-1} u_k^* e^{ikx_j}, \qquad (A7)$$

and

$$v(x_j) = \sum_{p=-N/2}^{N/2-1} v_p^* e^{ipx_j}, \qquad (A8)$$

where

$$x_j = \frac{2\pi}{N} j$$

$$j = 0, 1, ...N - 1.$$

The product of these functions is then given by:

$$z_j = \sum_k \sum_p u_k{}^* v_p{}^* e^{i(k+p)x_j}, \qquad (A9)$$

where

$$z_j = u(x_j)v(x_j)$$

and the Fourier coefficients of z_j are:

$$z_q^* = \sum_k \sum_p u_k{}^* v_p{}^* \frac{1}{N} \sum_{j=0}^{N-1} e^{(k+p-q)x_j}. \qquad (A10)$$

Now we use, again, the identity:

$$\frac{1}{N}\sum_{j=0}^{N-1} e^{i(k+p-q)x_j} = \begin{cases} 1, & \text{if } k+p-q = mN \quad m = 0, \pm 1, \ldots; \\ 0 & \text{otherwise.} \end{cases} , \qquad (A11)$$

(A10) becomes:

$$z_q^* = \sum_{\substack{(k,p) \\ k+p=q}} u_k{}^* v_p{}^* + \sum_{\substack{m=-\infty \\ m\neq 0}}^{\infty} \sum_{\substack{(k,p) \\ k+p-q=mN}} u_k{}^* v_p{}^*. \qquad (A12)$$

However, we note the following inequalities;

$$| p |, | k |, | q | \leq \frac{N}{2}, \qquad (A13)$$

and

$$\max(p + k - q) = \frac{3N}{2}.$$

Since $\frac{3N}{2} < 2N$ it therefore follows that $| m | \leq 1$. The final result becomes:

$$z_q^* = \sum_{\substack{(k,p) \\ k+p=q}} u_k{}^* v_p{}^* + \sum_{\substack{(k,p) \\ k+p=q+N}} u_k{}^* v_p{}^* + \sum_{\substack{(k,p) \\ k+p=q-N}} u_k{}^* v_p{}^*. \qquad (A14)$$

The last two terms on the right hand side of (A14) are termed aliasing errors. We observe that if all modes $\frac{N}{2} > (k,p) > \frac{N}{3}$, and$\frac{-N}{3} > (k,p) > \frac{-N}{2}$ are removed from the spectral representation of u and v and if their product is taken in physical space, then there can be no aliasing errors in the region $\frac{N}{2} > q > \frac{N}{3}$, and$\frac{-N}{3} > q > \frac{-N}{2}$. This fact was first observed by Orszag (1971a). We note that this so called 'two-thirds rule' works because, for example, when $k + q \geq \frac{-N}{3}$ aliasing errors are dumped into the region $\frac{-N}{3} > q > \frac{-N}{2}$. Since this region of the spectrum is nulled after the non-linear product is taken, the calculation is alias-free. We note that to insure an alias-free calculation one-third of the modes is the minimum number that need to be removed and is therefore an optimal choice. In a typical three dimensional calculation the dealiasing is traditionally performed only in the periodic plane and therefore in our calculations dealiasing is performed using the "2/3 rule" in the $x_1 - x_3$ plane. There is some evidence, however, that in the non-homogeneous direction, (x_2) that aliasing effects may be important (Zang and Krist(1987)).

2. Results from low Resolution Aliased Channel Flow calculations

A relatively long run was made using the Orszag-Kells algorithm with the boundary condition, $u_2 = 0$ on $x_2 = \pm 1$, applied in the pressure step in which aliasing errors were not removed. We used $33 \times 64 \times 16$ grid points in the x_2, x_3, and x_1 directions respectively. The calculation was started with laminar initial conditions to which 2D and 3D finite amplitude Orr-Sommerfeld modes were applied.

Before proceeding with a detailed description of the results, however, we review the manner in which the flow is driven to a steady-state. This is discussed in Handler, Leighton, and Carroll(1987) but is reiterated here for the sake of completeness. First, we note that in a physical experiment the flow is driven by a pressure gradient. In the simulation, however, periodic boundary conditions are used in the streamwise direction so that *a differential pressure forcing cannot be prescribed.* Thus, an external driving force, $\mathbf{f}$, is required in the equations of motion. We note, of course, that $\mathbf{f}$ is a completely arbitrary function of space and time. If we define a control surface to be that which encloses the entire computational domain, a momentum balance in the streamwise direction gives:

$$\frac{\partial}{\partial t}\int_{-1}^{1} < u_1(\mathbf{x},t) > dx_2 = \frac{-2 < \tau_w >}{\rho U^2} + \frac{2 < f_1(\mathbf{x},t) > L_2}{\rho U^2}. \qquad (A15)$$

In this expression, <>, represents averaging over a horizontal plane, τ_w is the instantaneous shear stress at the wall, and f_1 is the streamwise component of the force per unit volume. The simple form of this expression is due to the use of periodic boundary conditions which insures no net mass flow through the control surface and no net forcing arising from normal stresses. It follows that for a globally steady flow the time rate of change of momentum within the control volume must be zero, so that:

$$\lim_{t\to\infty} < \tau_w > = L_2 \lim_{t\to\infty} < f_1(\mathbf{x}, t) > . \tag{A16}$$

This can be written in non-dimensional form as:

$$\lim_{t\to\infty} R^*(t) = \overline{\lim_{t\to\infty} \frac{< f_1 > L_2}{\rho U^2} R^2}. \tag{A17}$$

Thus, if the arbitrary force reaches a limit as $t \to \infty$, we can predict the final wall Reynolds number.

Some global results of this aliased calculation are presented in Figures A1(a, b, c). In this calculation, the force, $\frac{f_1 L_2}{\rho U^2}$, was fixed at $\frac{4}{R}$ and $R = 4000$, so that we can predict from (A17) that the final Reynolds umber, R^*, will be $\sqrt{4R} = 126.49$. We observe in Figure A1(a) that R^* initially increases rapidly as in the calculation of Orszag and Patera (1983) but then, after the flow has gone through transition to turbulence, the wall Reynolds number gradually decays to the predicted value. Some oscillations about the predicted value of 126.49 occur but a dynamic equilibrium, that is a state in which the driving force is balanced by shear stresses at the wall, has been achieved. We can now use the correlations introduced by Dean(1978) for fully developed channel flow to determine values for R_{cl} and R_m, the Reynolds number based on centerline velocity, U_{cl}, and that based on the average, or bulk, velocity U_m. We perform this calculation by using the value $R^* = 126.49$. The relationships:

$$\frac{\tau_w}{\frac{1}{2}\rho {U_m}^2} = 0.073 {R_m}^{-.25} \tag{A18}$$

$$\frac{\tau_w}{\rho} = u^{*2} \qquad (A19)$$

and

$$u^* = \frac{R^*}{R} \qquad (A20)$$

can be used to predict R_m, and the relation

$$\frac{U_c}{U_m} = 1.28 {R_m}^{-0.0116} \qquad (A21)$$

is used to predict the centerline velocity which can then be used to compute R_{cl}. The results of this calculation give $R_m = 3697.5$ and $R_{cl} = 2151.3$. From Figures A1(b) and A1(c) we find that, at the end of the calculation, $R_m = 4470$ and $R_{cl} = 2800$. Thus, we find that both the mean Reynolds number and centerline Reynolds number are significantly higher then they would be in an experiment *with this asymptotic value of the wall shear stress.* The effect of aliasing has been to give a larger mass flux for the given pressure gradient (driving force) than for fully developed turbulence. This gives a strong indication that the flow is not a fully developed turbulence. Evidence for this is given in Figures 3(a, b) in which we have performed a somewhat different calculation. Here we have used a fully converged solution which we obtained from Steven Lyons at the Univ. of Illinois from an alias-free code as an initial condition to our (aliased) code. We note that the effect of aliasing was first (Figure A2(a)) to increase the centerline velocity and cause a dramatic loss of the logarithmic region of the mean velocity profile that was clearly present in the initial condition. The final velocity profile is very similar to that obtained by Patel and Head (1969) in transitional (underdeveloped) turbulent channel flow. We also observe in Figure A2(b) that the intensity of the streamwise velocity fluctuations are dramatically reduced and the location of the maximum intensity has shifted farther from the wall.

We also report on an independent test of the effects of aliasing performed by Panda (1987) who performed low resolution channel flow calculations in which the dealiasing algorithm was turned on at an appropriate time in the calculation. These results are shown in Figures A3(a) and A3(b). We note that the effect of dealiasing was to cause a dramatic decrease in the centerline velocity which is consistent with our results. There can be little doubt from these results that aliasing errors, at least for these low resolution calculations, has a damping effect on the turbulence. We observe first that the effect is not clearly exhibited unless the calculations are run for very long times, so that these errors have a chance to build and interfere in some way with the proper solution to the equations. Secondly, and perhaps most importantly, the aliasing errors caused no catastrophic numerical instabilities. Instead, the effects were subtle in the sense that earlier in the calculations (results not shown here) the mean velocity profile did exhibit a logarithmic layer which subsequently disappeared. In conclusion, aliasing errors affect, in a significant manner, the long-time behavior of the turbulent solution to the equations of motion. We speculate that aliasing errors are acting very much like an external forcing which has both the proper phase and amplitude to cause some damping, but not a complete destruction of the turbulence.

B. Calculation of Energies from Fourier Spectra

When Fourier spectra are computed, as in (3.8), it is useful to check the results by computing from them the mean square values, or energies, by integrating the spectra over all wavenumbers. This result can then be compared with a 'direct' calculation of the energy by squaring and averaging the physical variable of interest such as velocity or pressure, for example, in its physical (space-time) representation. We derive here a convenient expression for a real function of two (space) variables that can be used to make such a check. We first define the real function $u(x, y)$ and its Fourier coefficients $a_{k,p}$ as follows:

$$u_{l,m} = \sum_{k=-N/2}^{N/2-1} \sum_{p=-N/2}^{N/2-1} a_{k,p} e^{ikx_l} e^{ipy_m}, \qquad (B1)$$

and,

$$a_{k,p} = \frac{1}{N^2} \sum_{l=0}^{N-1} \sum_{m=0}^{N-1} u_{l,m} e^{-ikx_l} e^{-ipy_m}. \qquad (B2)$$

The physical lengths are defined by $x_l = \frac{2\pi}{N} l$ and $y_m = \frac{2\pi}{N} m$. The mean square energy, $\overline{u^2}$, is given by :

$$\overline{u^2} = \frac{1}{N^2} \sum_{l=0}^{N-1} \sum_{m=0}^{N-1} {u_{l,m}}^2. \qquad (B3)$$

It follows from (B1) that:

$$\overline{u^2} = \sum_{k,p} \sum_{k',p'} a_{k,p} a_{k',p'} \frac{1}{N^2} \sum_{l=0}^{N-1} \sum_{m=0}^{N-1} e^{i(k+k')x_l} e^{i(p+p')y_m}. \qquad (B4)$$

Use of the identities:

$$\frac{1}{N} \sum_{m=0}^{N-1} e^{i(p+p')y_m} = \begin{cases} 1, & \text{if } p + p' = nN \quad n = 0, \pm 1, \ldots; \\ 0 & \text{otherwise.} \end{cases} \qquad (B5)$$

and

$$\frac{1}{N}\sum_{l=0}^{N-1} e^{i(k+k')x_l} = \begin{cases} 1, & \text{if } k+k' = nN \quad n = 0, \pm 1, \ldots; \\ 0 & \text{otherwise.} \end{cases} \tag{B6}$$

and the use of the reality of u, that is $a_{kp} = \overline{a_{-k,-p}}$, leads to the following expression for the energy:

$$\overline{u^2} = a_{0,0}^2 + a_{-N/2,0}^2 + a_{0,-N/2}^2 + a_{-N/2,-N/2}^2 +$$

$$2\{\sum_{k=1}^{N/2-1}\sum_{p=-N/2+1}^{N/2-1} |a_{kp}|^2 + \sum_{p=1}^{N/2-1} |a_{0,p}|^2$$

$$+ \sum_{p=1}^{N/2-1} |a_{-N/2,p}|^2 + \sum_{k=1}^{N/2-1} |a_{k,-N/2}|^2\}. \tag{B7}$$

As discussed in Section 3.b, it is sometimes useful to impose the symmetry condition $a_{k,p} = a_{k,-p}$. If this is done the energy becomes:

$$\overline{u^2} = a_{0,0}^2 + a_{-N/2,0}^2 + a_{0,-N/2}^2 + a_{-N/2,-N/2}^2 +$$

$$4\sum_{k=1}^{N/2-1}\sum_{p=1}^{N/2-1} |a_{kp}|^2$$

$$+2\{\sum_{k=1}^{N/2-1} |a_{k,0}|^2 + \sum_{p=1}^{N/2-1} |a_{0,p}|^2\}$$

$$+2\{\sum_{p=1}^{N/2-1} |a_{-N/2,p}|^2 + \sum_{k=1}^{N/2-1} |a_{k,-N/2}|^2\}. \tag{B8}$$

If we define the Fourier coefficients as follows:

$$a_{0,0} = 2A_{0,0} \quad a_{-N/2,0} = 2A_{-N/2,0}$$

$$a_{0,-N/2} = 2A_{0,-N/2} \quad a_{-N/2,-N/2} = 2A_{-N/2,-N/2}$$

$$a_{k,0} = \sqrt{2}A_{k,0} \quad a_{0,p} = \sqrt{2}A_{0,p}$$

$$a_{-N/2,p} = \sqrt{2}A_{-N/2,p} \quad a_{k,-N/2} = \sqrt{2}A_{k,-N/2} \tag{B9}$$

and,

$$\begin{gathered} a_{k,p} = A_{k,p} \\ 1 \leq k \leq N/2 - 1 \\ 1 \leq p \leq N/2 - 1, \end{gathered} \tag{B10}$$

then the energy can be conveniently expressed as :

$$\overline{u^2} = 4\sum_{k=0}^{N/2}\sum_{p=0}^{N/2} |A_{k,p}|^2. \tag{B11}$$

(B11) was used to compute the mean square energies from the spectra, $\psi_{\alpha\beta}$. The results for the root mean square values for the streamwise, spanwise, and wall-normal turbulence intensities are shown in Figure B1 and for the Reynolds stress ,$\overline{u_1 u_2}$, in Figure B2. One can see that these results are identical to the results obtained by performing the 'direct' computation described in section 3.1 and shown in Figures 2 and 5. We conclude with a high degree of confidence that our calculaton of $\psi_{\alpha\beta}$ is correct.

References

Barlow, R.S. & Johnston, J.P. 1985 Structure of turbulent boundary layers on a concave surface. *Rep. MD-47* Department of Mechanical Engineering, Stanford University, Stanford, California, USA.

Bogard, D.C. & Tiedermann, W. G. 1986 Burst detection with single-point velocity measurements. *J. Fluid Mech.* **162**, 389.

Canuto,T., Hussaini, M.Y., Quarteroni, A., Zang, T. A., 1987 *Spectral Methods in Fluid Mechanics*, Springer-Verlag.

Comte-Bellot, G. 1965 *Ecoulement Turbulent entre deux parois parallels.* Publications Scientific et Techniques du Ministere de l'Air.

Dean, R.B. 1978 Reynolds number dependence of skin friction and other bulk flow variables in two-dimensional rectangular duct flow. *Trans. ASME I: J. Fluids Engng.* **100**, 215.

Eckelmann, H. 1974 The structure of the viscous sublayer and the adjacent wall region in a turbulent channel flow. *J. Fluid Mech.* **65**, 439.

Fornberg, B. 1975 On a Fourier method for the integration of hyperbolic equations. *SIAM J. Numer. Anal.* **12**, 509.

Gottlieb, D. & Orszag, S. A. 1977 *Numerical Analysis of Spectral Methods: Theory and Applications*, SIAM-CBMS, 127.

Gottlieb, D., Hussaini, M. Y. & Orszag, S. A. 1984 Theory and applications of spectral methods, in: R.G. Voigt, D. Gottlieb, & M. Y. Hussaini (editors), *Spectral Methods for Partial Differential Equations*, SIAM-CBMS, 1.

Haidvogel, D. B. & Zang, T. A. 1979 The accurate solution of Poisson's equation by expansion in Chebyshev polynomials. *J. Comp. Phys.* **30**, 167.

Handler, R.A., Leighton, R.I., Carroll, D.M. 1987 *NRL Memorandum Report*6009.

Hinze, J. 1975 *Turbulence*, McGraw-Hill.

Hussain, A.K.M.F. & Reynolds, W.C. 1975 Measurements in fully developed turbulent channel flow. *Trans. ASME I: J.Fluids Engng.* **97**, 568.

Kastrinakis, E. G. & Eckelmann, H. 1983 Measurement of streamwise vorticity fluctuations in a turbulent channel flow. *J. Fluid Mech.* **137**, 165.

Kim, J. Moin, P. and Moser, R. 1987 Turbulence statistics in fully developed channel flow at low Reynolds number. *J. Fluid Mech.* **177**, 133.

Krist, S.E., Zang, T.A. 1987 Numerical Simulation of Channel Flow Transition. *NASA Tech. Paper* 2667.

Kreplin, H. & Eckelmann, H. 1979 Behavior of the three fluctuation velocity components in the wall region of a turbulent channel flow. *Phys. Fluids* **22**, 1233.

Leighton, R.I. 1986 Ph.D. Thesis, University of Michigan.

Luchik, T. S. & Tiedermann, W. G. 1987 Burst detection with single-point velocity measurements. *J. Fluid Mech.* **174**, 529.

Lumley, J.L. 1970 *Stochastic Tools in Turbulence*, Academic Press.

Marcus, P.S. 1984 Simulation of Taylor-Couette flow. Part 1. Numerical methods and comparison with experiment. *J.Fluid Mech.* **146**, 45.

Moin, P. Kim, J. 1982 Numerical investigation of turbulent channel flow. *J. Fluid Mech.* **118**, 341.

Moriuti, K. 1987 Comparison of conservative and rotational forms in large eddy simulation of turbulent channel flow. *J. Comp. Phys.* **71**, 343.

Orszag, S.A. 1971a On the elimination of aliasing in finite-difference schemes by filtering high wavenumber components. *J. Atmosph. Sci.* **28**, 1074.

Orszag, S.A. 1971b Numerical simulation of incompressible flows within simple boundaries: I. Galerkin (spectral) representations. *Stud. Appl. Math.* **50**, 293.

Orszag, S.A. & Patterson, G.S. 1972 Numerical Simulation of three-dimensional homogenous isotropic turbulence. *Phys. Rev. Letters* **28**. 76.

Orszag, S.A. & Kells, L.C. 1980 Transition to turbulence in plane Poiseuille and plane Couette flow. *J. Fluid Mech.* **96**, 159.

Orszag. S.A.,Patera, A.T. 1980 Subcritical transition to turbulence in plane channel flow. *Phys. Rev. Lett.* **45**, 989.

Orszag, S. A. & Patera, A.T. 1981 Subcritical transition to turbulence in planar shear flows. in: R.E. Meyer (editor). *Transition and Turbulence*.Academic Press. 127.

Orszag, S. A., Israeli, M. & Deville, M.O. 1986 Boundary conditions for incompressible flows. *J. Sci. Comp.***1** ,75.

Panda, R. 1987 Ph.D. Thesis, Princeton Unveristy.

Patel, V.C. & Head, M.R. 1969 Some observations on skin friction and velocity profiles in fully developed pipe and channel flows. *J. Fluid Mech.* **38**, 181.

Perry, A.E., Lim, K. L. & Henbest, S.M. 1985 A spectral analysis of smooth flat-plate boundary layers. *Proc. 5th Symp. on Turbulent Shear Flows, 7-9 August 1985, Cornell University, Ithaca, NY* , pp 9.29-9.34.

Sabot, J. & Comete-Bellot, G. 1976 Intermittency of coherent structures in the core region of fully developed turbulent pipe flow. *J. Fluid Mech.* **74**, 767.

Schumann, U. 1985 Algorithms for direct numerical solution of Shear-Periodic turbulence. in: J.B. Soubbarameyer(editor) *Proc. 9th Int. Conf. Numerical Methods in Fluid Mechanics* Springer, 492.

Sirovich, L. 1987b Turbulence and the dynamics of coherent structures. *Q. Appl. Math.* **45**, 573.

Smith, C.R. & Metzler, S. P. 1983 The characterization of low-speed streaks in the near wall region of a turbulent boundary layer. *J. Fluid Mech.* **129**, 27.

Tennekes, H. & Lumley, J. L. 1975 *A First Course in Turbulence,* MIT Press .

Zang, T. 1988 On the rotation and skew-symmetric forms for incompressible flow simulations. to appear in: *Applied Numerical Mathematics.*

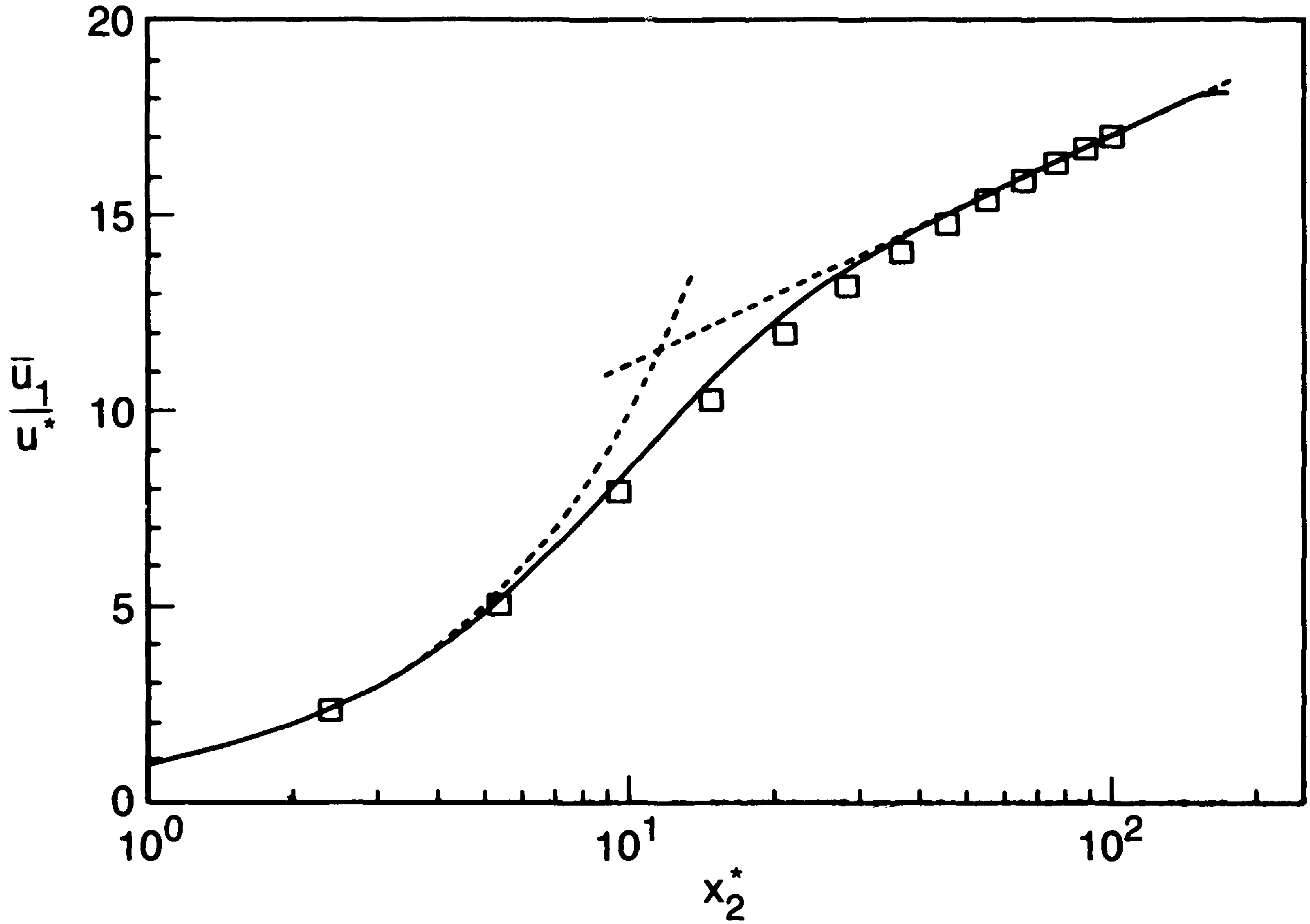

Fig. 1 — Mean Velocity Profiles from the DA dataset. □, Current results. —, KMM, ----, Hussain and Reynolds (1975).

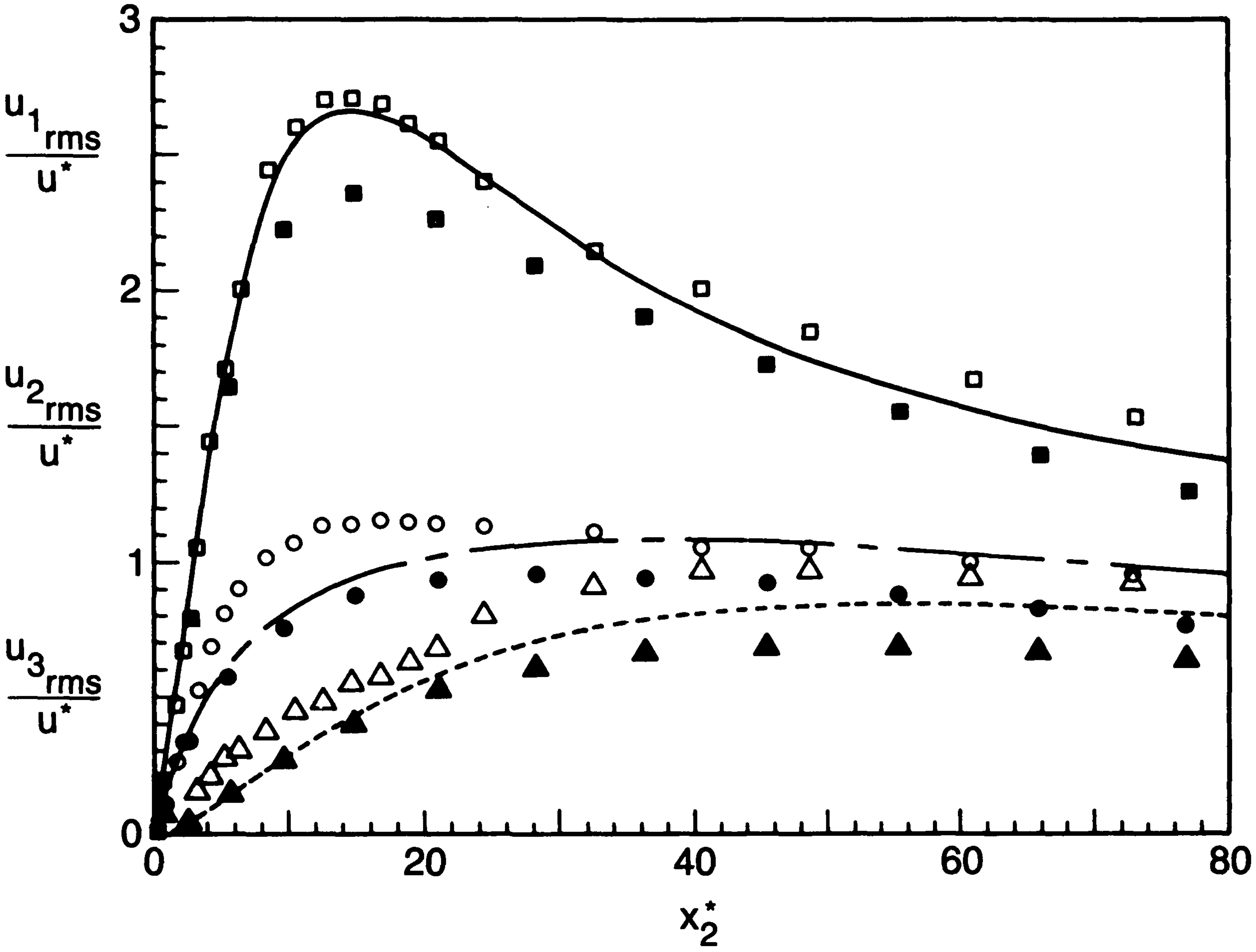

Fig. 2 — Velocity Fluctuation Profiles from the DA dataset. □, u_1, (solid triangle), u_2, ●, u_3, Current results; —, u_1, ----, u_2, — - —, u_3, KMM; □, u_1, Δ, u_2, o, u_3, Kreplin and Eckelmann (1979).

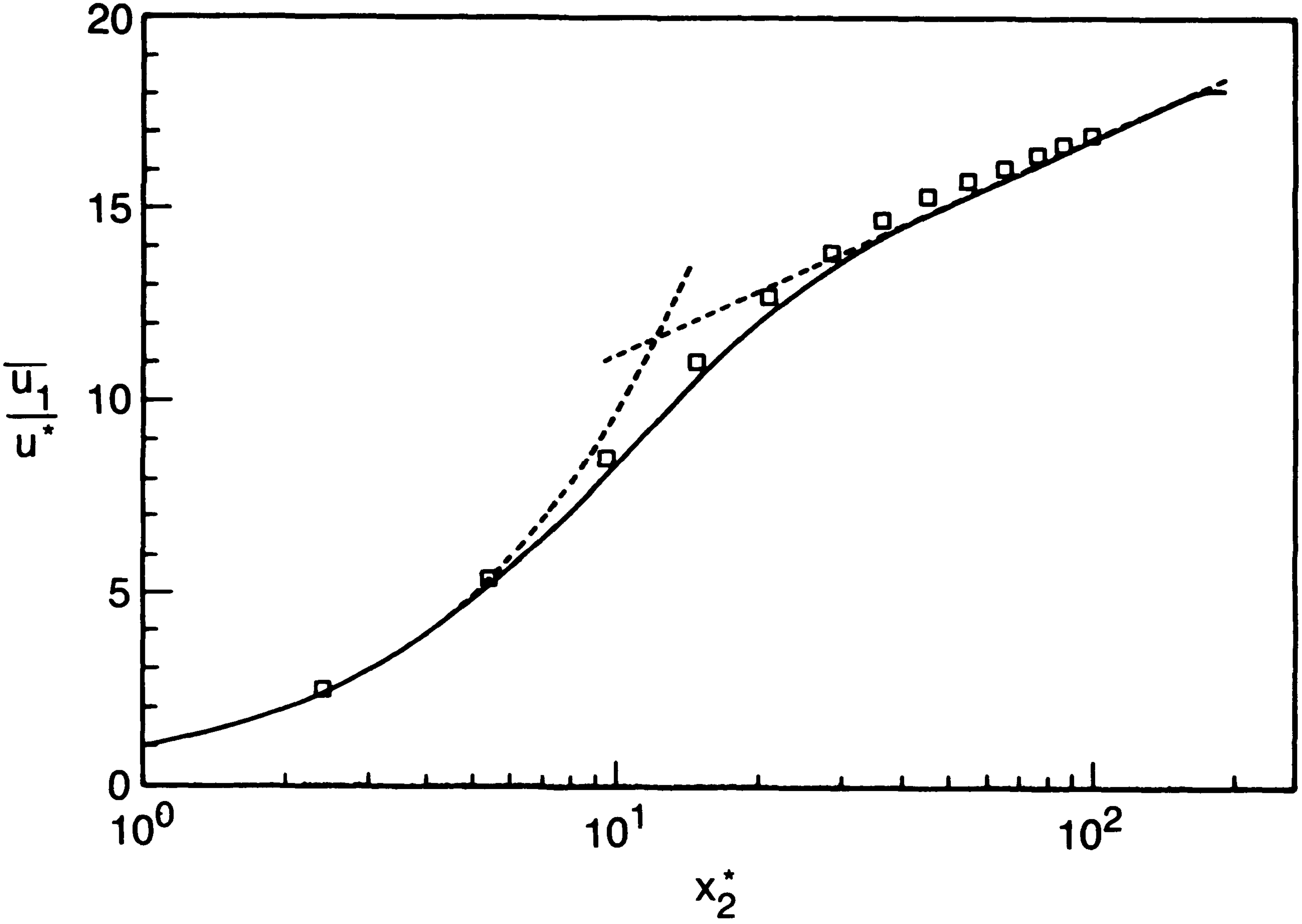

Fig. 3 — Mean Velocity Profiles from the DAG dataset. □, Current results, ——, KMM, ----, Hussain and Reynolds (1975).

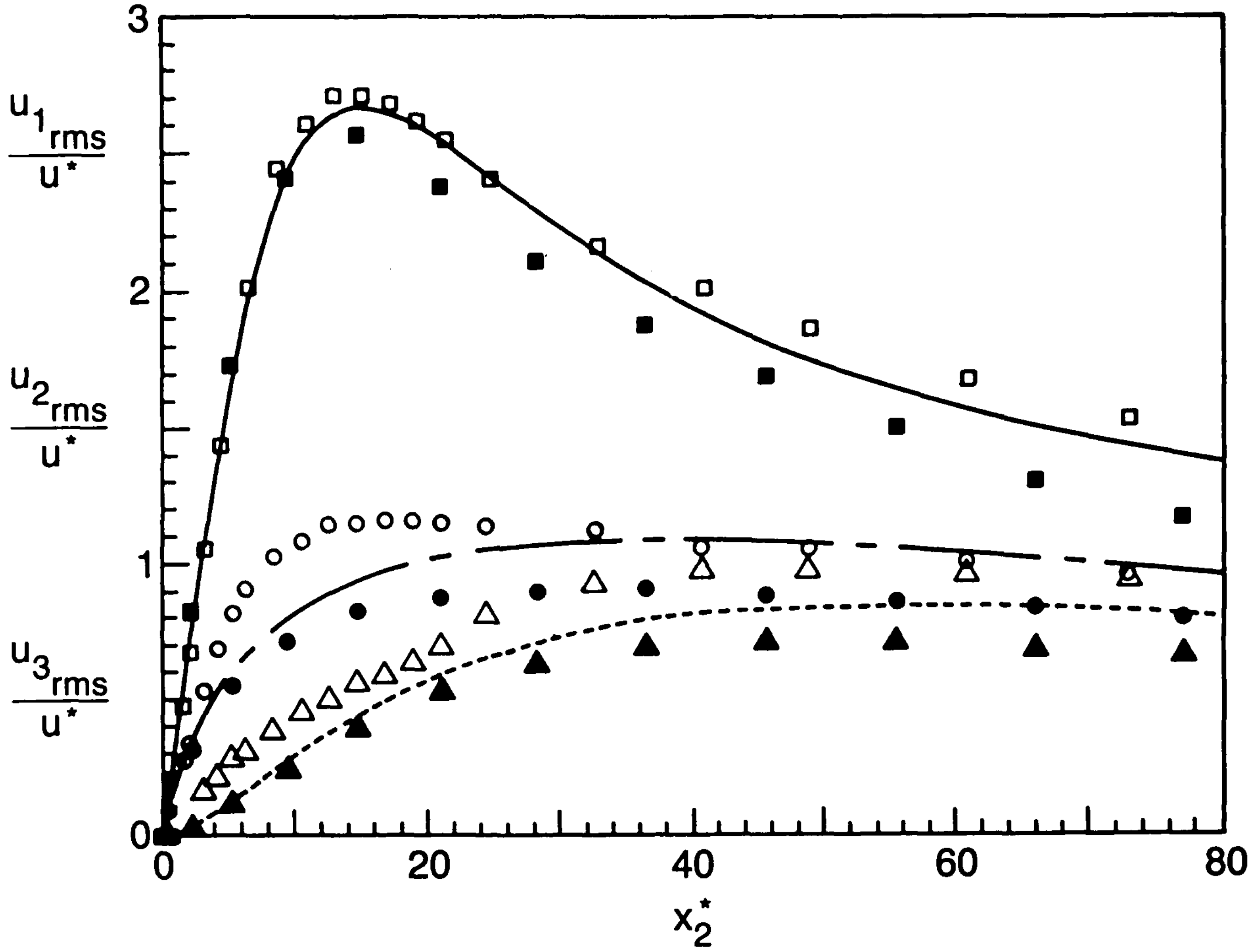

Fig. 4 — Fluctuating Velocity Profiles from the DAG dataset. □, u_1, (solid triangle), u_2, ●, u_3, Current results; —, u_1, ----, u_2, — - —, u_3, KMM; □, u_1, Δ, u_2, o, u_3, Kreplin and Eckelmann (1979).

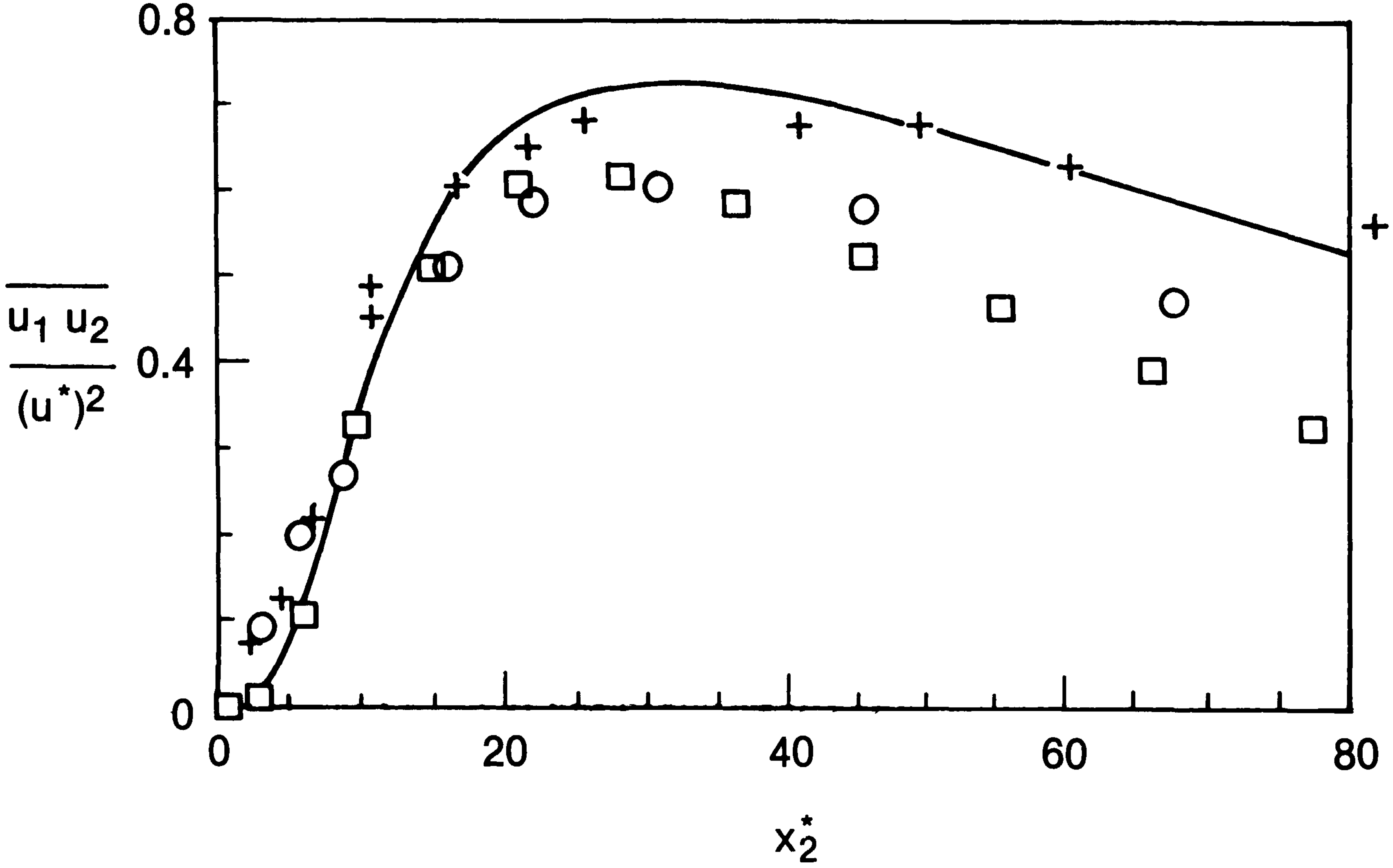

Fig. 5 — $u_1 - u_2$ correlations from the DA dataset. □, Current results; —, KMM; +, $R^* = 208$, ○, $R^* = 142$, Eckelmann (1974).

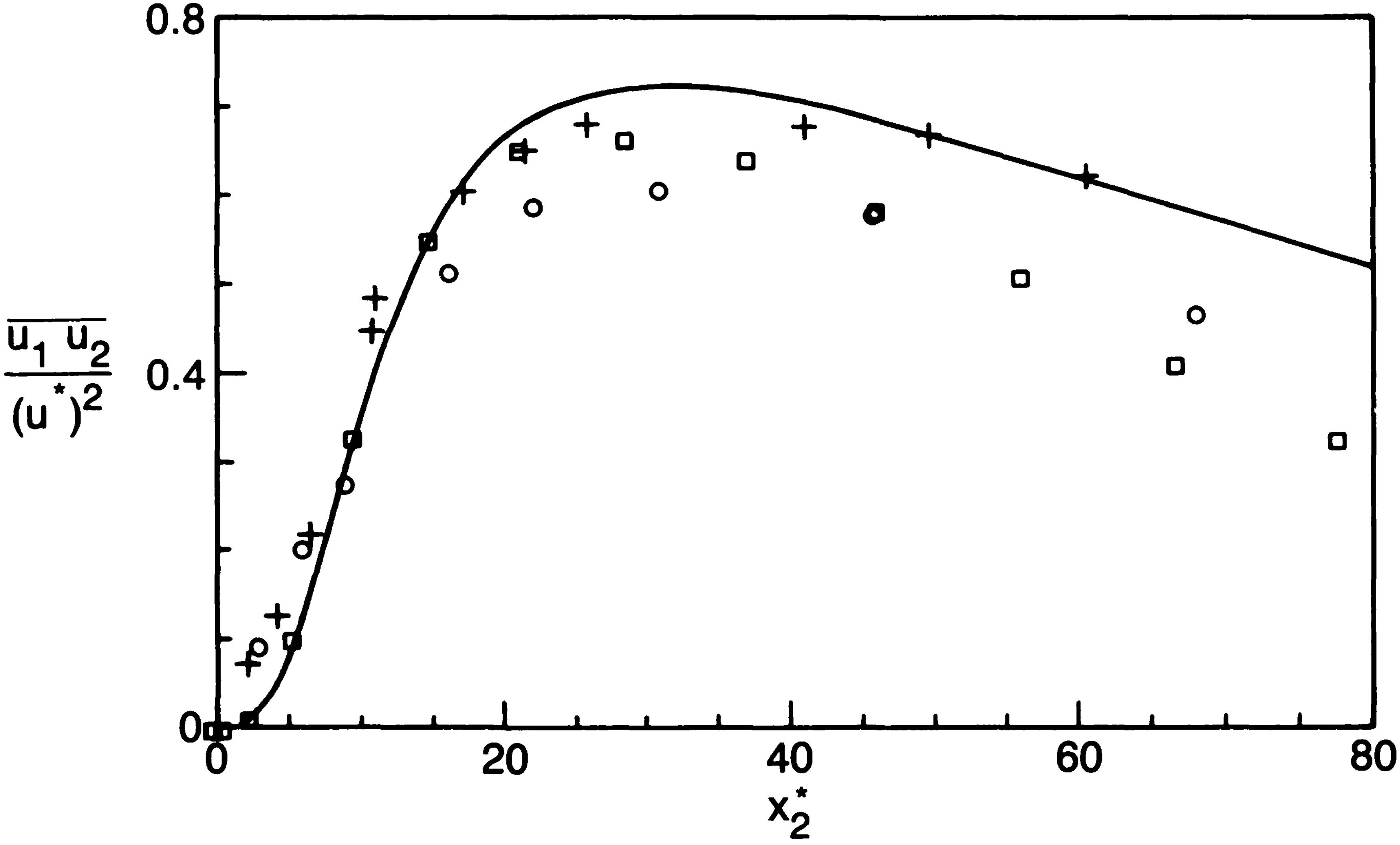

Fig. 6 — u_1–u_2 correlations from the DAG dataset. □, Current results; — KMM; +, R^* = 208, ○, R^* = 142, Eckelmann (1974).

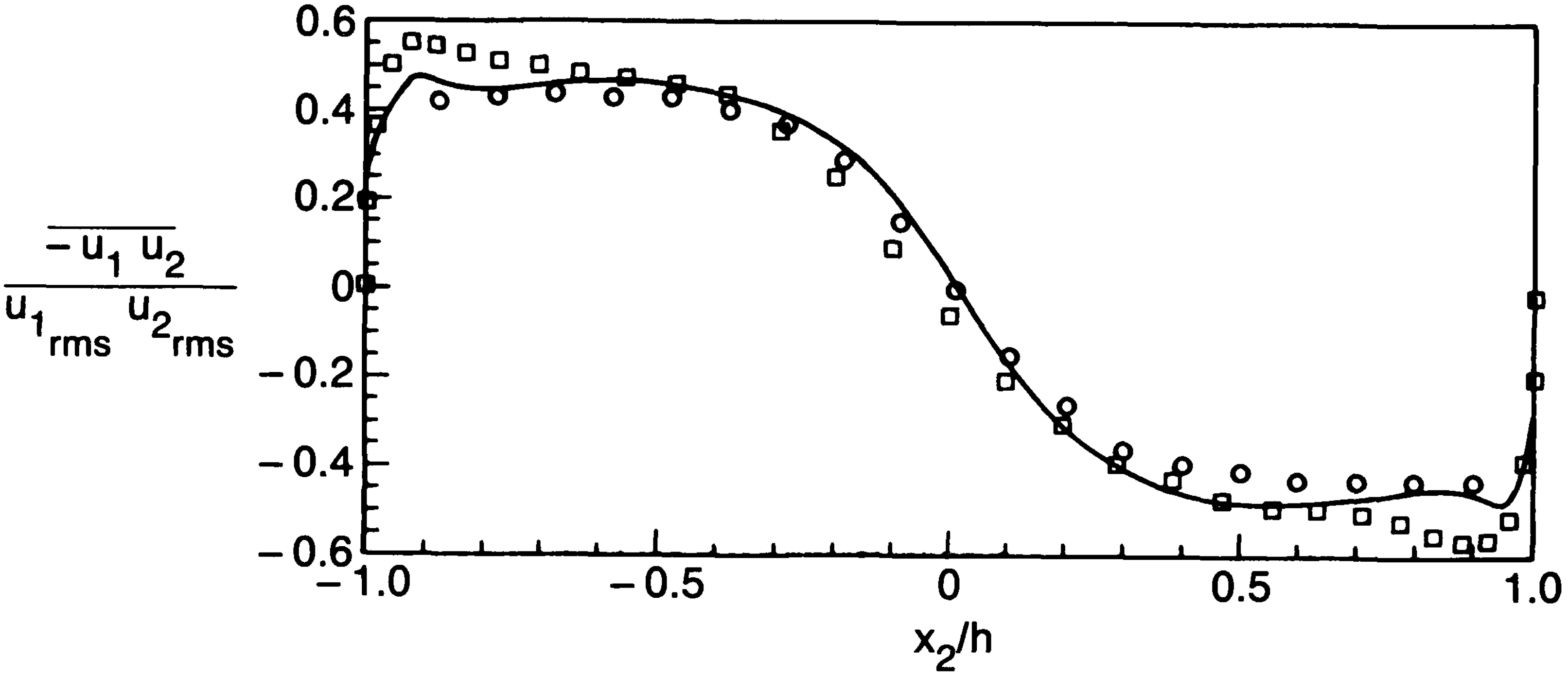

Fig. 7 — $u_1 - u_2$ Correlation Coefficient. □ Current results; —, KMM; o, Sabot and Comte-Bellot (1976).

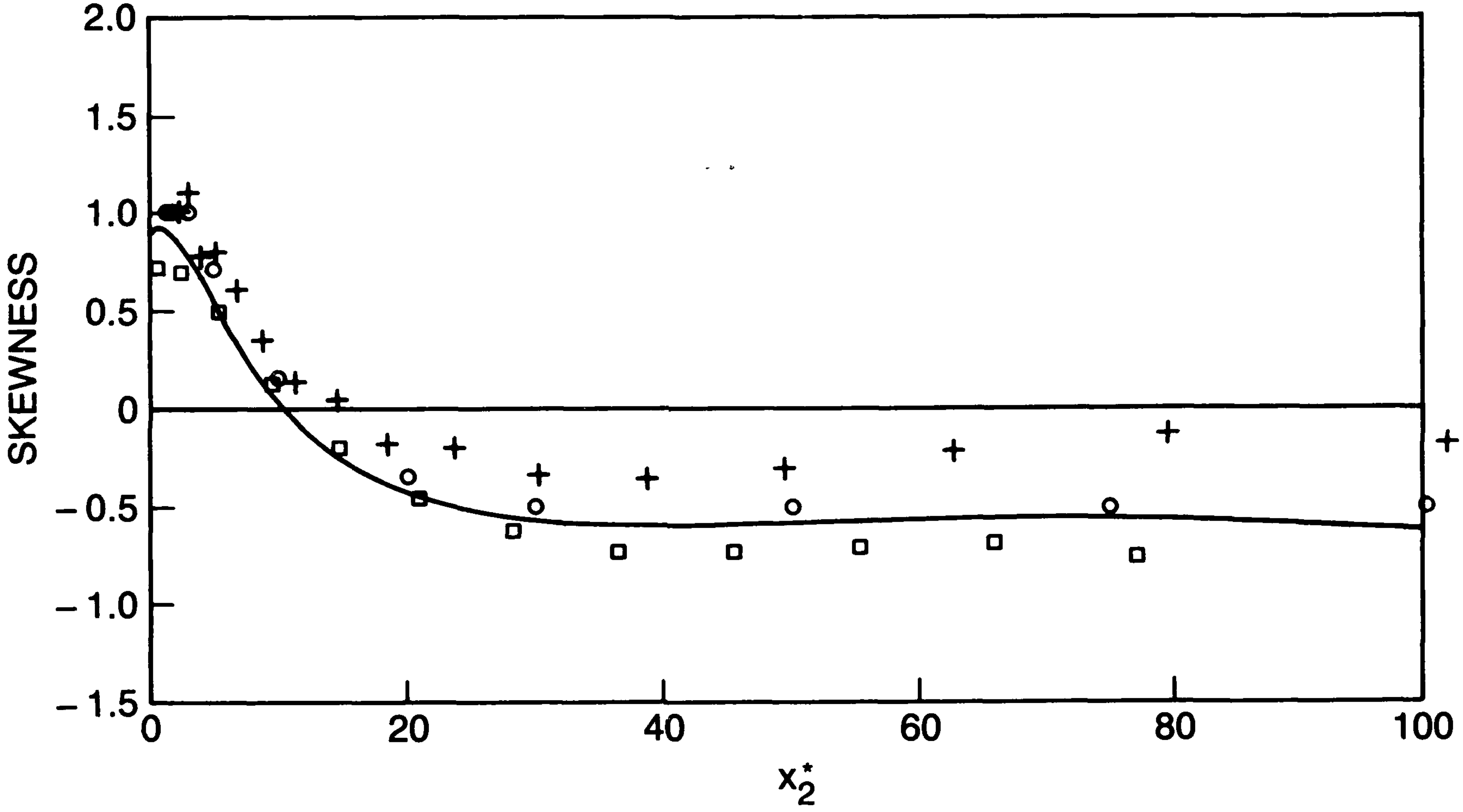

Fig. 8 — Skewness for u_2. □, Current results; —, KMM; +, Barlow and Johnston (1985); o, Kreplin and Eckelmann (1979).

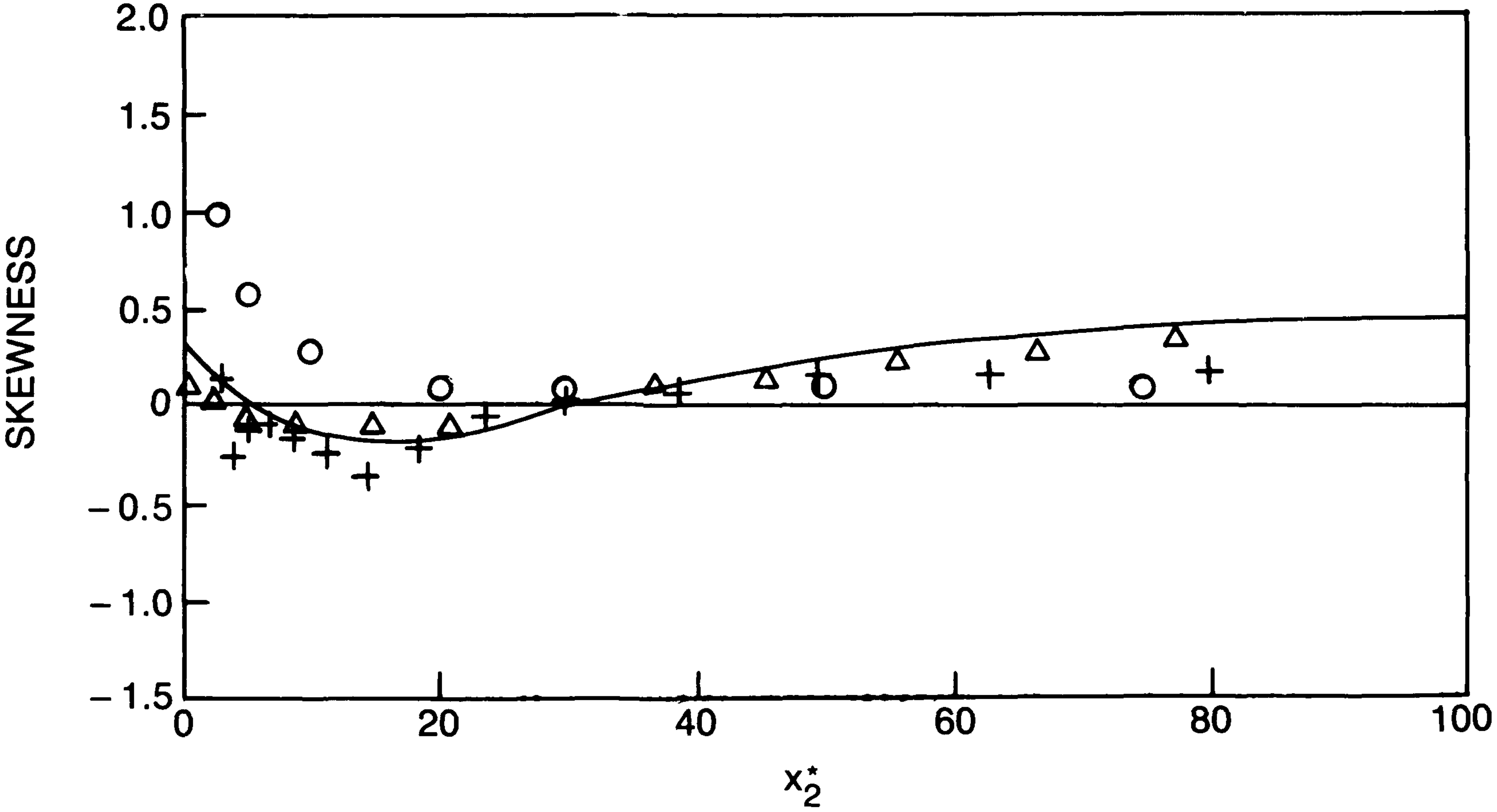

Fig. 9 — Skewness for u_2. Δ, Current results; —, KMM; +, Barlow and Johnston (1985); o, Kreplin and Eckelmann (1979).

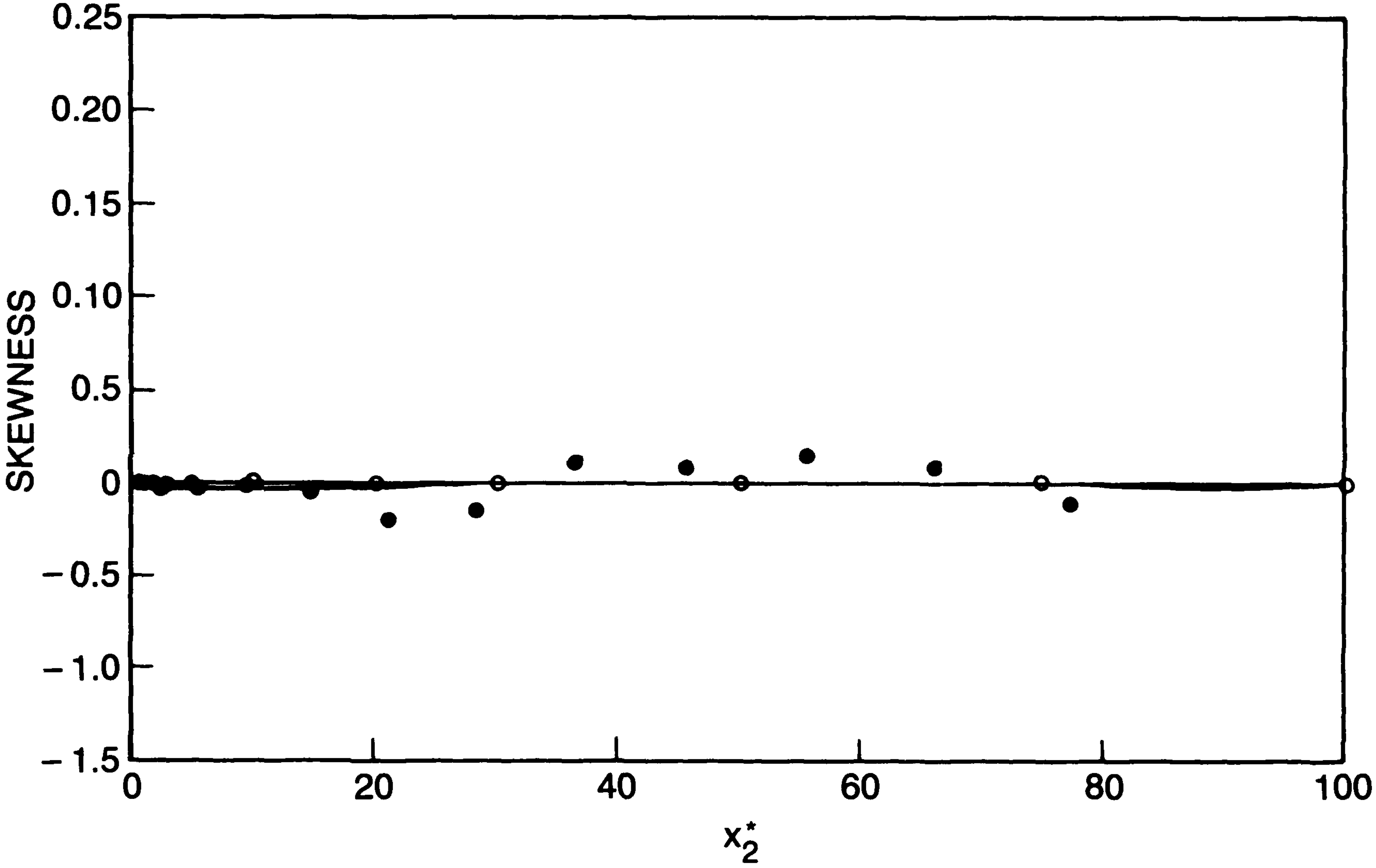

Fig. 10 — Skewness for u_3. ●, Current results; —, KMM; o, Kreplin and Eckelmann (1979).

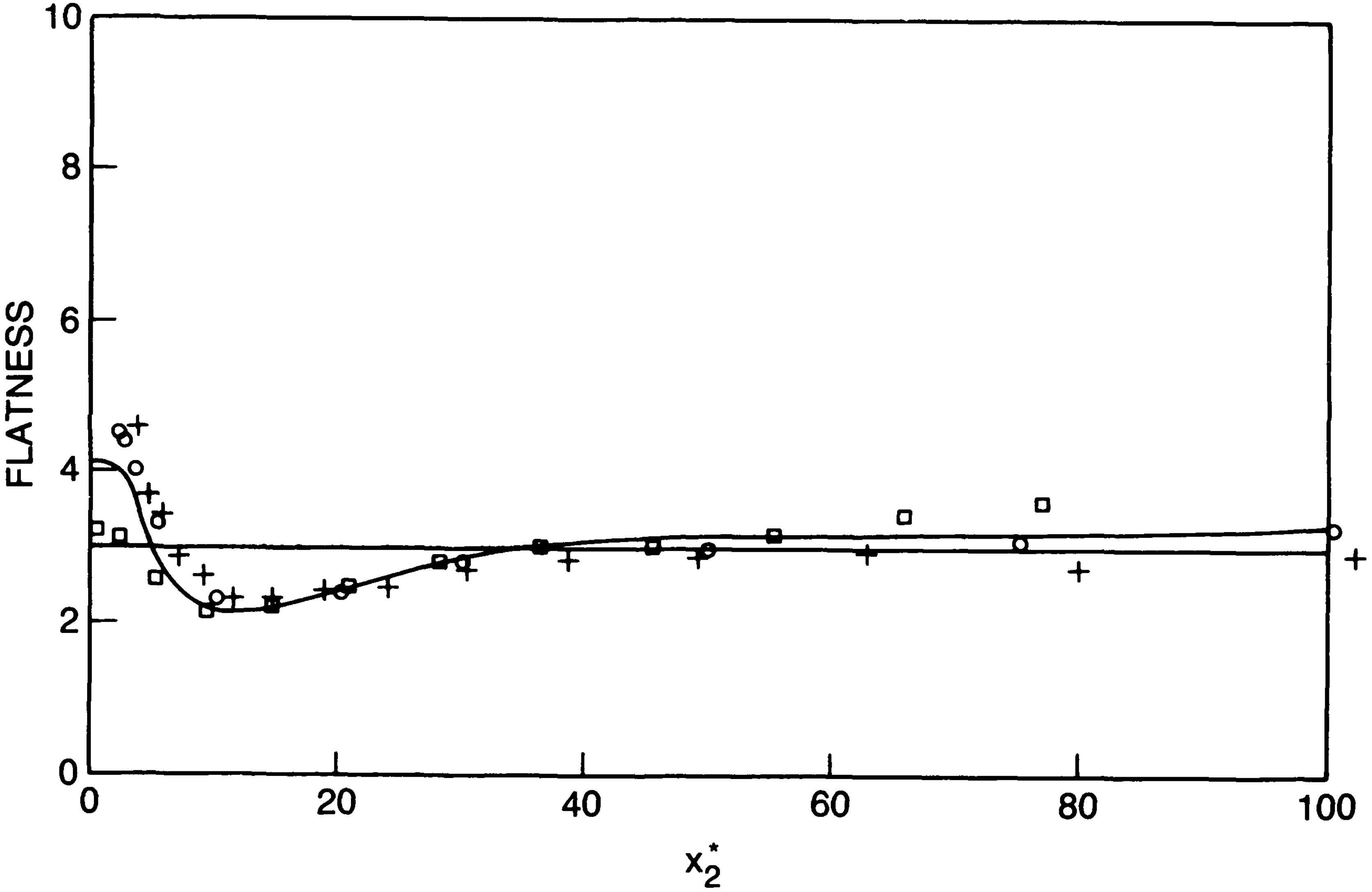

Fig. 11 — Flatness for u_1. o, Kreplin and Eckelmann (1979). □, Current results; —, KMM; +, Barlow and Johnston (1985); ○, Kreplin and Eckelmann (1979).

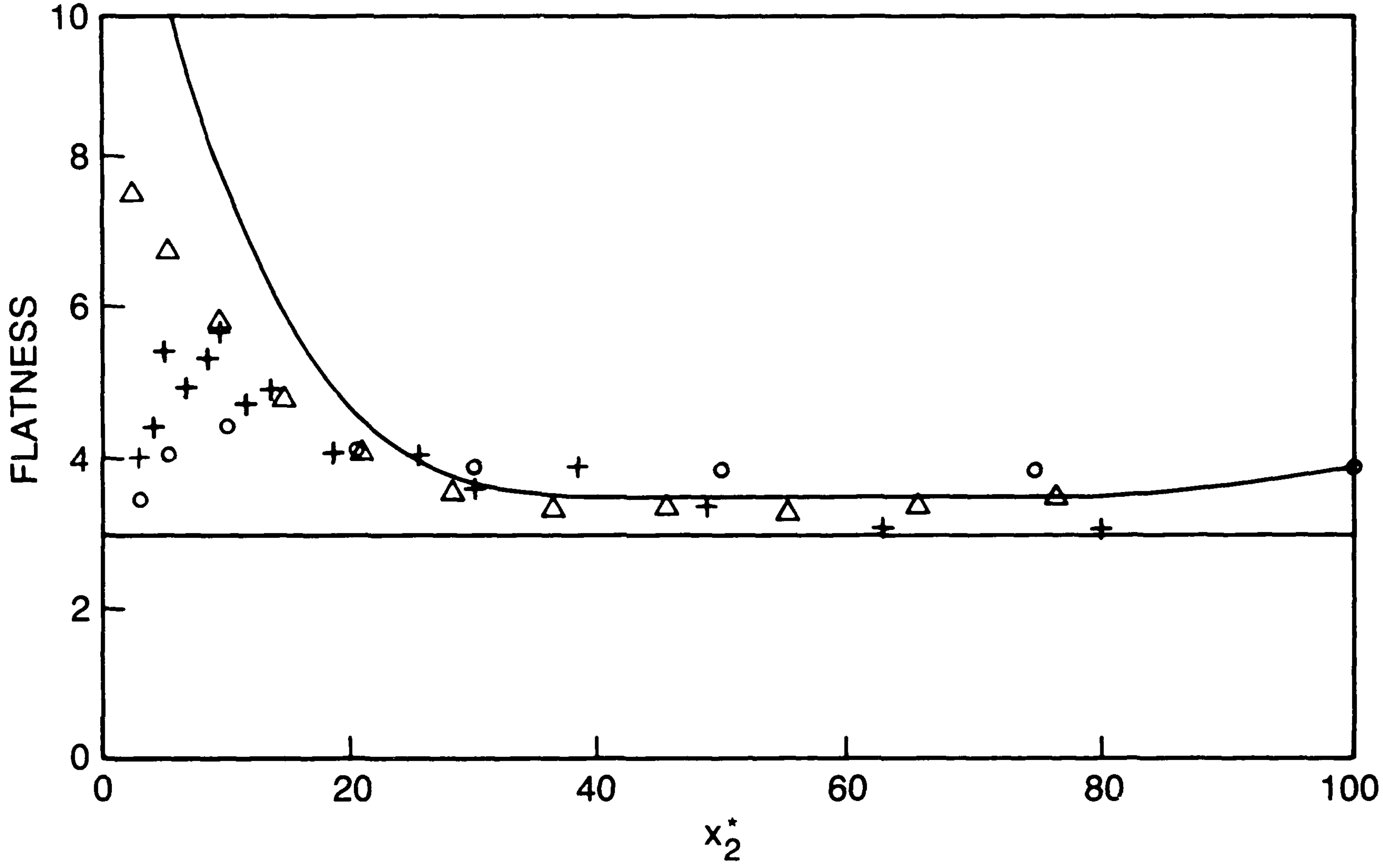

Fig. 12 — Flatness for u_2. Δ, Current results; — KMM; +, Barlow and Johnston (1985); o, Kreplin and Eckelmann (1979).

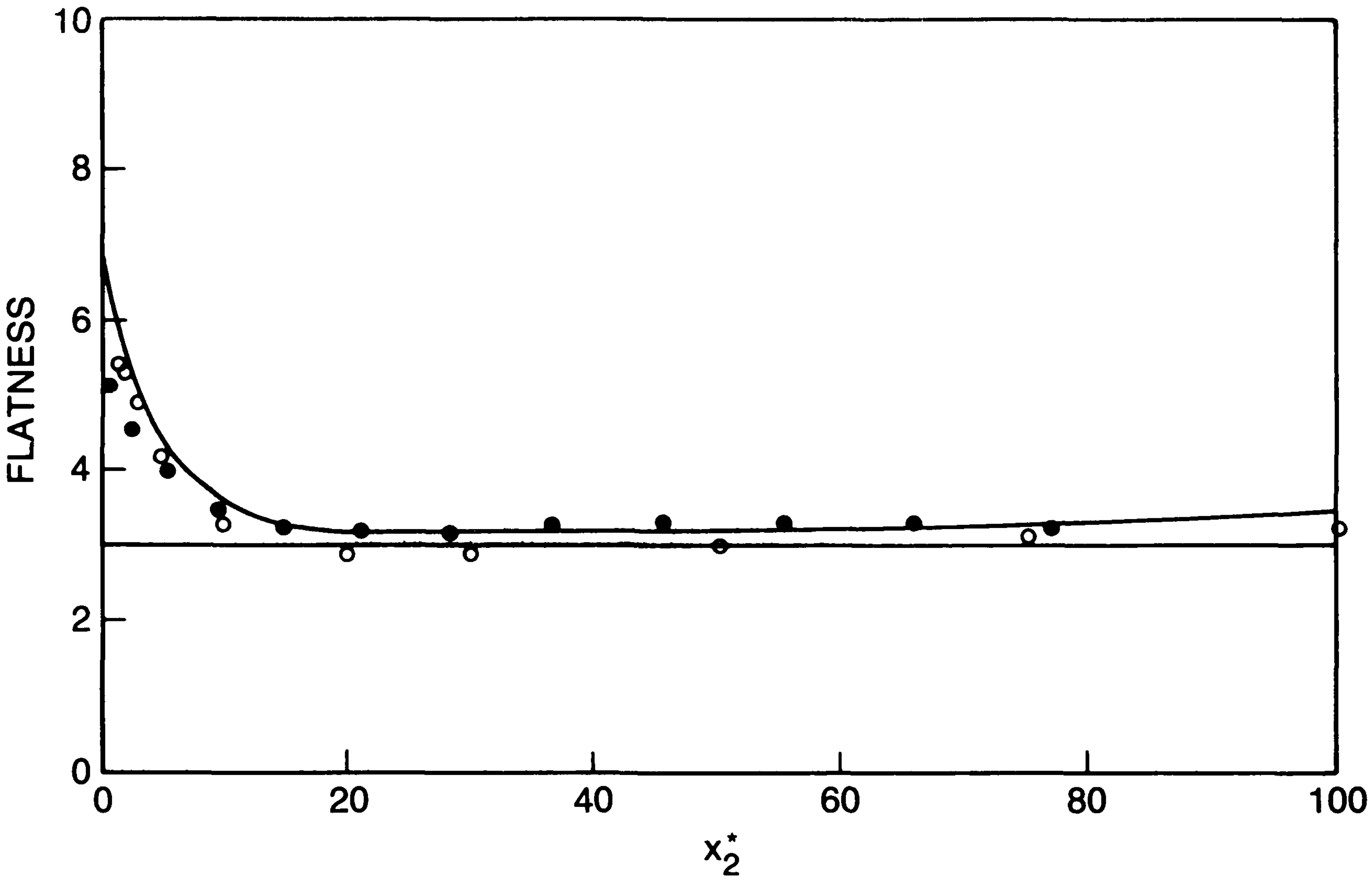

Fig. 13 — Flatness for u_3. ●, Current results; —, KMM; o, Kreplin and Eckelmann (1979).

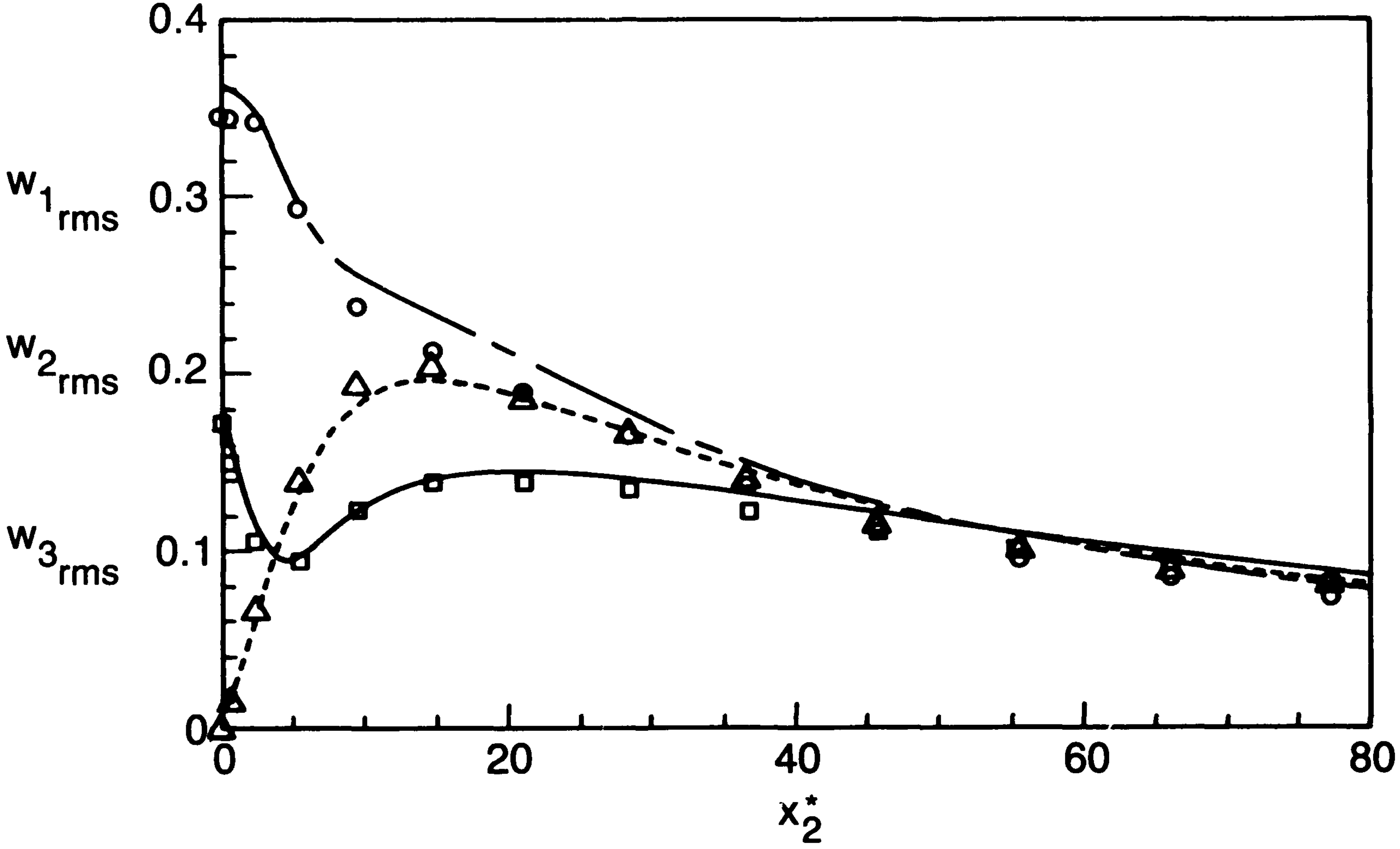

Fig. 14 — Fluctuating Vorticity Profiles, normalized by inner variables. □, ω_1, Δ, ω_3, Current results; —, ω_1, ----, ω_2 — - —, ω_3, KMM; □, ω_1, ●, ω_3, Kreplin and Eckelmann (1979).

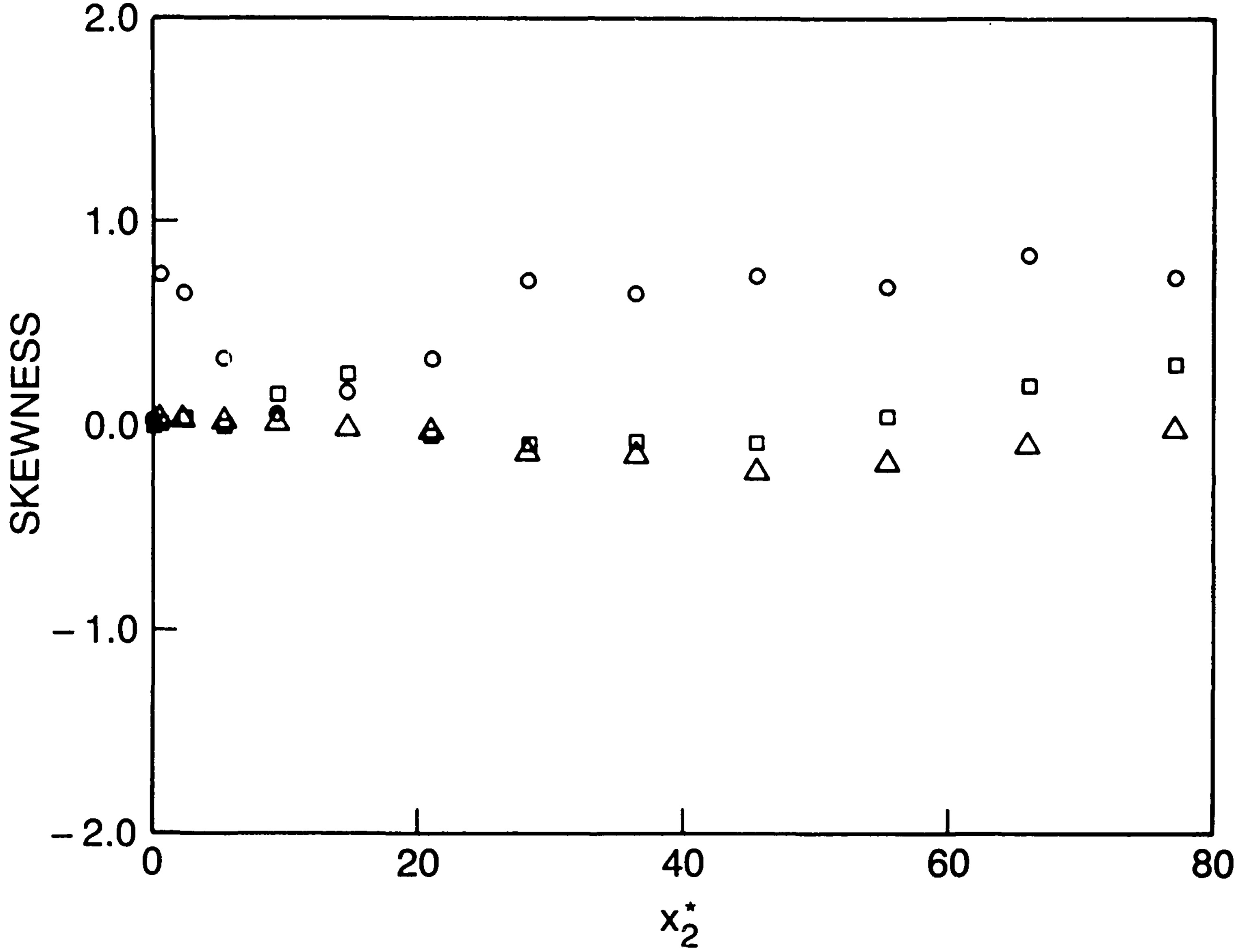

Fig. 15 — Skewness of the Vorticity Fluctuations. □, ω_1, Δ, ω_2, o, ω_3, Current results.

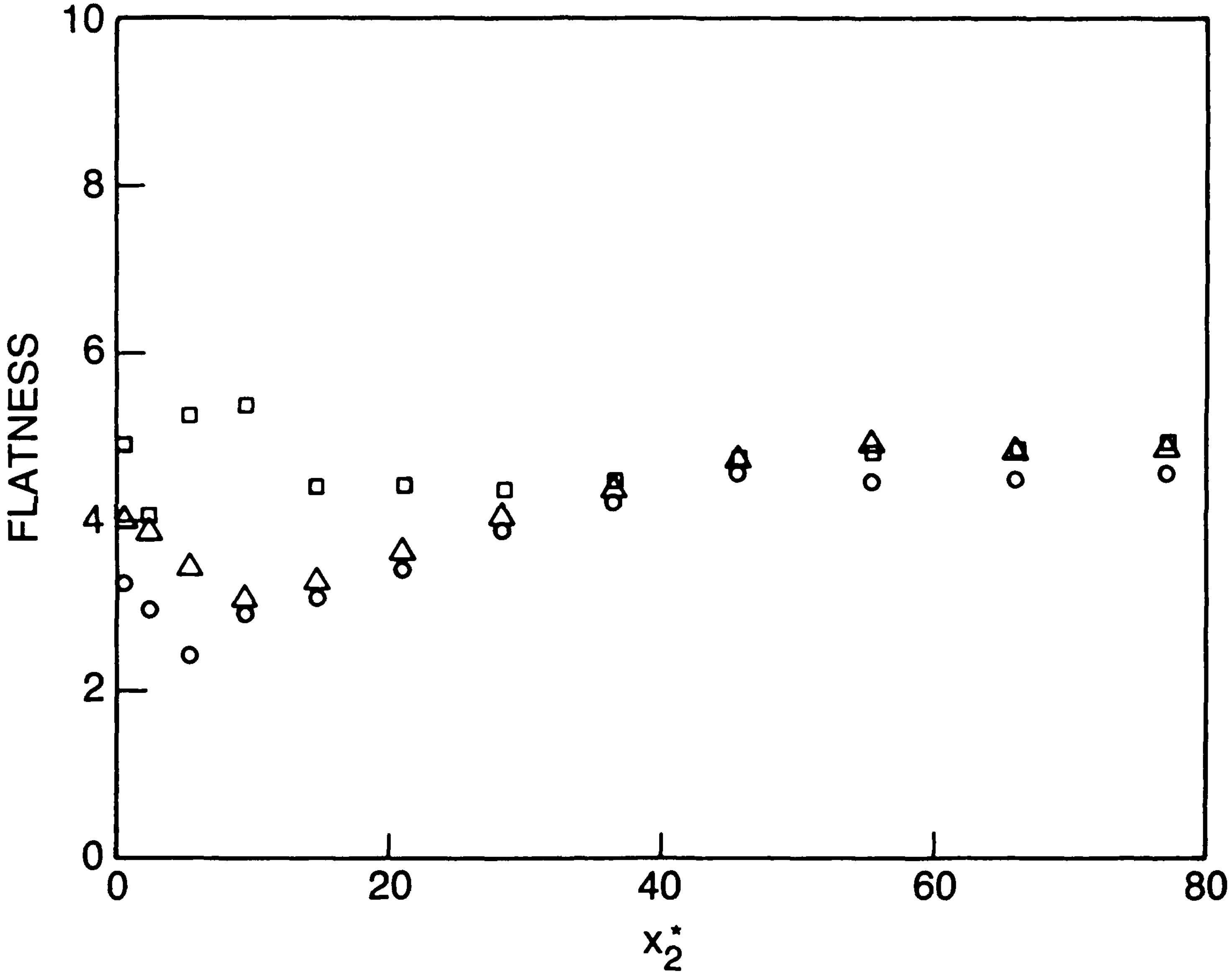

Fig. 16 — Flatness of the Vorticity Fluctuations. □, ω_1 Δ, ω_2, o, ω_3, Current results.

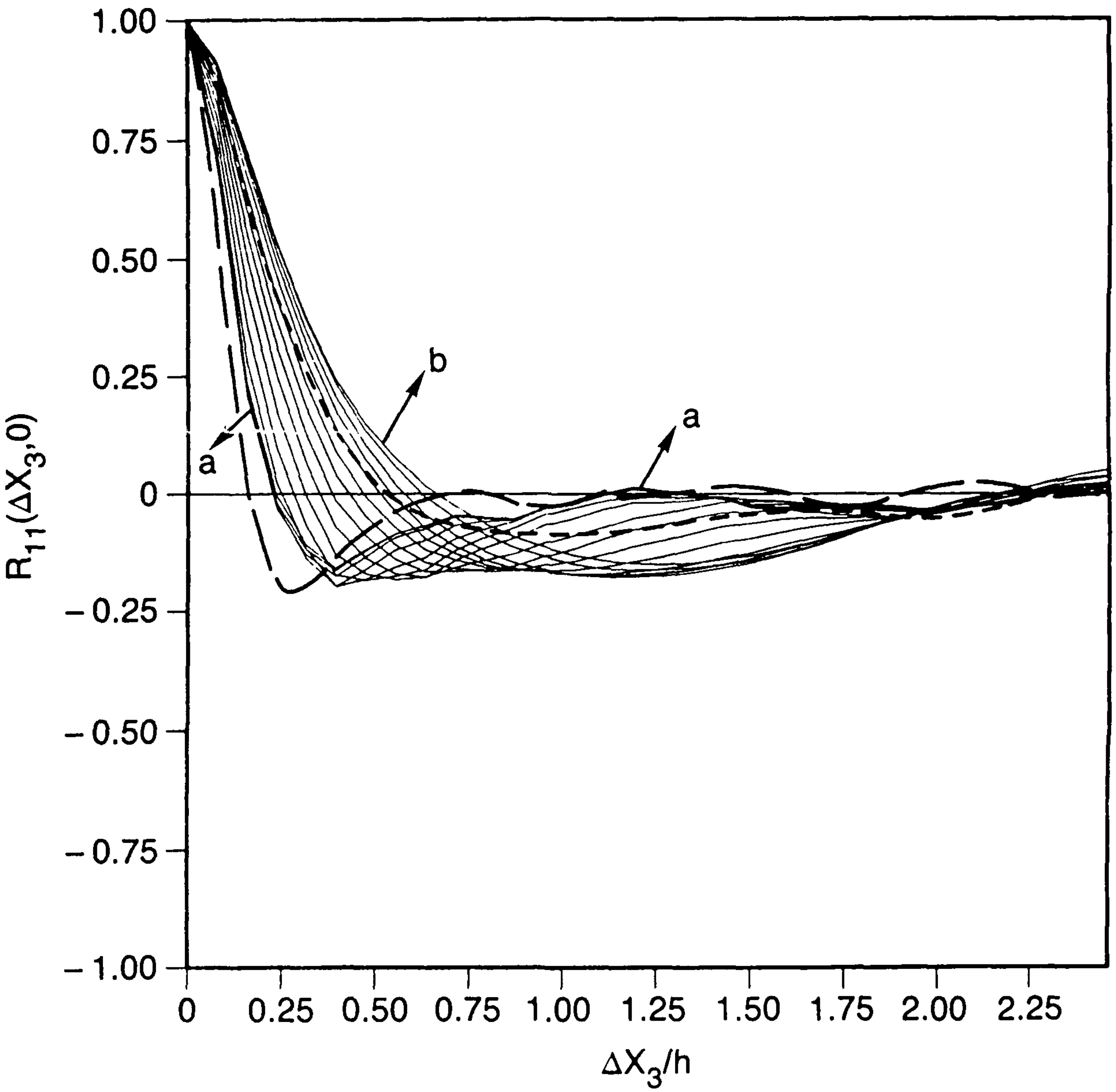

Fig. 17(a) — Spanwise dependence of the correlation function. Streamwise velocity. a: x_2^* = 0.062, b: x_2^* = 125, Current results; ----, x_2^* = 5.39, ----, x_2^* = 149.23, KMM.

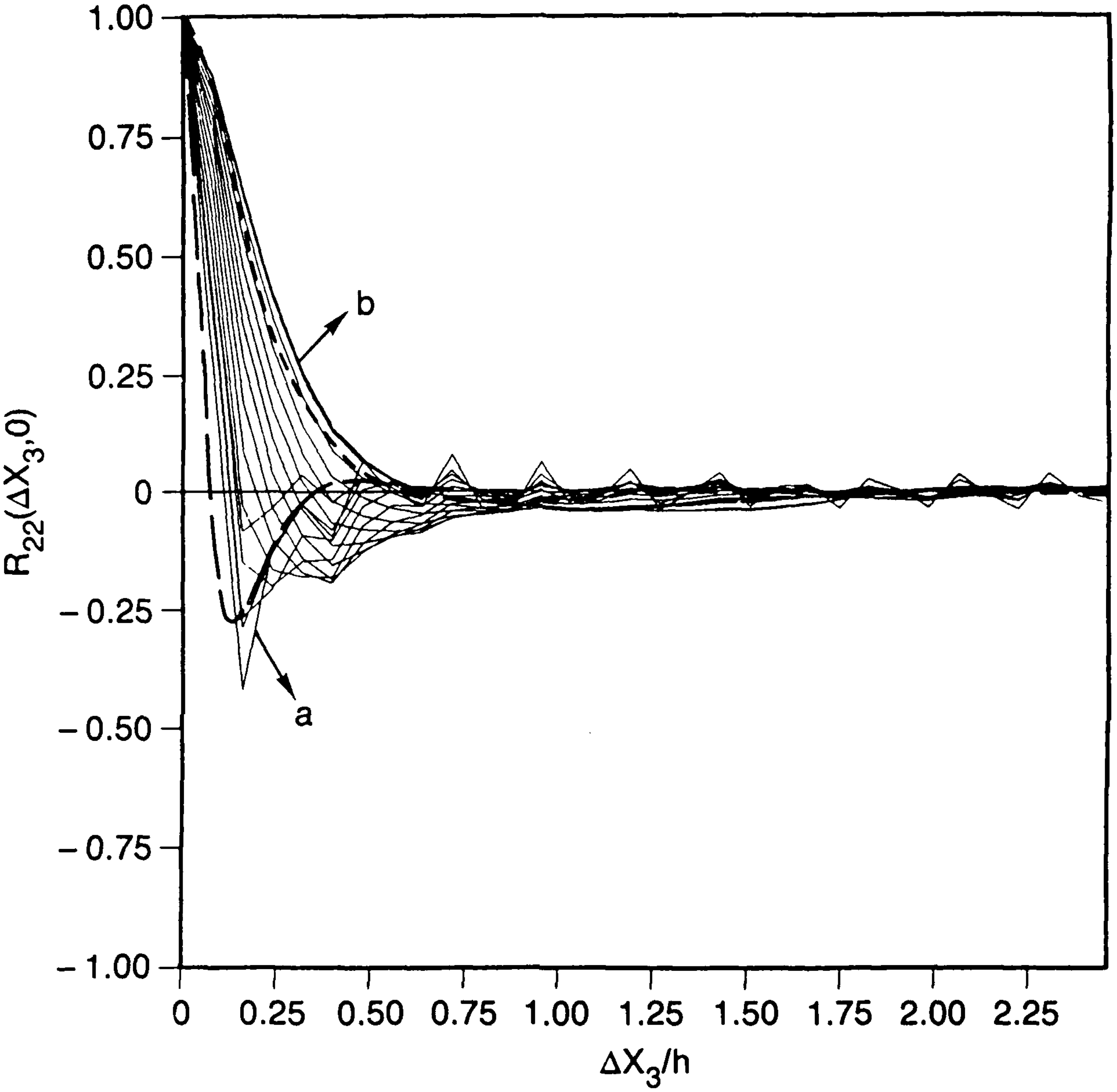

Fig. 17(b) — Spanwise dependence of the correlation function. Wall-normal velocity. a: 2.402, b: 125, Current results; ---, $x_2^* = 5.39$, -----, 149.23, KMM.

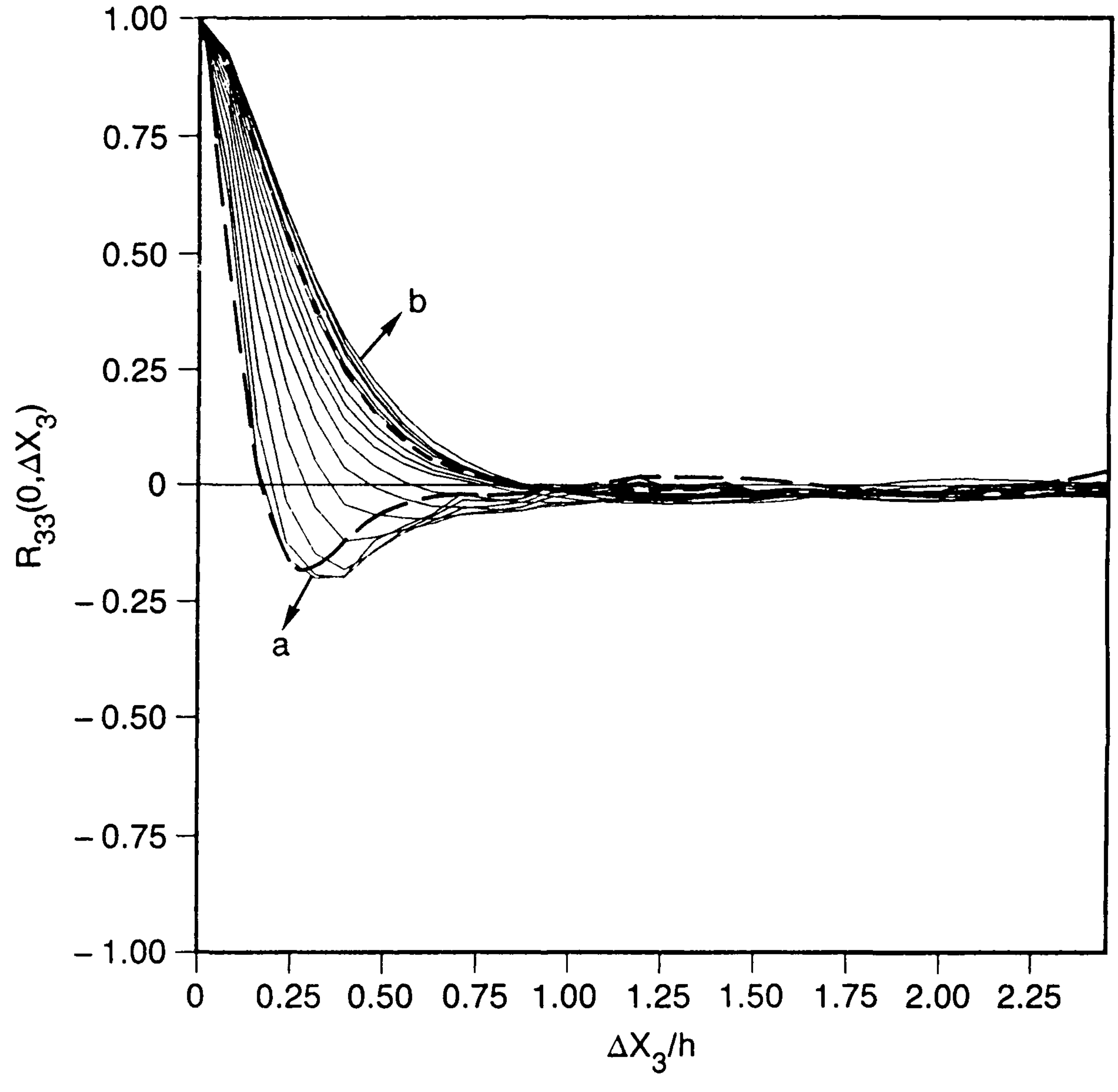

Fig. 17(c) — Spanwise dependence of the correlation function. Spanwise velocity. a: 0.602, b: 125, Current results; ----, 5.39, ----, 149.23, KMM.

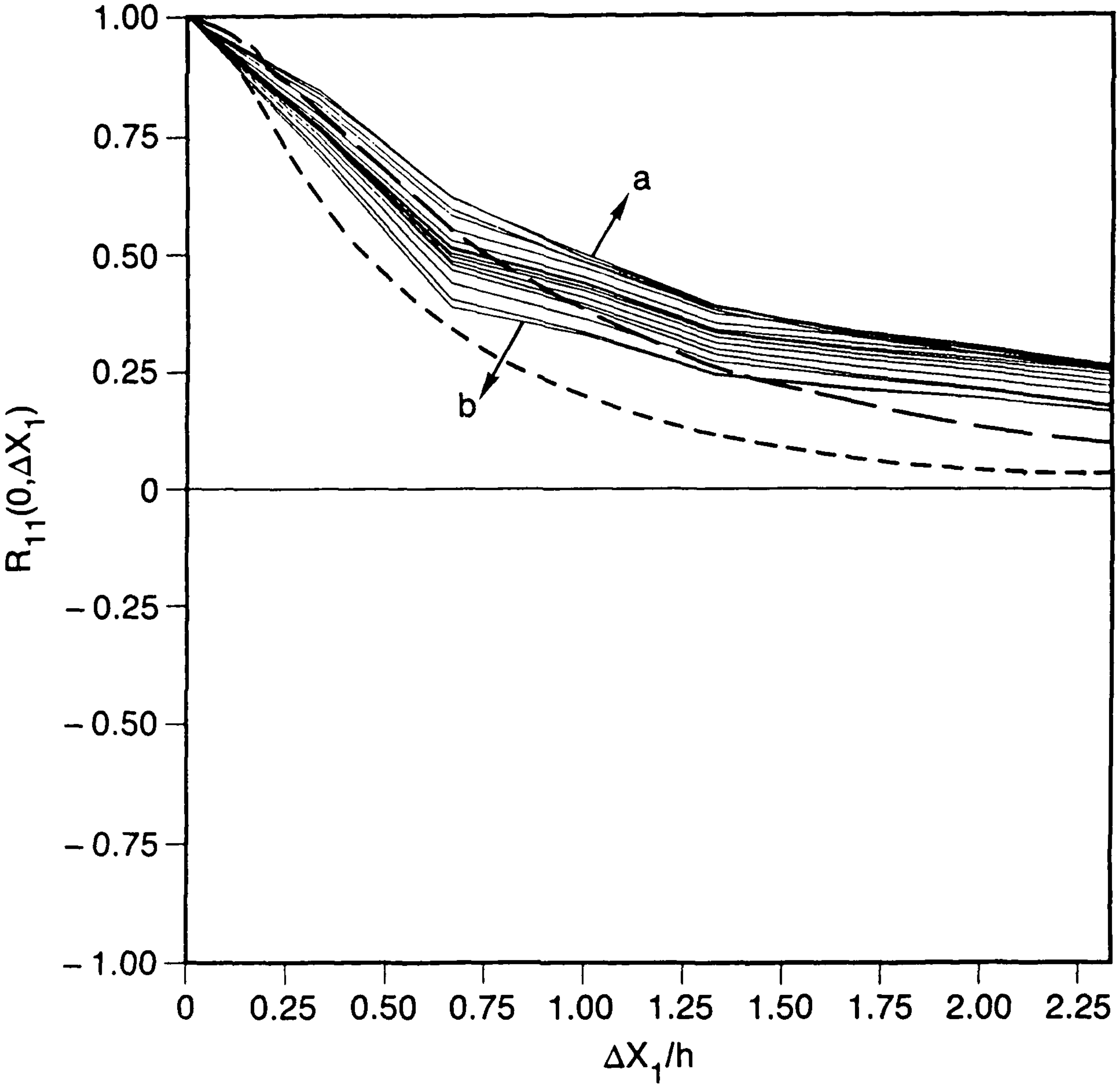

Fig. 18(a) — Streamwise dependence of the correlation function. Streamwise velocity. a: $x_2^* = 0.602$, b: $x_2 = 125$, Current results; ---, $x_2^* = 5.39$, ----, $x_2^* = 149.23$, KMM.

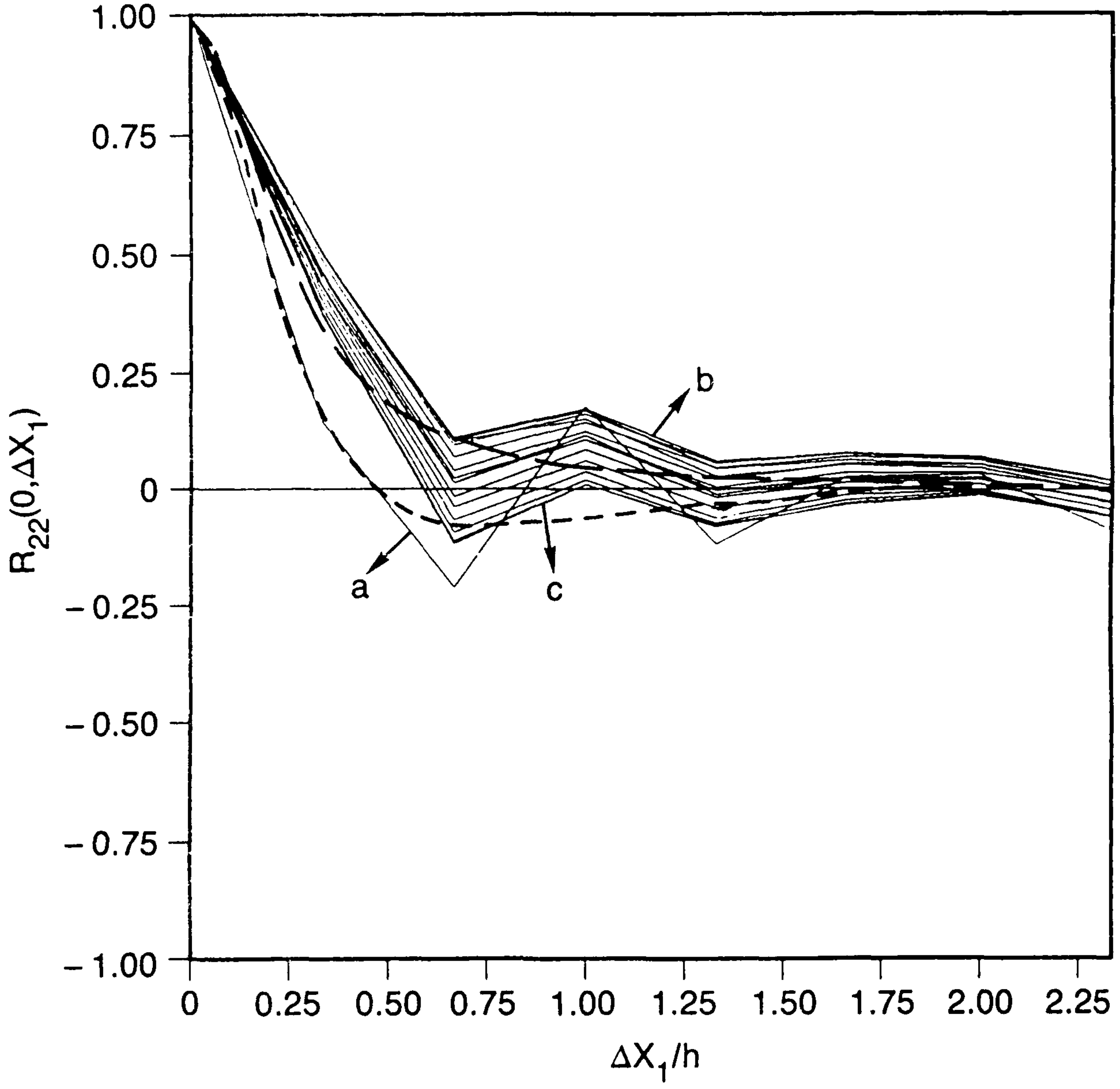

Fig. 18(b) — Streamwise dependence of the correlation function. Wall-normal velocity. a: 0.602, b: 2.402, c: 125, Current results; -----, 5.39, ----, 149.23, KMM.

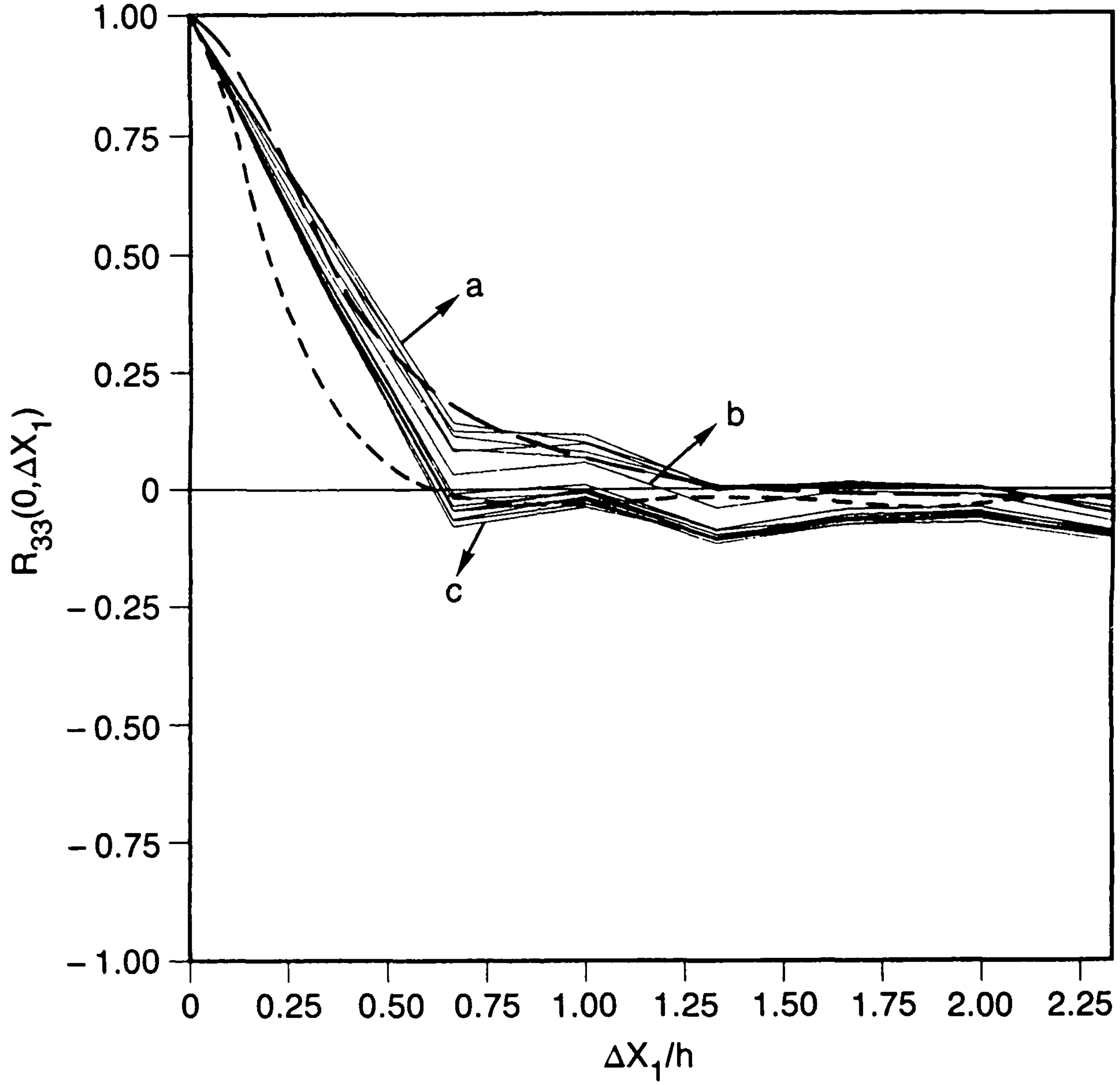

Fig. 18(c) — Streamwise dependence of the correlation function. Spanwise velocity. a: 0.602, b: 21.06, c: 125, Current results; ---, 5.39, ----, 149.23 KMM.

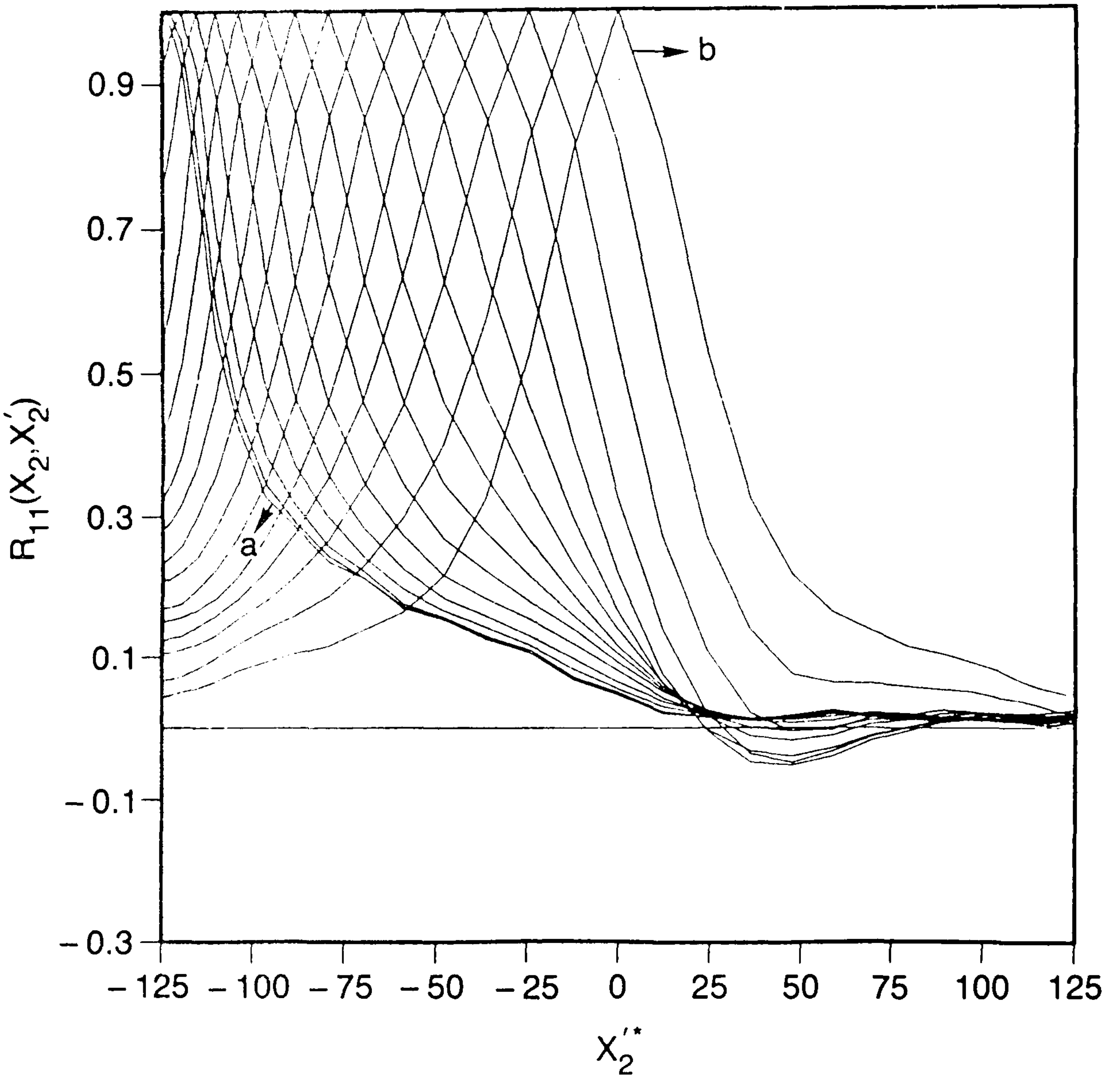

Fig. 19(a) – Wall-normal dependence of the correlation coefficient. Streamwise velocity. a: $x_2^* = 0.602$, b: $x_2^* = 125$.

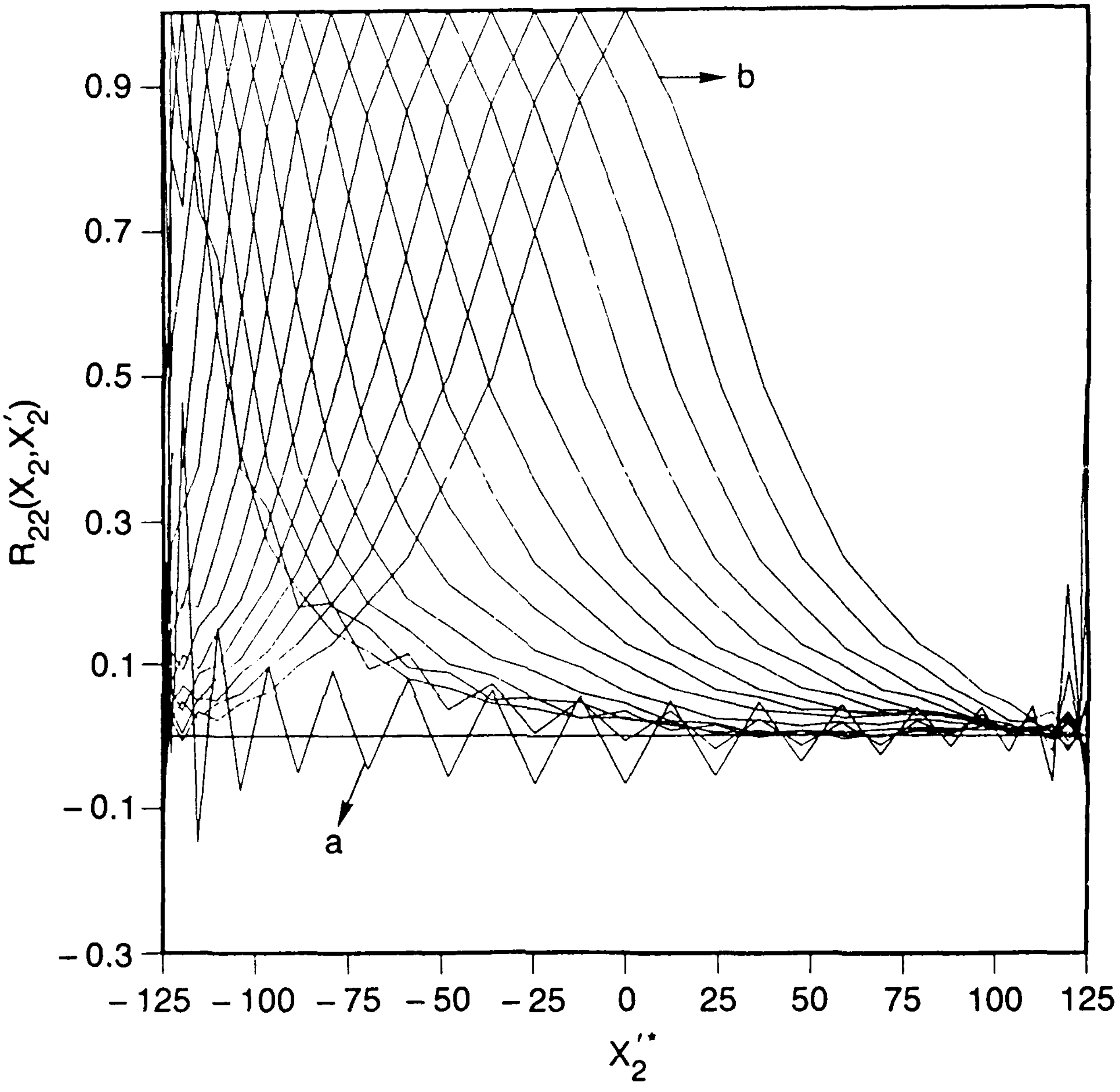

Fig. 19(b) — Wall-normal dependence of the correlation coefficient. Wall-normal velocity. a: 0.602, b: 125.

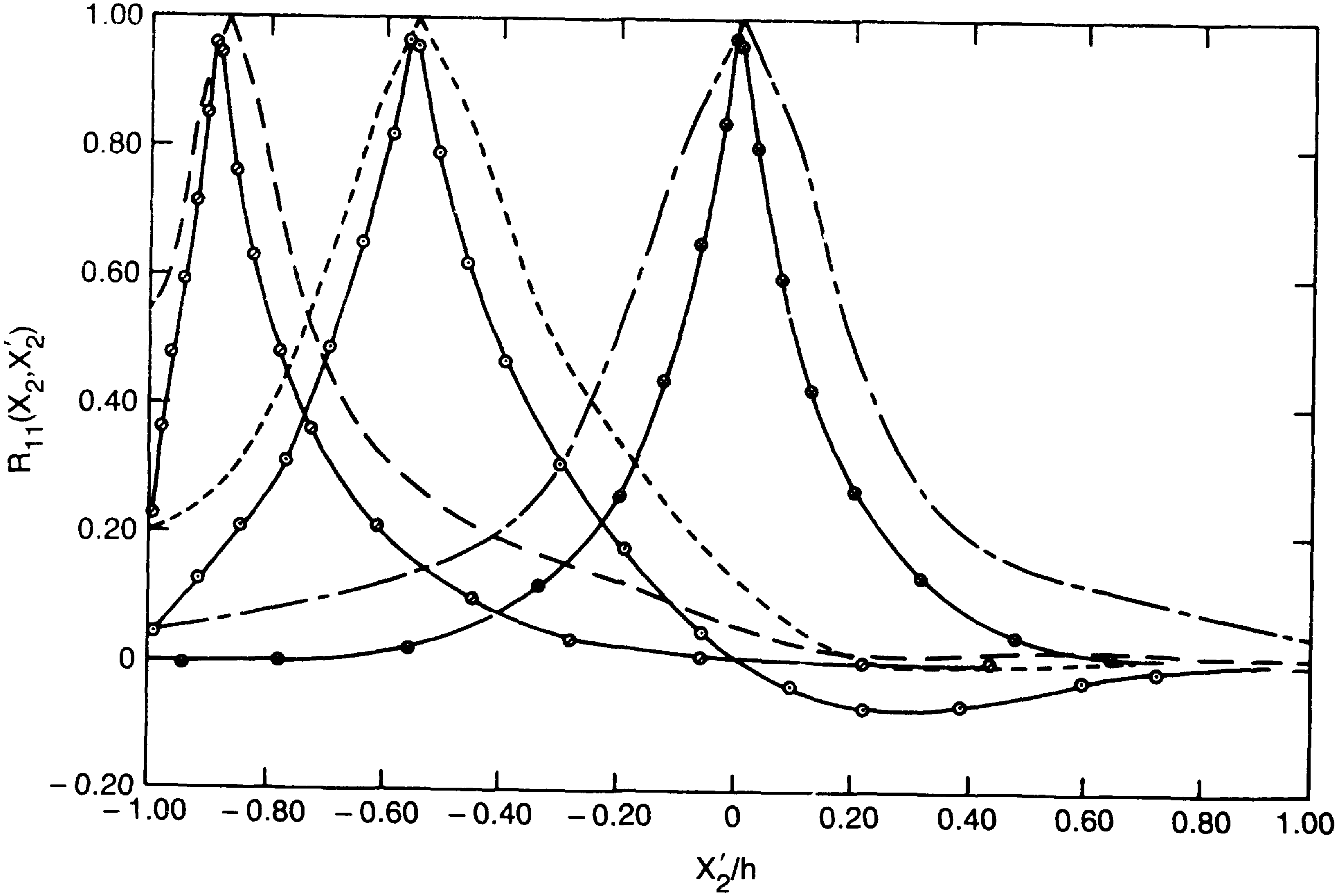

Fig. 20(a) — Wall-normal dependence of the correlation function compared with experiment. Streamwise velocity. Calculations: ———, $x_2/L_2 = 0.118$, ———, $x_2/L_2 = 0.4444$, $x_2/L_2 = 1.0$, — - —. Experiments of Comte-Bellot (1965) are designated by the markers. L_2 is the channel half-width.

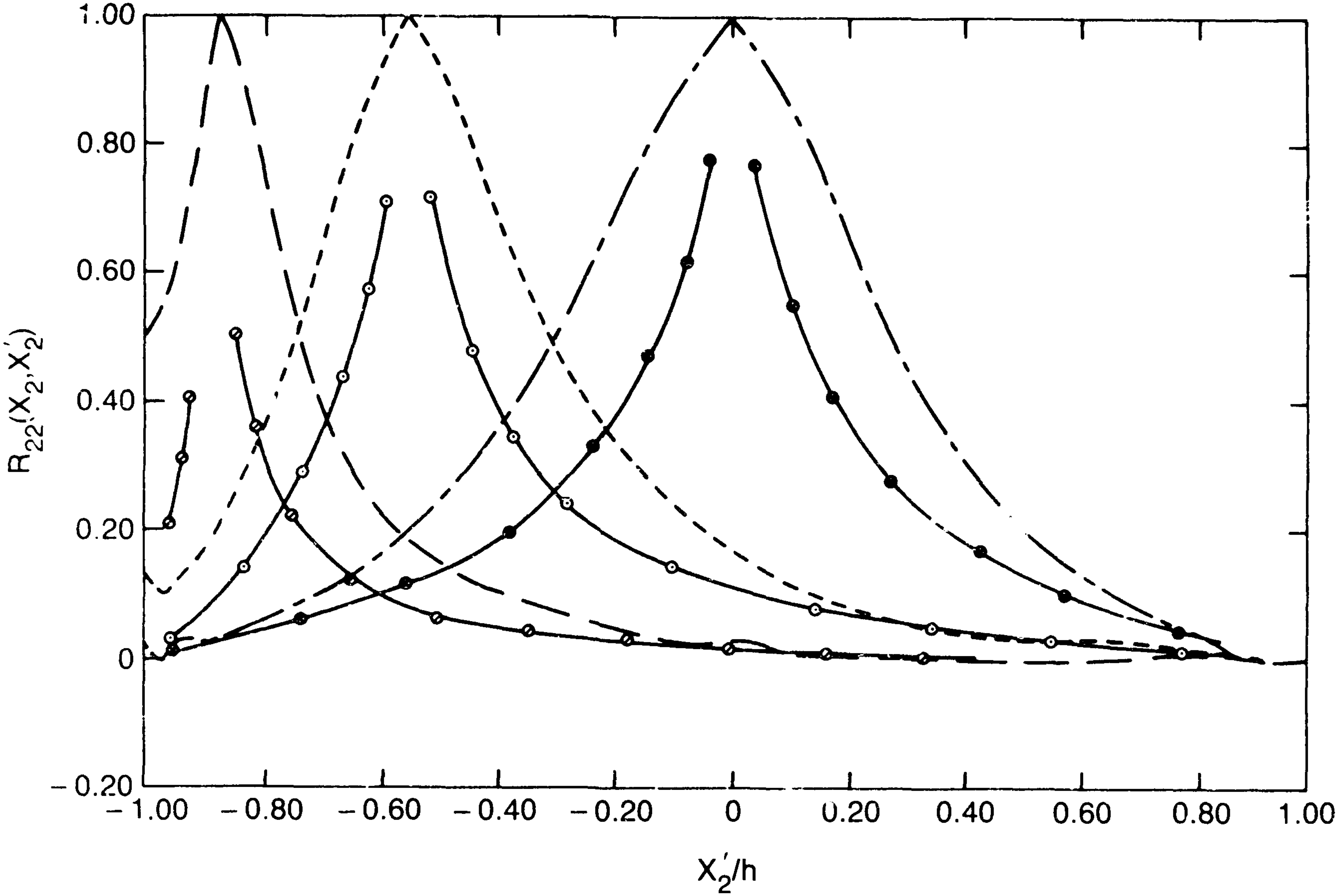

Fig. 20(b) — Wall-normal dependence of the correlation function compared with experiments. Wall-normal velocity.

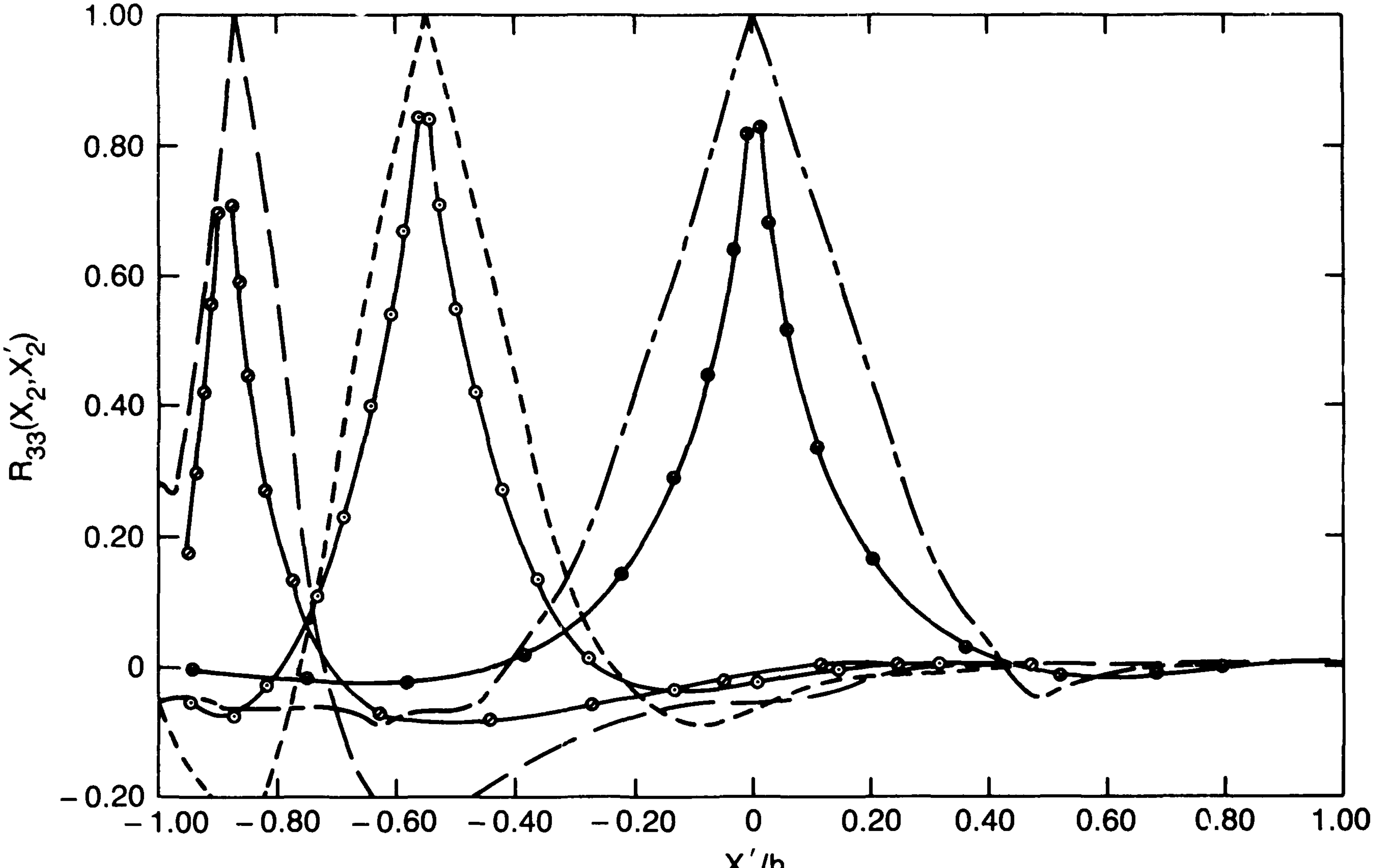

Fig. 20(c) — Wall-normal dependence of the correlation function compared with experiments. Spanwise velocity.

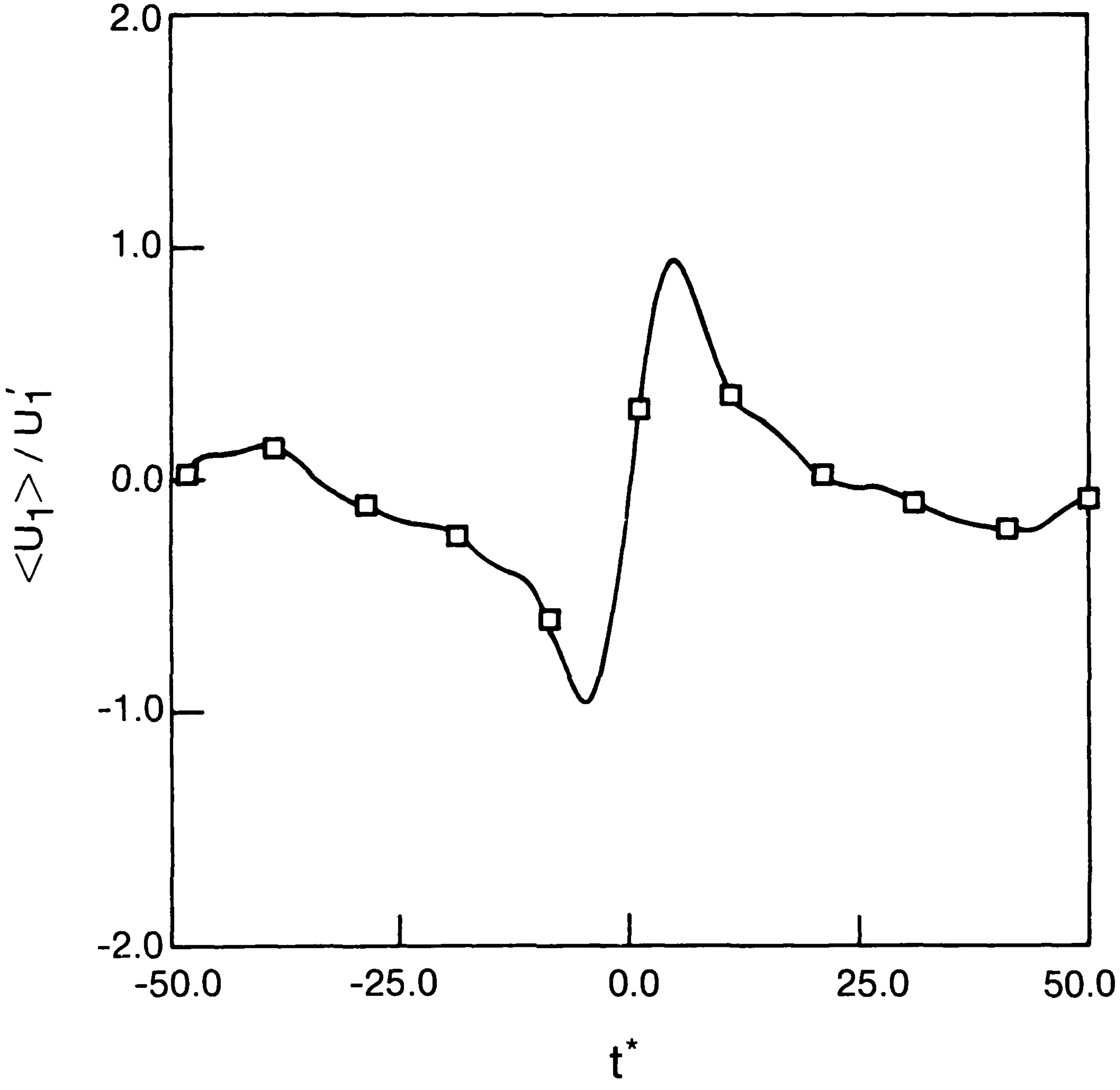

Fig. 21 — Ensemble average of the streamwise velocity for turbulent events detected with the VITA conditional sampling scheme. The detection parameters are: $k = 1.0$ and $T^* = 16$. The detection is located $15l^*$ above the wall.

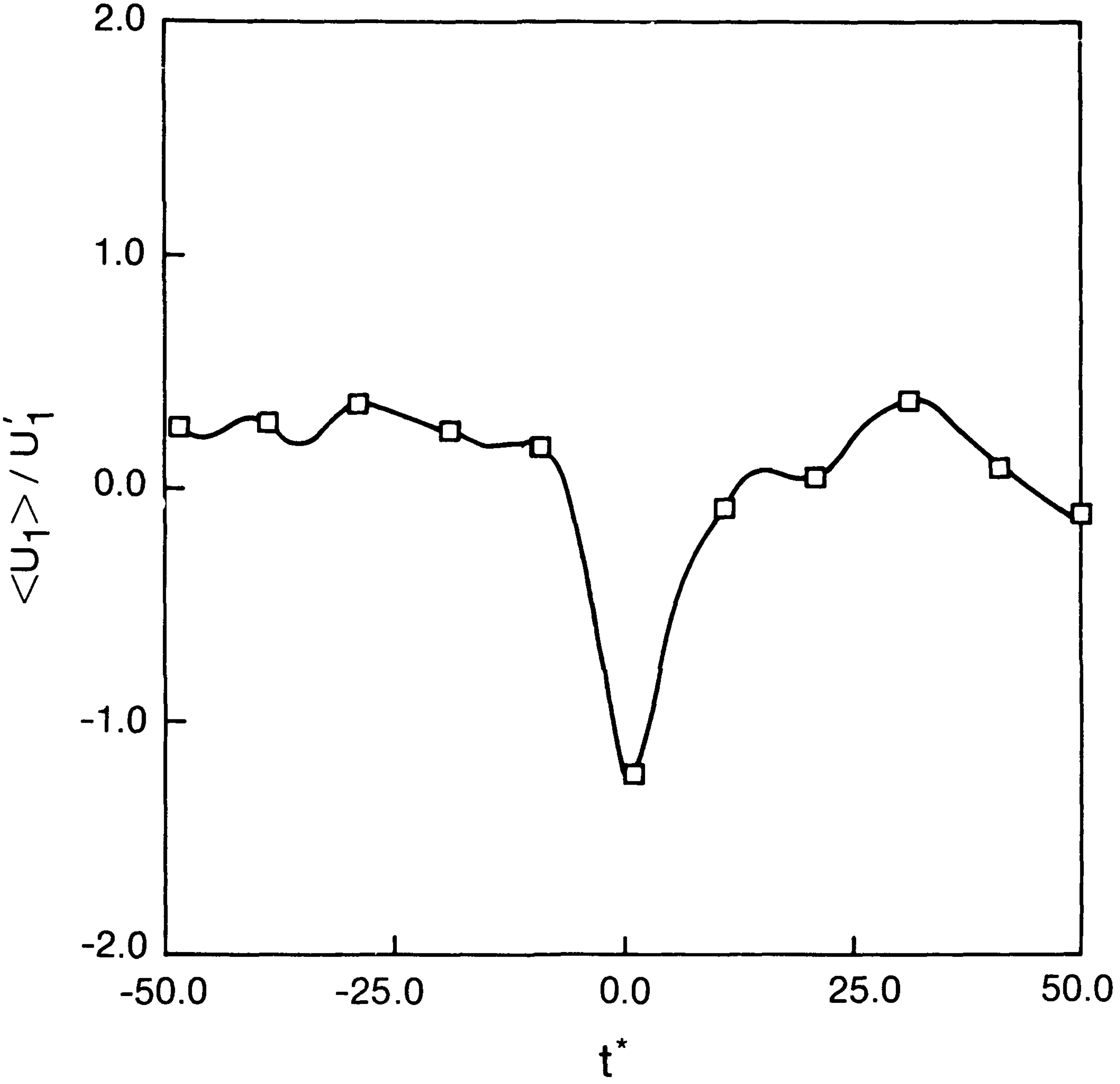

Fig. 22 — Ensemble average of the streamwise velocity for turbulent events detected with the Second Quadrant Reynolds stress conditional sampling scheme. The detection threshold is h = 1.0. The detetion is located 15l^* above the wall.

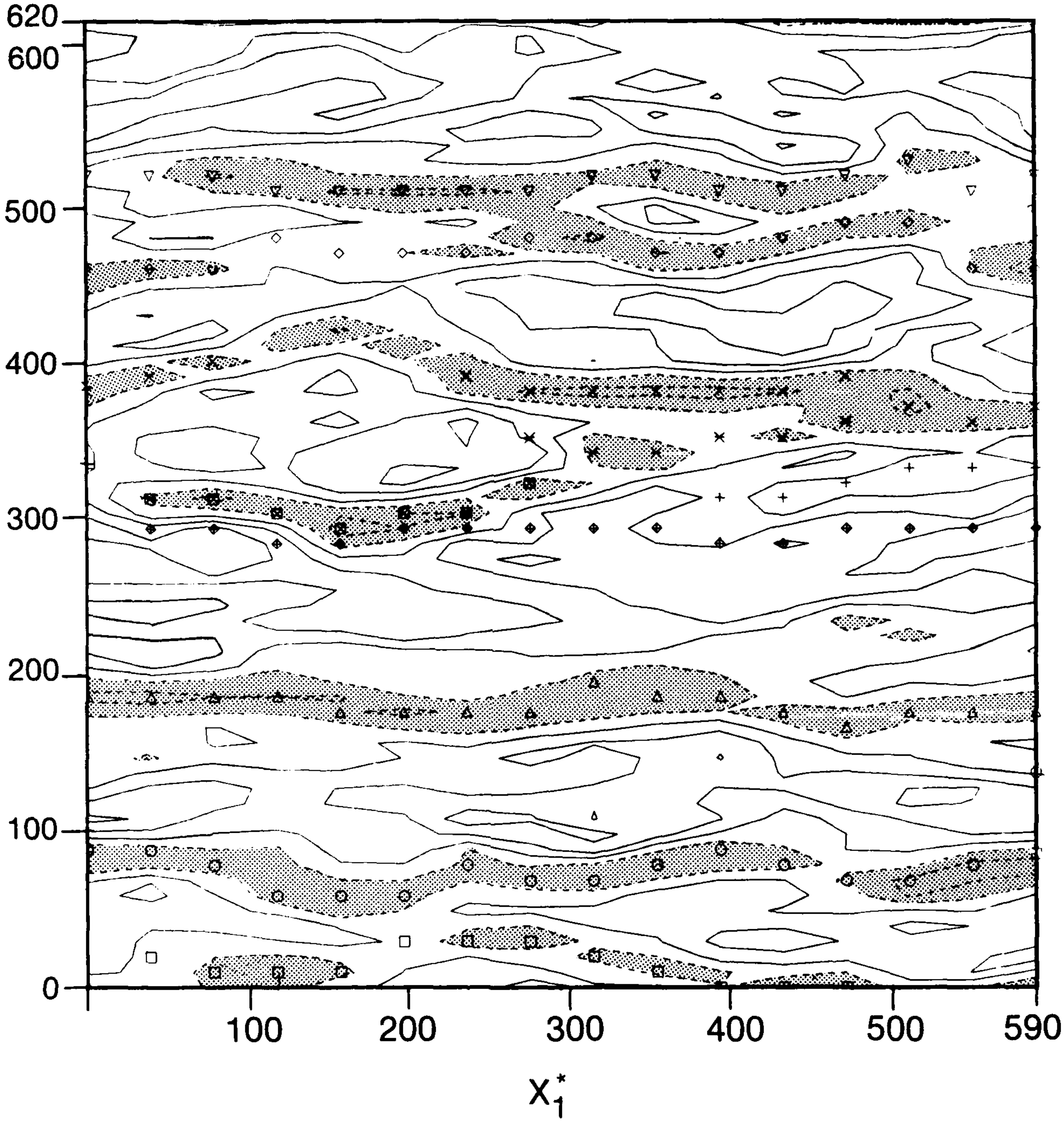

Fig. 23 — The fluctuating streamwise velocity contours in the buffer layer ($x_2^* = 15$). The markers are the detected low speed streaks and the shaded regions indicate fluctuating velocities less than $-u_1'$ ($x_2^* = 15$).

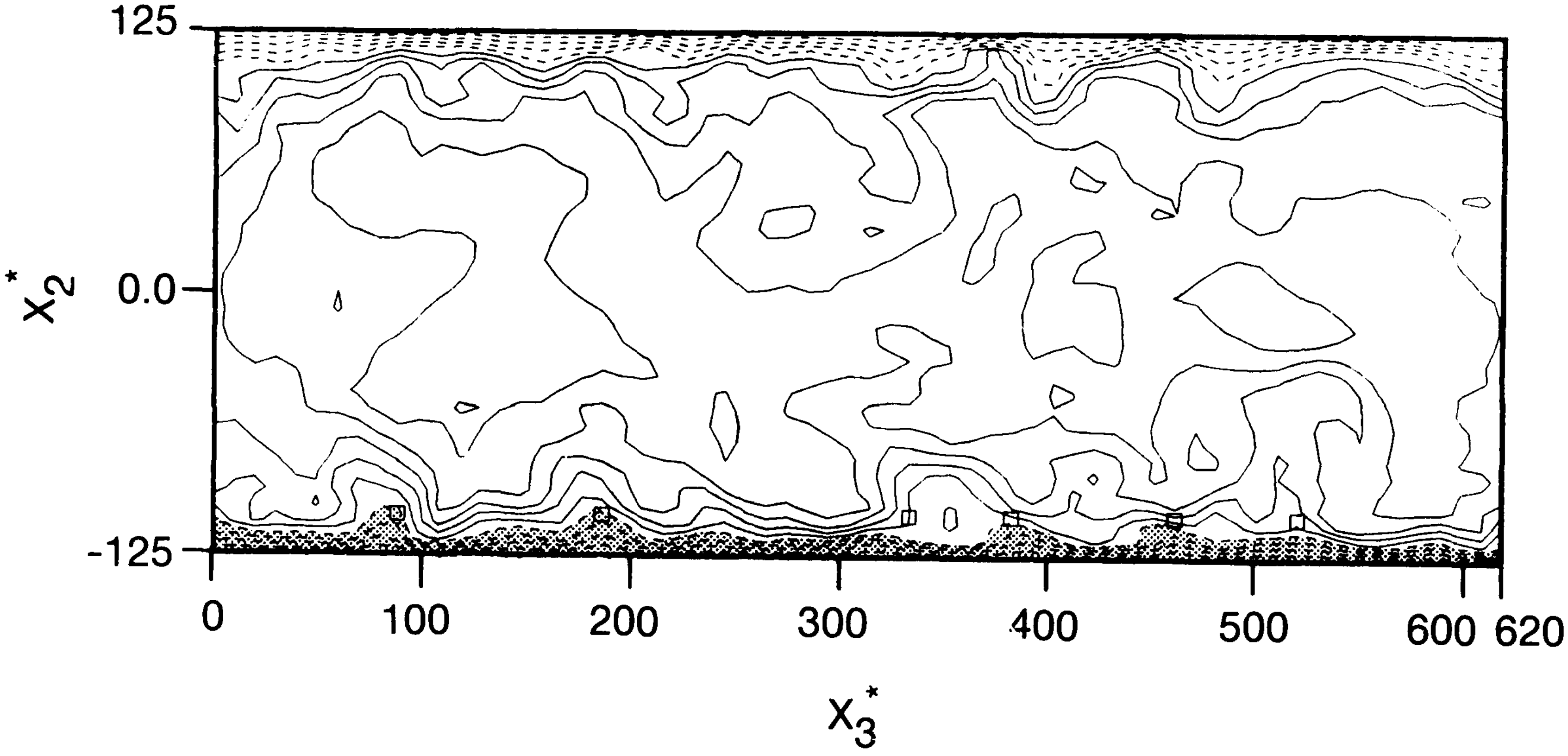

Fig. 24 — The fluctuating streamwise velocity contours across the channel looking downstream at $x_1^* = 0$. The markers are the detected low speed streaks and the shaded regions indicate fluctuating velocities less than $-u_1'(x_2^* = 15)$.

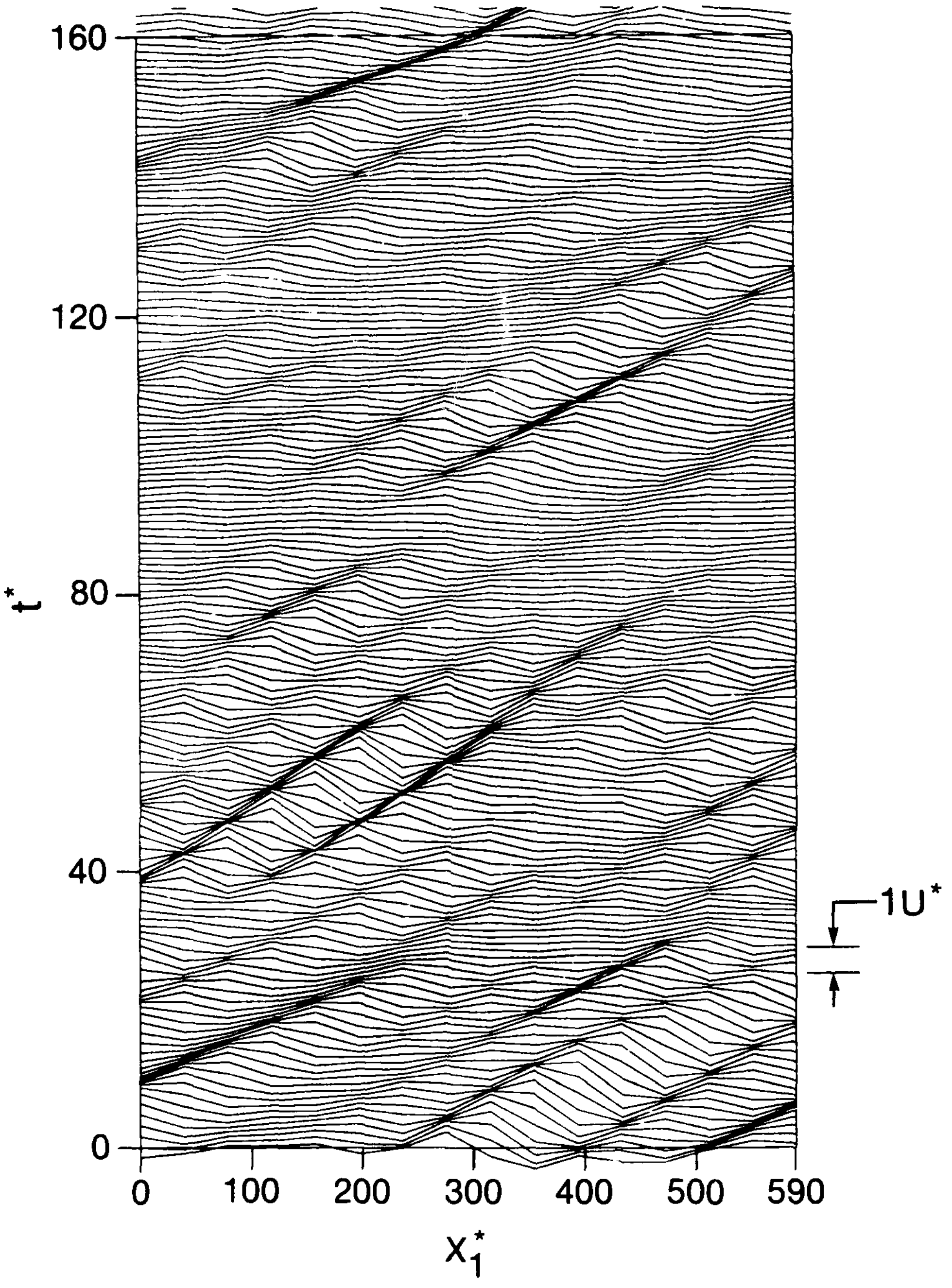

Fig. 25 — The normal velocity (u_2) in the vicinity of a low speed streak as a function of streamwise location and time, (x_1^*, t^*). The figure is of the velocity at a distance of $x_2^* = 15$. The regions of wavelike disturbance are localized pockets of second and fourth quadrant Reynolds stress.

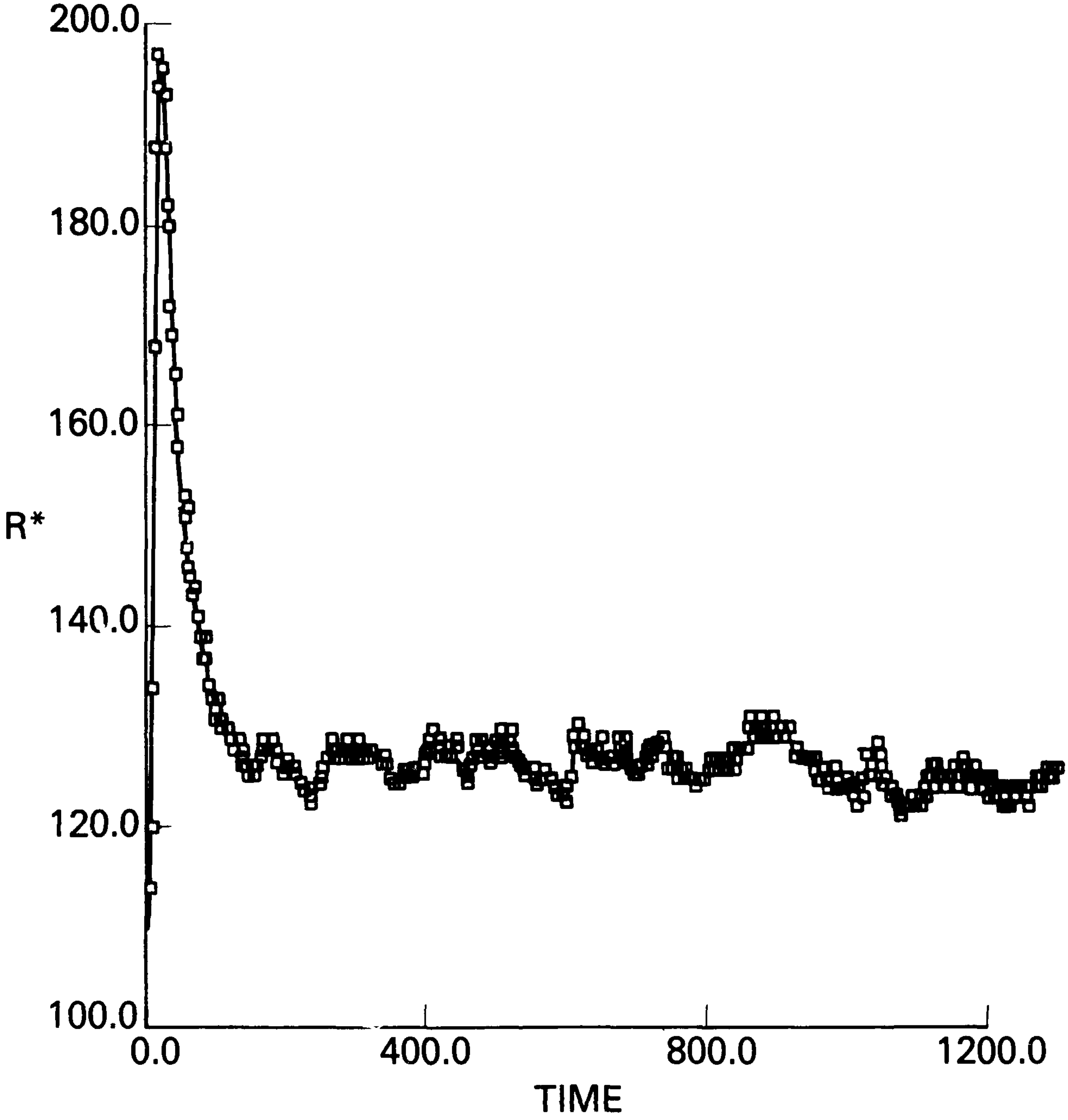

Fig. A1(a) — Wall Reynolds number versus time. Time is scaled wit centerline velocity and channel half-width. Grid resolution: 33 × 64 × 16, (y,z,x).

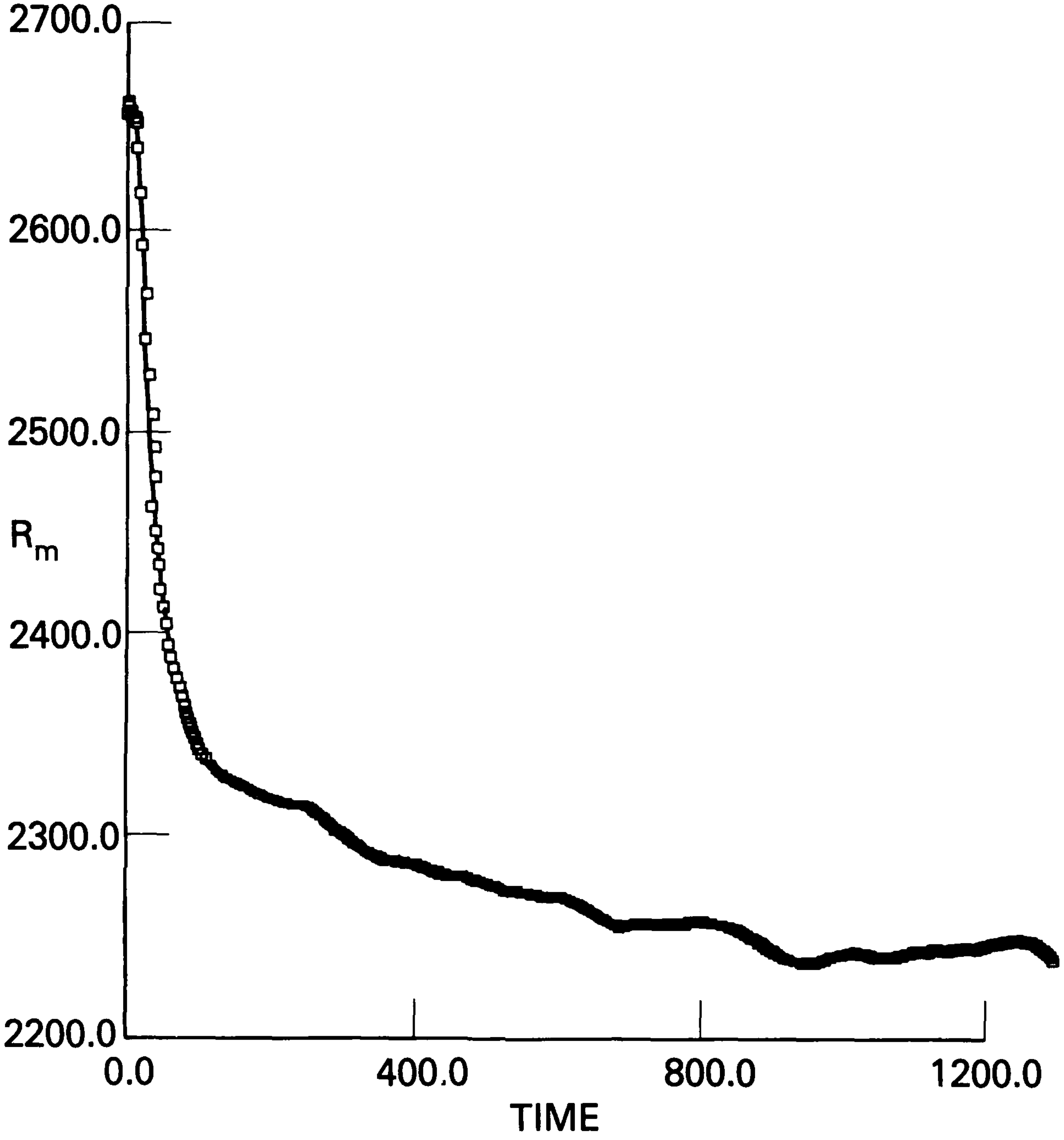

Fig. A1(b) — Reynolds number based on mean velocity versus time.

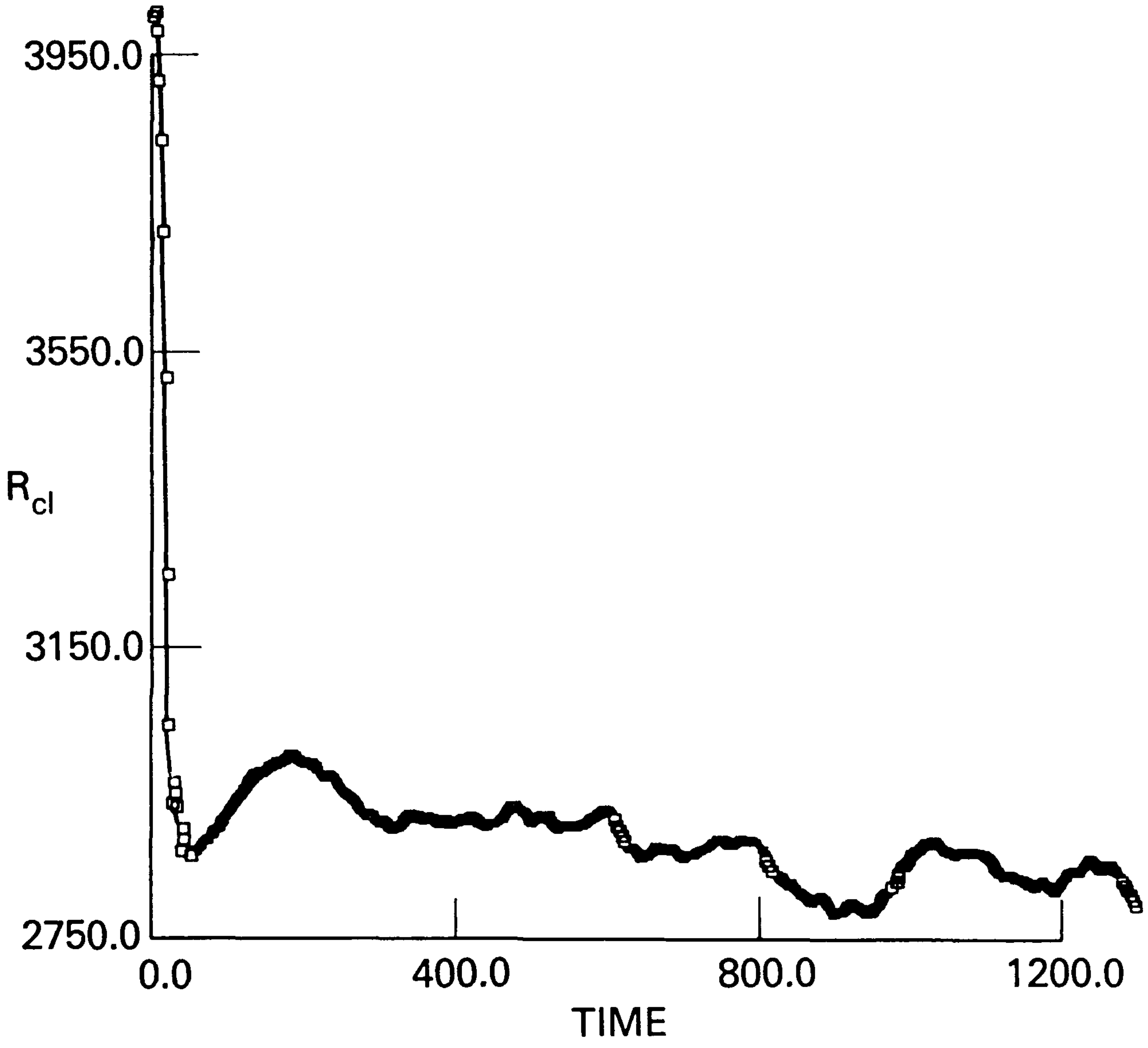

Fig. A1(c) — Reynolds number based on the centerline velocity versus time.

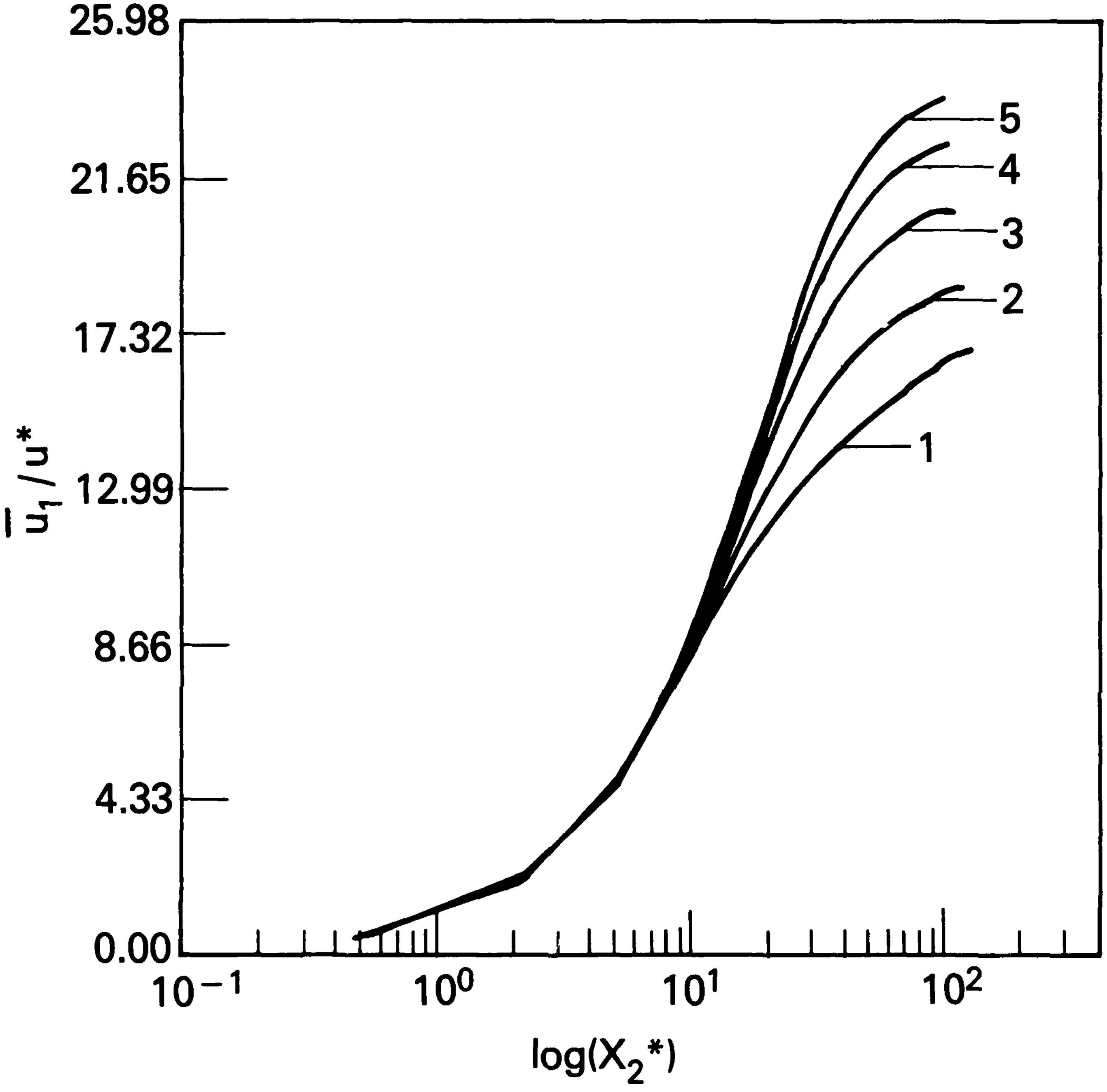

Fig. A2(a) — Mean velocity profile versus time. Time is in viscous units. 1: t = 0, 2: t = 50, 3: t = 100, 4: t = 150, 5: t = 200.

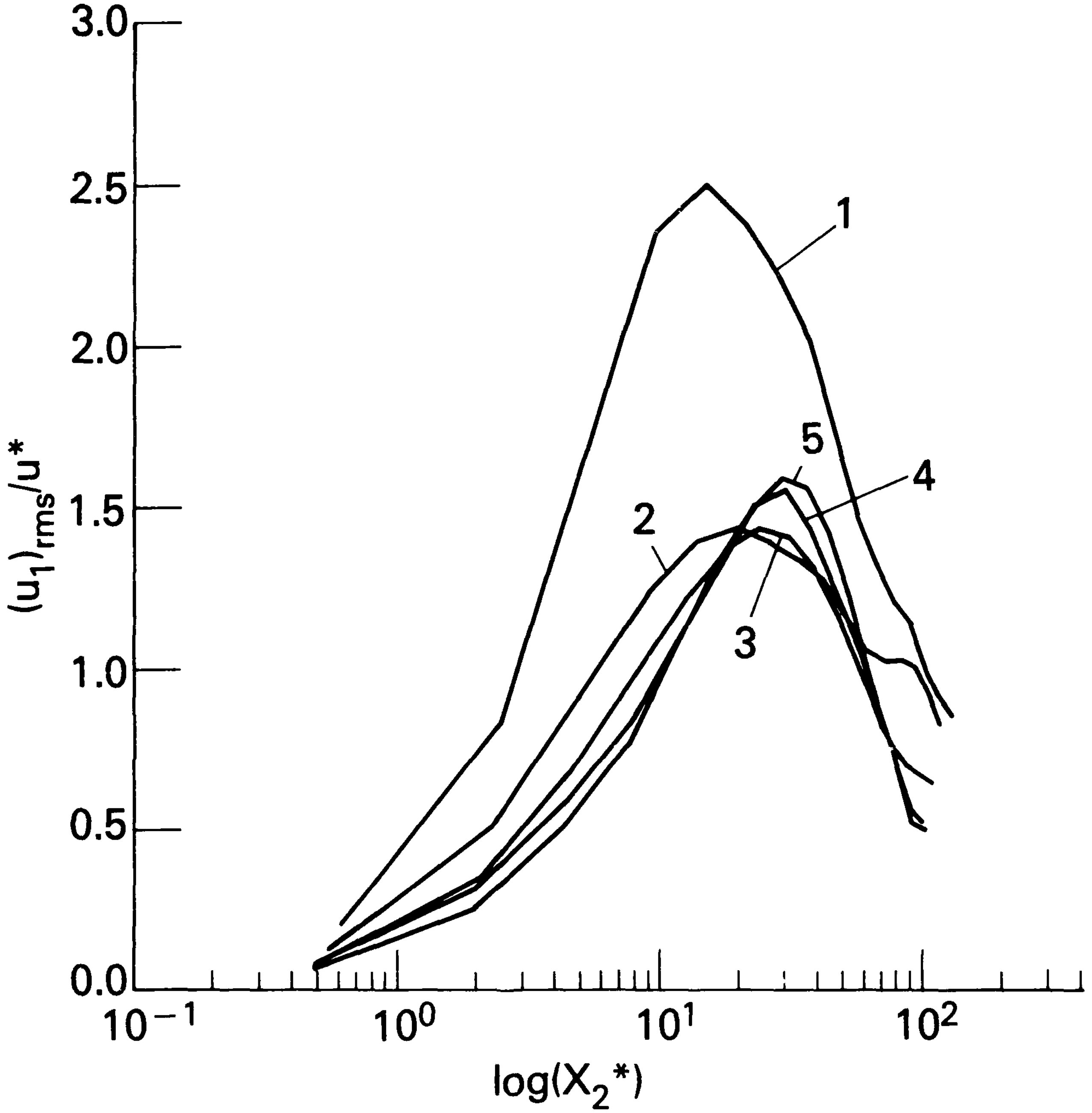

Fig. A2(b) — Streamwise velocity fluctuation intensity profiles. 1: $t = 0$, 2: $t = 50$, 3: $t = 100$, 4: $t = 150$, 5: $t = 200$.

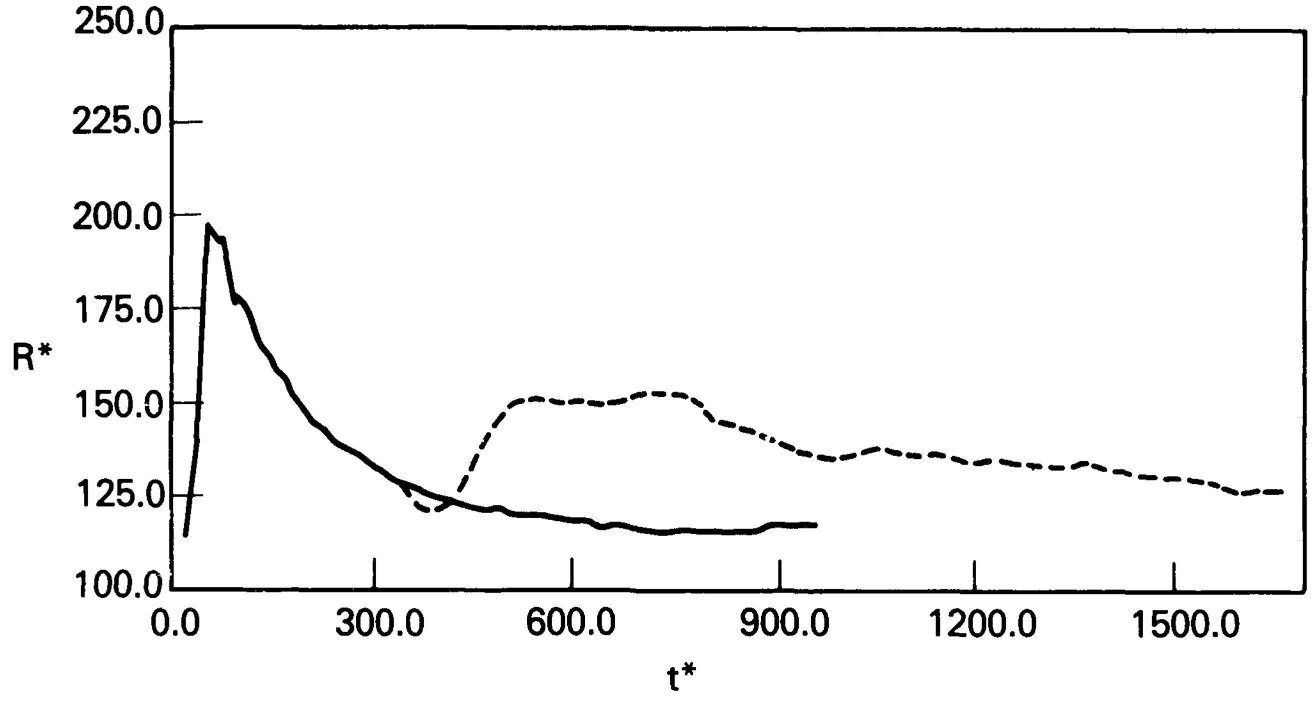

Fig. A3(a) — Reynolds number behavior in channel flow turbulence with and without aliasing. (From Panda (1987)). Wall Reynolds number versus time (viscous units). 33 × 64 × 16 grid: — without dealiasing, ----, with dealiasing.

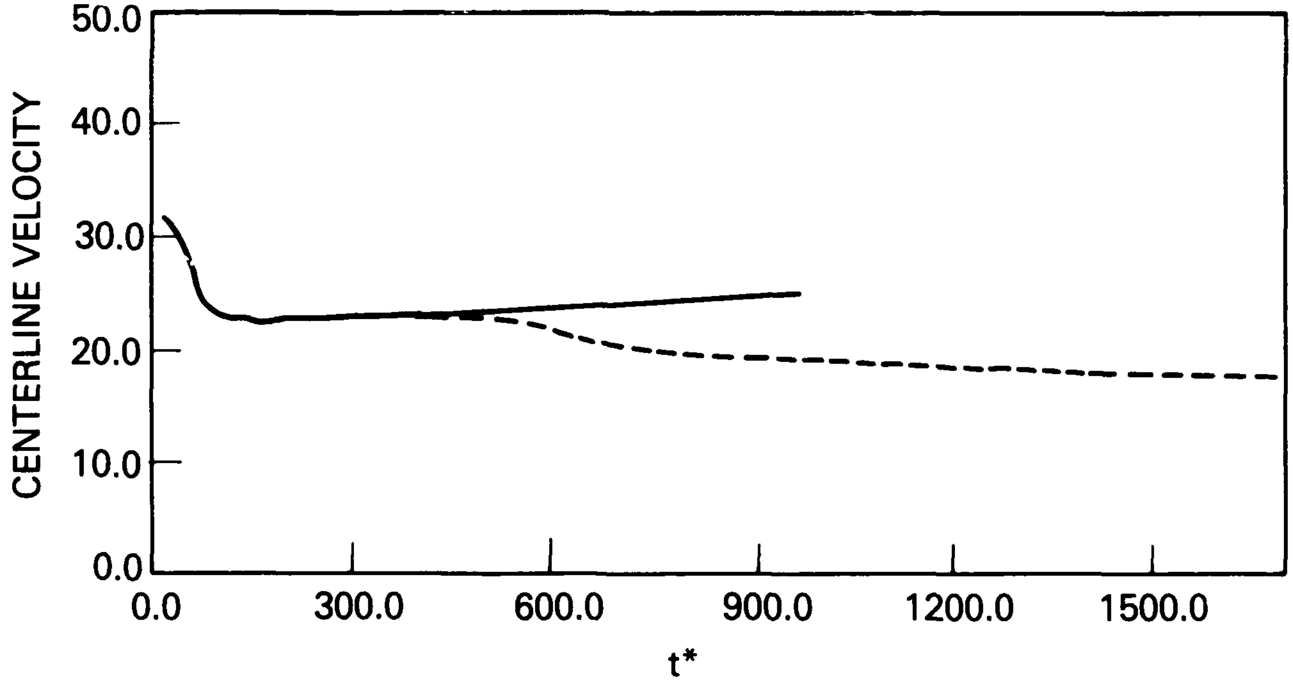

Fig. A3(b) — Reynolds number behavior in channel flow turbulence with and without aliasing. (From Panda (1987)). Centerline velocity versus time.

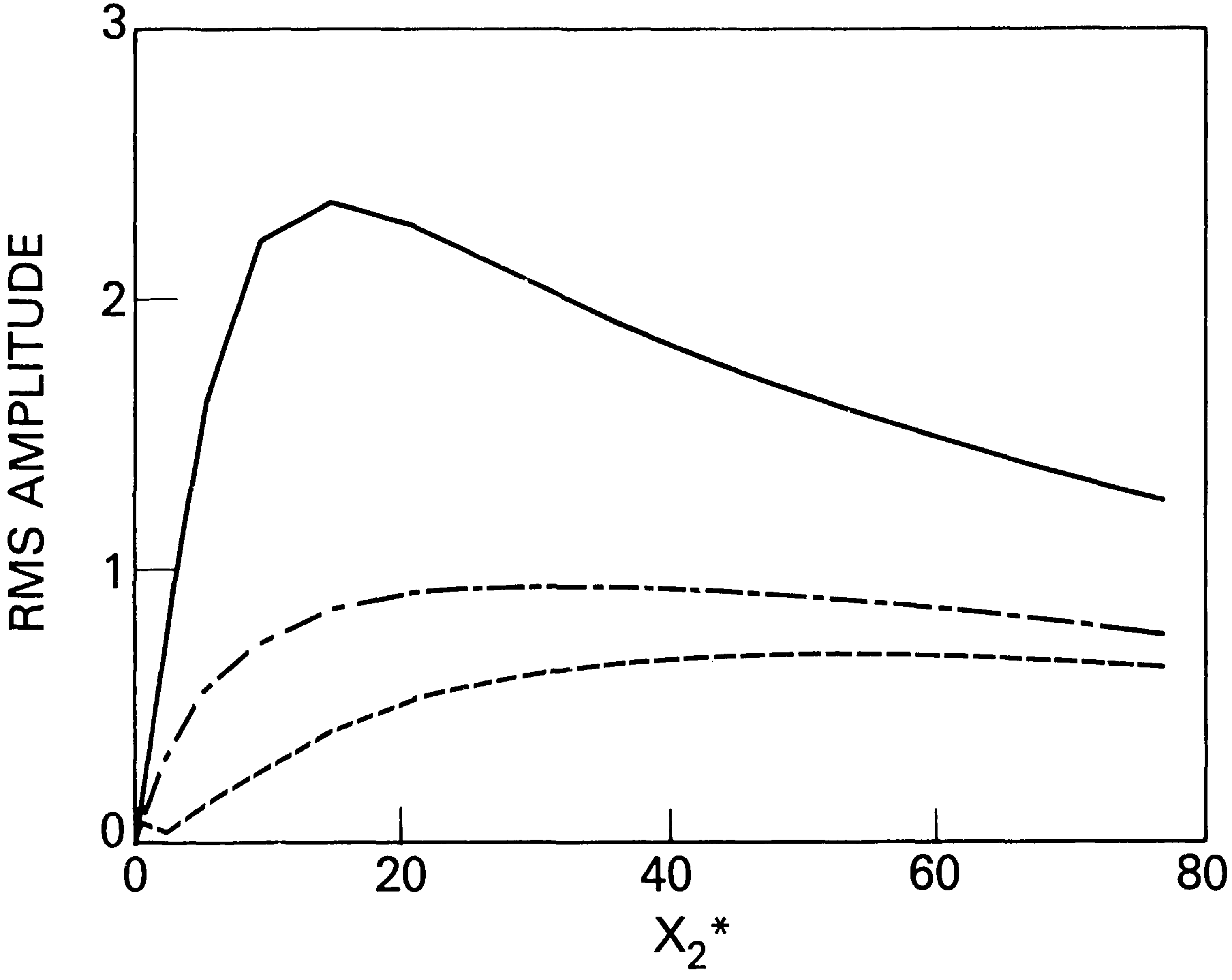

Fig. B1 — Root mean square velocity fluctuation profiles computed from Equation B11. — u_1, — - —, u_3, ----, u_2.

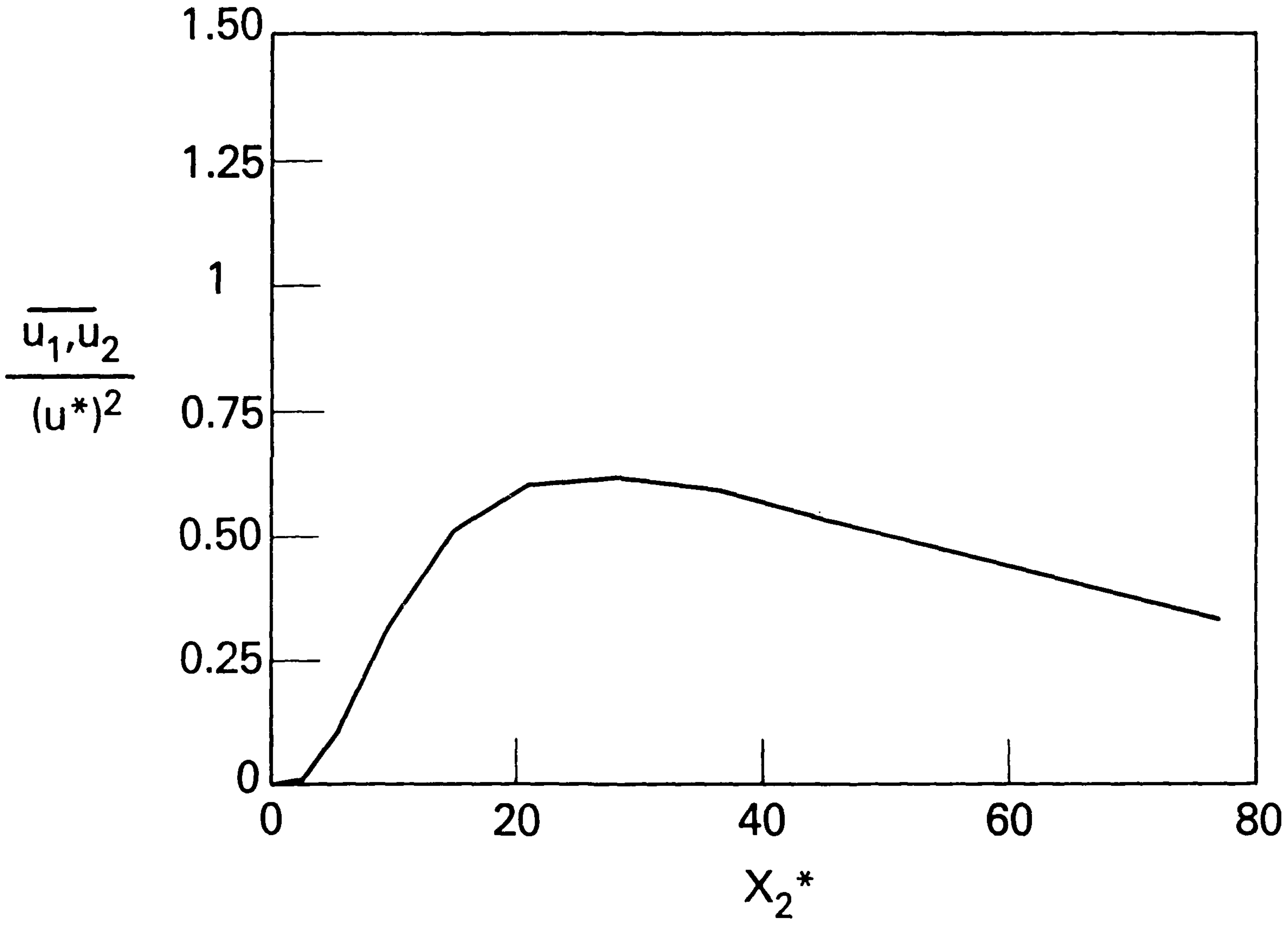

Fig. B2 — $\overline{u_1 u_2}$ computed from equation B11.